UNIVERSIDAD NACIONAL AUTÓNOMA DE MÉXICO

POSGRADO EN CIENCIA E INGENIERÍA DE MATERIALES

INSTITUTO DE FÍSICA

"Third-order nonlinear optical response of ion-implanted embedded arrays of plasmonic gold nanoparticles"

T E S I S

QUE PARA OPTAR POR EL GRADO DE:
DOCTOR EN CIENCIA E INGENIERÍA DE MATERIALES

P R E S E N T A:

M. en C. José Miguel Zárate Reyes

TUTOR PRINCIPAL:

Dr. Juan Carlos Cheang Wong
Instituto de Física

MIEMBROS DEL COMITÉ TUTOR:

Dr. Guillermo Santana Rodríguez
Instituto de Investigaciones en Materiales

Dr. Erick Flores Romero
Instituto de Física

Ciudad Universitaria, Cd. Mx., mayo 2021

A Alejandra

Agradecimientos

Agradezco a la Universidad Nacional Autónoma de México, al Instituto de Física y al Posgrado en Ciencia e Ingeniería de Materiales por el apoyo recibido durante mis estudios de Doctorado, además de agradecer por el apoyo financiero otorgado por el Consejo Nacional de Ciencia y Tecnología (CONACYT) en mis estudios de maestría y doctorado, CVU 632320. A los proyectos PAPIIT-UNAM IN-100819 y IN-112919.

A mi tutor, Dr. Juan Carlos Cheang Wong, gracias por su amistad, su apoyo, su entera confianza, motivación y paciencia.

A los miembros de mi comité tutorial, Dr. Guillermo Santana Rodríguez y Dr. Erick Flores Romero por su acompañamiento durante este trabajo.

Un agradecimiento especial a mis sinodales: Dra. Citlali Sánchez Aké, Dra. Monserrat Bizarro Sordo, Dr. José Manuel Saniger Blesa y al Dr. Jorge Alejandro Reyes Esqueda por la revisión de este trabajo, así como sus comentarios y sugerencias.

Al Ing. Francisco Jaimes Beristain y al Ing. Mauricio Escobar por su valiosa labor en la operación y mantenimiento del Acelerador Pelletron del IFUNAM.

Al Laboratorio Central de Microscopia (LCM): Dr. Jesús Arenas Alatorre, Dr. Arturo Rodríguez, Dr. Samuel Tehuacuanero, M. en C. Manuel Aguilar, Fis. Roberto Hernández, Dr. Carlos Magaña y al Arq. Diego Quiterio por su invaluable asistencia en la toma de micrografías, además de contar con todo su apoyo y amistad a lo largo de todos estos años.

Al M. en C. Juan Gabriel Morales Morales por su asistencia en la preparación de muestras, además de todo su apoyo y amistad a lo largo de todos estos años.

Un especial agradecimiento al Dr. Alejandro Reyes Esqueda por su invaluable participación en este proyecto, así como al Dr. Oswaldo Sánchez Dena y al M. en C. Alberto Peralta Ángeles.

Agradezco enormemente al Dr. Luis Rodríguez Fernández y al Dr. Erick Flores Romero por toda su amistad y apoyo durante toda mi estancia en el Instituto de Física.

A mis amigos y compañeros de laboratorio, M. en C. Carmen Cecilia Salinas Fuentes, Deyanira de la Peña Peña y Santiago Fernández.

A mis amigos de ciencia fácil, Quím. Alejandra Quezada Castro y Fernando Andrés Santiago Díaz, gracias por su amistad y permitirme colaborar en este gran proyecto.

A mis amigos Denisse, Amador, Asael, Aline, Marisol, Adrián, Cesar, Julian, Vladi, Peter, Artwo, George, Richi, Gus, Gonzalo, Amauri, Javitt, Ricardo, Pacheco y a todos aquellos que me faltó mencionar.

A mis padres y hermanos, muchas gracias por todo su apoyo.

Y finalmente, quiero dar gracias a mi compañera de vida, Alejandra. Porque siempre has estado a mi lado y me has apoyado incondicionalmente. Gracias por recorrer este camino conmigo, por acompañarme en los buenos y no tan buenos momentos. ¡Gracias!

Abstract

In this thesis a systematic study was carried out, following a modified Stöber synthesis method, in order to obtain monodisperse submicrometer-sized colloidal silica particles exhibiting a high-quality shape and a narrow size distribution. The novelty of this work consists in setting the initial temperature of the reagents at low temperatures (6 - 14°C) in comparison to the laboratory room temperature, while fixing other experimental parameters such as humidity and reagent concentrations. A series of samples of monodisperse colloidal silica particles were prepared, with diameters ranging from 590 nm to 1000 nm and quite narrow particle size distributions. According to the results it was established that the initial temperature of the reagent solutions constitutes a remarkable parameter, affecting the particle size, shape and monodispersity and even allowing the tunability for the synthesis of large spherical silica particles. Moreover, in combination with spin coating deposition, the proposed technique greatly favors the formation of ordered arrays of monodisperse silica particles over silicon or silica substrates in areas as large as several mm^2. This is ideal for thermal insulators, photonic crystals, Nanosphere Lithography, and other applications requiring high-quality extended arrays of monodisperse silica particles.

On the other hand, for the first time to our knowledge, Nanosphere Lithography in combination with high-energy MeV ion implantation is used to generate ordered arrays of Au nanoparticles deeply embedded in fused silica substrates (about 500 nm below the sample surface). These ordered arrays were prepared by implanting 2 MeV Au^+ ions through a

lithographic silica particle mask. The nonlinear optical response of these periodic arrays was experimentally investigated using the z-scan technique at 532 nm with 26 ps pulses from a Nd:YAG laser. The open-aperture z-scan measurements were performed with different linear polarization angles of the incident light beam. A strong saturable absorption and a very clear nonlinear dichroic behavior were determined, the latter indicated by a sinusoidal modulation of the nonlinear absorption coefficient β (up to about 20 of its absolute value) as a function of the polarization angle, which gives clear evidence of the formation of ordered arrays of embedded Au nanoparticles, corresponding to a honeycomb lattice symmetry with a modulation period of 30°.

The interest in this type of composites consisting of metallic nanoparticles embedded in dielectric media comes from theirs possible advanced applications in nonlinear optical and opto-electronic devices, biosensing, biological imaging and medical field.

Resumen

En esta tesis se presenta un nuevo método para obtener partículas de sílice de tamaños sub-micrométricos, con gran calidad de forma y alta monodispersión. Esta novedosa síntesis basada en el bien conocido método Stöber nos permite incluso la posibilidad de ajustar y sintonizar el tamaño de las partículas.

Lo novedoso de este trabajo consiste en fijar la temperatura inicial de los reactivos a bajas temperaturas (6 - 14°C) mientras se mantienen constantes otros parámetros experimentales tales como la concentración de los reactivos, la humedad relativa y la temperatura ambiente. De este modo se obtuvieron una serie de muestras con diámetros entre 600 nm a 1000 nm con gran monodispersión. De acuerdo a los resultados se establece por vez primera que la temperatura inicial de los reactivos constituye un parámetro de gran importancia, afectando el tamaño, forma y monodispersión de las partículas.

Aunado a lo anterior, en combinación con la técnica de Spin coating, el método propuesto favorece altamente la formación de arreglos bien ordenados de las partículas de sílice, en forma de monocapas, ya sea sobre sustratos de silicio o sobre matrices de sílice de alta pureza, alcanzando áreas tan grandes como algunos mm^2. Esto es ideal para desarrollar aislantes térmicos, cristales fotónicos, Litografía por Nanoesferas y otras aplicaciones donde se requiere que las partículas de sílice sean de alta calidad, monodispersas y que se depositen en forma de arreglos ordenados.

Por otro lado, la técnica de Litografía por Nanoesferas en combinación con la implantación de iones se utilizó por vez primera para generar arreglos plasmónicos de nanopartículas de oro embebidos en matrices de sílice de alta pureza (alrededor de 500 nm por debajo de la superficie). Estos arreglos ordenados fueron producidas a partir de la implantación de iones de Au^+ con una energía de 2 MeV, pasando a través de las máscaras litográficas fabricadas anteriormente a partir de las monocapas ordenadas de partículas de sílice. La respuesta óptica no lineal de tercer orden para estas muestras fue investigada por medio de la técnica z-scan utilizando un láser Nd:YAG con una longitud de onda de 532 nm (cercana a la Resonancia Localizada del Plasmón de Superficie del sistema) con pulsos de 26 ps. Las medidas obtenidas a partir de la configuración "open aperture z-scan" fueron realizadas con diferentes ángulos de polarización de la luz incidente. De este modo, se encontró que las muestras presentan una fuerte saturación de la absorción y un claro efecto dicroico. Este comportamiento se ajusta a una modulación sinusoidal del coeficiente de absorción no lineal β de hasta 20% de su valor promedio como función del ángulo de polarización, lo cual da una clara evidencia de la formación de arreglos ordenados de nanopartículas de Au tipo "Honeycomb" con un periodo de 30°.

El interés en este tipo de materiales que consisten en nanopartículas metálicas embebidas en matrices dieléctricas se deriva de sus posibles aplicaciones en dispositivos ópticos no lineales u opto-electrónicos, biosensores e incluso en el campo de la medicina.

Contents

List of Figures

List of Tables

Introduction

Monodispersed colloidal silica particles have been widely used in many applications including thin films, Photonic Crystals (PCs) [1], Nanosphere Lithography (NSL) [2, 3], Surface-Enhanced Raman Spectroscopy (SERS) substrates [4] and many other fields of materials science and engineering. Nowadays, for the most applications, the industry requires uniformly ordered colloidal silica particles with high quality at relatively low cost. Thus, the synthesis of silica particles by the sol-gel method results to be very suitable for these purposes. Nevertheless, the silica synthesis from Tetraethyl orthosilicate (TEOS) precursor has many drawbacks because it is highly sensitive not only to the reagent concentrations, but also to environmental conditions. The so-called Stöber reactions are facilitated by hydrolysis and condensation of TEOS in absolute ethanol (EtOH) with ammonia (NH_3) as the base catalyst [5]. The spherical shape and a narrow size distribution are important issues in preparing silica particles, particularly for some applications. Thus, looking for a regular morphology and a narrow size distribution, the monodispersity of the synthesized silica particles is considered as the high-quality factor.

On the other hand, composites consisting of metallic nanoparticles (NPs) embedded in dielectric media have attracted considerable interest due to their nonlinear optical properties for advanced applications in nonlinear optical and opto-electronic devices, biosensing, and medical field. [6–11]. Particularly, metallic NPs embedded in fused silica plates are of great interest because of the nonlinear response enhancement due to presence of plasmonics effects associated with the localized surface plasmon resonance (LSPR). The LSPR are collective electromagnetic modes and are strongly dependent on the geometrical structure of the composite medium. Thus, embedded metal NPs in transparent dielectric and semiconductor materials can be effectively used in new integrated opto-electronic devices [12].

In recent years, these type of structures have been prepared using different techniques such as magnetron sputtering, laser ablation, ion implantation, NSL, among others [13–16]. Ion implantation has been applied to the synthesis of embedded nanoparticles in dielectric substrates. By this method, quite high elemental concentrations, beyond solubility restrictions, can be achieved in a solid matrix [12, 17, 18]. The NP concentration can be controlled by a proper combination of ion fluences and post implantation annealing treatments [19]. In principle, the metallic NPs synthesized by this method are randomly dispersed in the dielectric matrices and can be considered as quasi-spherical with a narrow size distribution. On the other hand, NSL is a low-cost technique that allows the fabrication of 2D ordered arrays of metallic nanostructures on top of a substrate surface. Monodisperse spherical particles of polystyrene or silica are the most used materials to develop, by self-assembly, hexagonally ordered close-packed monolayers of micrometer-sized spheres, which in turn will be used as a lithographic mask for NSL [2, 3]. Metallic nanoestructures can provide a platform to increase nonlinear optical effects due to light-matter interaction under intense field conditions. Recently, periodically arranged NP patterns have gained importance in relation to possible tunable nonlinear optical devices, where the tunability arises from a proper control of the shape, size and orientational order of the patterns [20]. In particular, it has been demonstrated that the NP periodicity plays a key role in the capability to modify the nonlinear optical response of the ordered nanostructures in a reversible way by switching of external parameters [14].

In this thesis, based on the Stöber method, was developed a new technique for improvement the quality of silica microparticles by controlling the initial temperatures of reagents in sol-gel synthesis, referred to hereafter as “LIT-synthesis” (Low initial temperature-synthesis). Furthermore, it is well known that the physical treatments on the sol or gel can have a substantial impact on the final gel structure [21]. Therefore, taking into consideration how the rate of evaporation during gelation can affect the quality of the silica particle monolayer,

a new approach during the spin coating deposition was developed to improve successfully the quality of the silica particle monolayers. Thus, with these results, NSL in combination with direct ion implantation has been used to generate ordered arrays of Au nanoparticles embedded in fused silica substrates. The Z-scan technique with variable linear polarization angle is used to probe the third-order nonlinear optical properties. The effects of dichroism regarding the nonlinear optical response of the plasmonic Au NPs in such honeycomb lattice symmetry are studied in detail.

1.1. Hypothesis

The synthesis of high-quality silica particles will improve monolayers quality of silica particles on silicon and silica substrates, by means of Spin-coating method. These monolayers on silica substrates will serve as lithographic masks when high-energy gold ions impinge on them. That is, only ions that pass through the interstitial spaces of the silica particles will be deeply implanted into the substrate. From a thermal treatment, the nucleation of gold nanoparticles will be promoted, originating nanoparticles located in the intersticial positions determined by the hexagonally ordered silica mask. The gold nanoparticles, being in a dielectric medium, shall present third-order non-linear optical properties such as Saturable Absorption (SA). Likewise, this last property must depend directly on the polarization of the incident light confirming the formation of ordered nanostructures inside the substrate.

1.2. Aim

The aim of this investigation is to study the third-order nonlinear optical response of embedded arrays of plasmonic gold nanoparticles fabricated by Ion-Implanted and Nanosphere Lithography for their great potential in advanced applications for nonlinear optical and opto-electronic devices, biosensing, and even medical field.

1.3. Objectives

The following objectives have been set to fulfill this aim:

1. Optimize the synthesis of colloidal silica particles by varying physical parameters, such as temperature, humidity, and dripping time from the Sol-gel method (Stöber method).

2. Establish ideal parameters in the Spin-coating technique for the generation of high-quality monolayers of silicon colloidal particles over silicon and silica substrates for later use as lithographic masks.

3. Implant high-energy gold ions of the order of Megaelectron Volts (MeVs) through the interstitial regions of the lithographic mask over silica substrates to generate an ordered array of gold nanoparticles inside the substrate.

4. Confirm the formation of embedded ordered arrays of nanoparticles by studying the third-order nonlinear optical response as a function of light polarization using the Z-scan technique in its open-aperture configuration.

CHAPTER ONE

Sol-Gel Method

Sol-gel process is a highly versatile method that allows obtaining a large variety of materials of different composition such as oxides, mixed oxides, and hybrid organic-inorganic materials. Used since the second half of the 19th century, it seems to stand as an alternative method in those fields where it is necessary to have a lot of homogeneity and purity for the manufacture of colloidal particles, because with this technique it is possible to develop new materials that are hardly accessible by other routes.

A colloid is a suspension in which the dispersed phase is so small ($1 - 1000$ nm) that gravitational forces are negligible and interactions are dominated by short-range forces, such as van der Waals attraction and surface charges. Thus, a sol represents a particular case of colloidal system given by the combination of a liquid as dispersive medium and a solid as the dispersed phase, whit a dimension smaller than 1 μm) [21, 22].

The IUPAC (International Union of Pure and Applied Chemistry) defines the sol-gel process as: "Process through which a network is formed from solution by a progressive change of liquid precursor(s) into a sol, to a gel, and in most cases finally to a dry network" [23]. Thereby, the process involves the transformation from a colloidal to a gel system, and at the end of the process, when a gel is finally obtained, the removal of the liquid through drying gives a solid material. In this way, a gel is a colloid in which the liquid medium has become viscous enough to behave more or less as a solid [22], while the IUPAC defines a gel

as: “Non-fluid colloidal network or polymer network that is expanded throughout its whole volume by a fluid”. [23]

The chemistry of the process largely depends on the choice of precursors. Inorganic salts, metal alkoxides, and organosilanes are some of the most common components used for sol-gel processing. The most popular family of precursors for sol-gel silica processing is composed by silicon alkoxides (alkoxysilanes). They are characterized by the strong covalent $Si-O$ bonding and are hydrophobic and immiscible with water. Among the most used are tetraethyl orthosilicate (TEOS), $Si(OC_2H_5)_4$ and tetramethyl orthosilicate (TMOS) $Si(OCH_3)_4$, which is less safe to handle and hydrolyzes faster than TEOS (around six times faster) [24]. In this work TEOS was used as precursor.

The first stage of the sol-gel process is the formation of a sol from a precursor; the second is the development of a gel through the sol to gel transition (Fig. 1.1). This transformation is due to the reactions of hydrolysis and condensation of metal alkoxides in the presence of mineral acid (*e.g.*, HCL) or base (*e.g.*, NH_3) as catalyst [25].

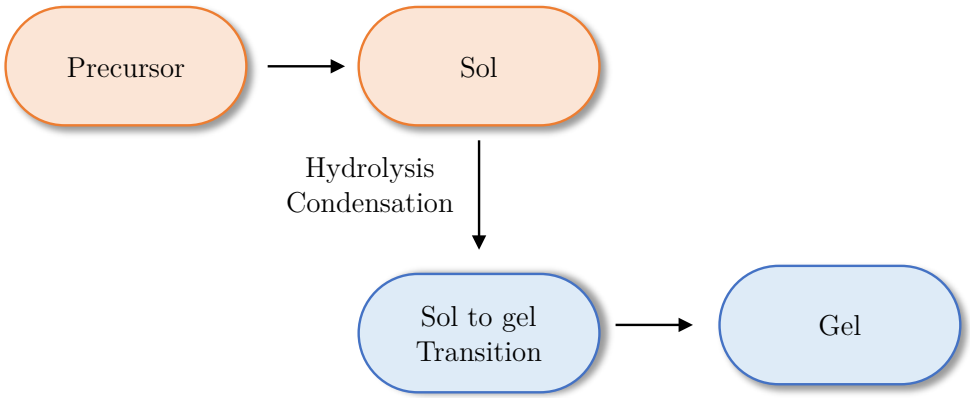

Figure 1.1: Scheme of the stages involved in a sol to gel process [22].

The figure 1.2 shows some products that can be formed using the sol-gel method. There is an intriguing discussion about this figure in the reference [22]. Here, Plinio explains

why it is difficult to model and to represent the sol-gel transition in inorganic systems through drawings because it is easy to misunderstand the complexity of the process using an oversimplified scheme.

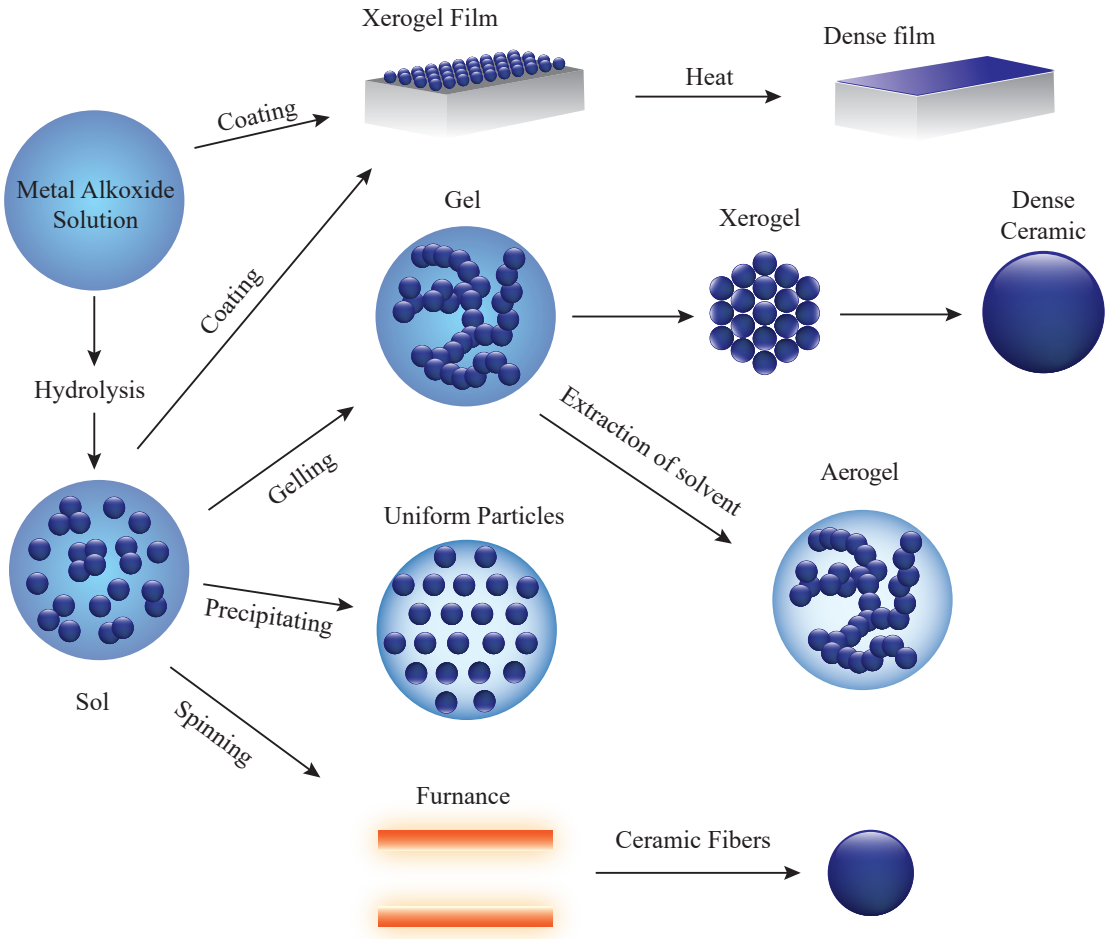

Figure 1.2: Different products of sol-gel process [22].

The sol-gel process is widely applied to produce silica particles and one of the most cited is the Stöber method, and the main advantage of this method is the ability to form monodispersed spherical silica particles compared to the acid-catalyzed system.

1.1. Synthesis of silica particles by Stöber method

A pioneer work on the synthesis of spherical and monodispersed silica particles was developed by Stöber, Fink and Bohn [5] in 1968, hereby known as Stöber Method, where silica particles with sizes in the range of 5 nm to 2 μm were obtained. This process involves the hydrolysis and condensation polymerization of TEOS, and this reaction is performed in the presence of the basic catalyst, ammonia. The overall hydrolysis and condensation reactions, respectively, can be written as [21, 26]:

$$Si(OC_2H_5)_4 + 4H_2O \longrightarrow Si(OH)_4 + 4C_2H_5OH \tag{1.1}$$

and

$$Si(OH)_4 \longrightarrow Si(O)_2 + 2H_2O \tag{1.2}$$

Experimentally, The Stöber method is carried out by mixing pure alcohol (ethanol or methanol), ammonium hydroxide and water, subsequently TEOS is added to the solution and the condensation reaction generally started within 10 min. This is observed due to an increasing opalescence of the mixture.

1.2. Mechanism for silica particle growth

All of the colloidal particle formation models agree that the reaction begins with the formation of particle nuclei and continues with the increase in particle size with time. There are two main proposed mechanisms for silica particle growth (Fig. 1.3). One is the monomer addition growth model which is based upon LaMer's original model [27] and the second is based on aggregation mechanism. In the monomer addition model of particle growth (Fig. 1.3.a), generally, nucleation is described as homogeneous, that is, once supersaturation

is reached the precipitable material falls out of solution in a quick outburst. Then, the particle growth occurs via the polycondensation of monomers on the surface of the newly formed nuclei or existing particles. In the second model (Fig. 1.3.b), nucleation and growth of particles are proposed to occur via an aggregation mechanism through the flocculation of nanometer-sized particles which are referred to as subparticles or primary particles [26]. In cases where the product is influenced by parameters such as ionic strength, pH, and solvent properties including the dielectric constant and viscosity, then aggregation is likely the dominant growth mechanism. However, independently of the growth mechanism, the nucleation process only occurs at the early stages of the reaction, leading to an increase in the final size of the particles and a narrow size distribution [26].

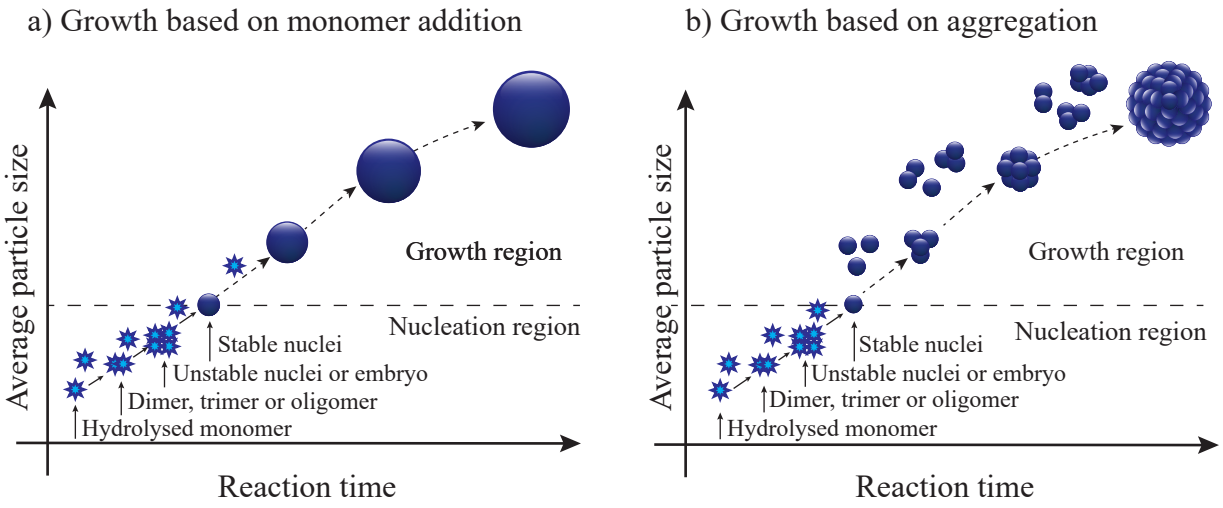

Figure 1.3: A general representation of particle growth base on a) monomer addition and b) aggregation mechanisms [26].

CHAPTER TWO

Optical Properties

The optical properties of metal nanoparticles (NPs) have been exploited from immemorial times in sculptures and paintings. The most famous example is the Lycurgus Cup (4th centuy AD) that is exposed in the British Museum of London (Fig. 2.4). The cup changes its color from red to greenish when illuminated by white light from different sides. For long time, the nature of these colors was unclear, but now it is known that the mentioned effects of light occur because the cup is made of a dichroic glass containing gold-silver NPs that provides the red color of transmitting light and green color of scattering light [6, 28].

Figure 2.4: The Roman Lycurgus Cup.

2.1. Basic electromagnetic theory

The light is a form of electromagnetic wave that consists of oscillating electric and magnetic fields. Figure 2.5 shows the wavelength and frequency range of visible and invisible light along with other types of electromagnetic waves. The wavelength of visible light ranges from about 400 nm to 650 nm, which defines several critical dimensions in optical techniques. The electric and magnetic fields of propagating light are perpendicular to each other and to the direction of propagation. If an electromagnetic wave hits an interface to another medium, boundary conditions have to be fulfilled for the parallel and normal components. The surface defines a plane of incidence that contains the surface normal and the incoming beam, also, the electric and magnetic fields can be decomposed into separate polarization components parallel and perpendicular to the plane of incidence, in this way, p- and s- polarization or transverse - magnetic (TM) and transverse - electric (TE) polarization [29].

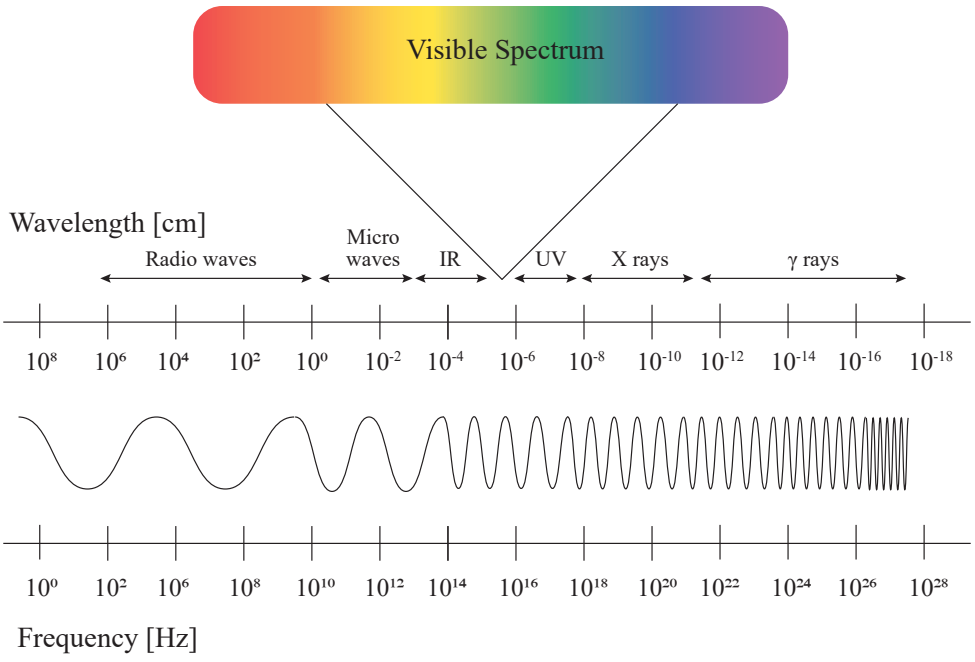

Figure 2.5: Light as an electromagnetic wave.

The interaction between metals and light can be reliably described in terms of classical Maxwell's equations. These equations also completely applicable for nanoparticles and nanostructures, since at room temperature the spacing between electron levels stays tight as compared with thermal excitation energy due to high electron density [28].

It is well known that metals reflect light effectively and thus do not allow light propagation inside it. In microwave and infrared bands, metals are used frequently for fabrication of waveguides. At these frequencies, Joule losses inside metals are small and an approximation as a perfect conductor is extremely effective. As the frequency increases, the absorption increases and in the optical region the approximation is not quite adequate. In the ultraviolet region, some metals such as sodium (Na) turn out to be transparent, while others such as gold and silver are heavily absorbing in this region due to interband transitions.

This complex behavior of metals can be described with the help of the function dielectric $\epsilon(\omega)$, which is a fundamental parameter in the study of optical properties. The physical reason for the strong dependence of the function dielectric on frequency is a change in phase of the currents induced in metal relative to the incident light phase in the frequency region close to the so-called plasma frequency, which will be defined further [28].

The optical properties of solids provide an important tool for studying energy band structure, impurity levels, excitons, localized defects, lattice vibrations, and certain magnetic excitations. Experimentally, we measure some observable, such as reflectivity, transmission, absorption, etc., and from these measurements we deduce the dielectric function $\epsilon(\omega)$, the optical conductivity $\sigma(\omega)$, or the fundamental excitation frequencies. It is the frequency-dependent complex dielectric function $\epsilon(\omega)$ or the complex conductivity $\sigma(\omega)$, which is directly related to the electronic energy band structure of solids.

2.2. The complex dielectric function and complex optical conductivity

Assuming no charge density in the absence of incident light, the complex dielectric function and complex optical conductivity are introduced through Maxwell's equations [30]:

$$\begin{aligned} \nabla \times \mathbf{E} &= -\frac{\partial \mathbf{B}}{\partial t} \\ \nabla \times \mathbf{H} &= \frac{\partial \mathbf{D}}{\partial t} + \mathbf{j} \\ \nabla \cdot \mathbf{D} &= 0 \\ \nabla \cdot \mathbf{B} &= 0 \end{aligned} \tag{2.3}$$

Here, $\mathbf{H}$, $\mathbf{E}$ and $\mathbf{j}$ are the magnetic field strength, electric field and current density, respectively, while $\mathbf{D}$ and $\mathbf{B}$ are the electric displacement and magnetic field in a medium. The constitutive equations relating $\mathbf{D}$, $\mathbf{B}$ and $\mathbf{j}$ to $\mathbf{E}$ and $\mathbf{H}$ field are written as [30]:

$$\begin{aligned} \mathbf{D} &= \epsilon \mathbf{E} \\ \mathbf{B} &= \mu \mathbf{E} \\ \mathbf{j} &= \sigma \mathbf{E} \end{aligned} \tag{2.4}$$

From Maxwell's equations and the constitutive equations one can obtain a wave equation for the variables $\mathbf{E}$ and $\mathbf{H}$ for electric and magnetic fields, respectively:

$$\nabla^2 \mathbf{E} = \epsilon\mu \frac{\partial^2 \mathbf{E}}{\partial t^2} + \sigma\mu \frac{\partial \mathbf{E}}{\partial t} \tag{2.5}$$

and

$$\nabla^2 \mathbf{H} = \epsilon\mu \frac{\partial^2 \mathbf{H}}{\partial t^2} + \sigma\mu \frac{\partial \mathbf{H}}{\partial t}. \tag{2.6}$$

For optical fields a sinusoidal solution to (2.5) and (2.6) can be found, and is given by:

$$\mathbf{E} = \mathbf{E}_0 e^{i(\mathbf{K}\cdot\mathbf{r}-\omega t)} \tag{2.7}$$

here $\mathbf{K}$ is a complex propagation constant, ω is the frequency of the light, and i is the imaginary unit. The real part of $\mathbf{K}$ can be identified as a wave vector, while the imaginary part of $\mathbf{K}$ accounts for the attenuation of the wave inside the solid material and corresponds to energy dissipation [30]. Replacing the plane wave solution (2.7) into the wave equation (2.5) the following relation results for K [30]:

$$K^2 = \epsilon\mu\omega^2 + i\sigma\mu\omega \tag{2.8}$$

If there were no losses in energy propagation, K would be equal to $K_0 = \omega\sqrt{\epsilon\mu}$ and would be a real number which has units of reciprocal length and k is thus identified as a wave vector. However, since there are losses in a conducting medium, then:

$$K = \omega\sqrt{\epsilon_{\text{complex}}\mu} \tag{2.9}$$

where we have defined the complex dielectric function as:

$$\epsilon_{\text{complex}} = \epsilon + \frac{i\sigma}{\omega} = \epsilon' + i\epsilon'' \tag{2.10}$$

Complex dielectric function of a nonmagnetic medium can be determined, for example, through examination of properties of the light reflected by the surface of a metal or other substance and through measurement of the complex refractive index $\tilde{n}$ [28, 30]:

$$\tilde{n} = \sqrt{\epsilon_{complex}} = n + ik \tag{2.11}$$

where n is a usual refractive index and k is the extinction coefficient that determines the optical absorption and has units of time/length.

From equation 2.11, the following relationships can easily be obtained:

$$\begin{aligned} \epsilon' &= \epsilon_0(n^2 - k^2) \\ \epsilon'' &= \epsilon_0(2nk) \end{aligned} \tag{2.12}$$

and vice versa:

$$\begin{aligned} n^2 &= \frac{\epsilon'}{2\epsilon_0} + \frac{1}{2}\sqrt{\epsilon'^2 + \epsilon''^2} \\ k &= \frac{\epsilon'^2}{2n\epsilon_0}. \end{aligned} \tag{2.13}$$

The extinction coefficient k is related to the absorption coefficient in the Lambert-Beer law describing exponential decrease of light intensity in a medium by:

$$I(x) = I_0 e^{-\alpha x} \tag{2.14}$$

where I_0 is the light intensity at a distance x into the medium, α is the linear absorption coefficient, which depends of the frequency by the following relation:

$$\alpha(\omega) = 2k(\omega)\omega \tag{2.15}$$

Thus, the imaginary part of the dielectric function defines the absorption in a substance.

2.3. The plasma frequency

The plasma medium is defined as a system with equal concentration of positive and negative charges in which some of the carriers are free to move under the action of electromagnetic fields. Metals or degenerate semiconductors are very good examples of a plasma medium because both have free carriers. Thus, at very low frequencies, i.e., $\omega\tau << 1$, where τ is the relaxation time of the free carriers in the presence of an optical electric field, the optical properties of semiconductors exhibit a metal-like behavior, while at very high frequencies, $\omega\tau >> 1$, their optical properties are like those of insulators. The characteristic frequency at which the material changes form metallic behavior to a dielectric response is called the plasma frequency ω_p, which is defined as that frequency at which the real part of the dielectric function vanishes $\epsilon'(\omega_p) = 0$ and can be described by [28, 30–33]:

$$\omega_p = \sqrt{\frac{ne^2}{\epsilon_0 m}} \tag{2.16}$$

where n is the electron density, ϵ_0 is the dielectric constant of the vacuum, e is the elementary charge and m is the effective mass of an electron. Thus, the bulk plasmon frequency of a particular metal depends only on its free electron density.

The quanta of these charge oscillations are plasmons, that is, quasi particles with energy [32]:

$$E_p = \hbar\omega_p = \hbar\sqrt{\frac{4\pi ne^2}{m}} \tag{2.17}$$

where $\hbar$ is the reduced Planck constant. The energy E_p is the minimum energy necessary for exciting a plasmon.

The plasma frequency defines the boundary region below which the transverse electromagnetic wave propagates in a given medium containing free carriers that attenuate the wave

propagation, and a wave at higher frequency (above ω_p) that propagates without attenuation because the phase change of the wave is too fast for free carriers to respond. In summary, if $\omega > \omega_p$ the wave propagates and if $\omega < \omega_p$ the waves are attenuated [30].

The plasma frequency for most metals occur in the ultraviolet (UV) region, with alkali metals and some transition metals such as Ag and Au exhibiting plasma frequencies in the visible region. Due to the penetration depth of an electromagnetic wave on a metal surface is limited (< 50 nm for Ag and Au), only plasmons caused by surface electrons are significant and are commonly referred to as Surface Plasmons (SPs).

2.4. Localized Surface Plasmon Resonance (LSPR)

SPs consist of a collective oscillation of conduction electrons at the interface between a metal and dielectric medium. SPs can be excited at the surface of bulk metals, but they are particularly important in the case of nanostructures. The large surface to volume ratio of nanostructures allows that SPs determine their optical properties, providing new phenomena not achievable in bulk materials.

For metallic films, SPs consist of oscillating waves of free electrons that travel at the interface between a conductor (metal) and an insulator (dielectric). These electromagnetic waves, with p-polarization, are associated with waves that travel perpendicular to the metal - dielectric interface and decay exponentially into both media, as shown figure 2.6 [34]. This guided mode couples to electromagnetic waves resulting in a polariton. Surface plasmon polaritons (SPPs) occur at frequencies close to but smaller than plasma frequency. These surface modes show exceptional properties for applications of nanophotonics, specially they constitute a class of nanophotonics themselves, namely nanoplasmonics [32].

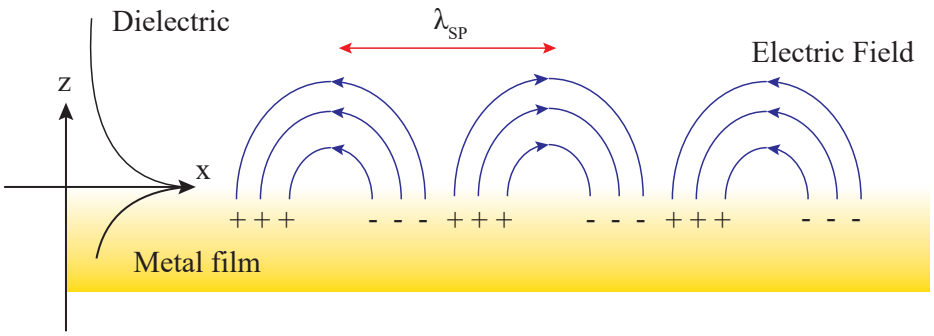

Figure 2.6: SPs at the interface between a dielectric medium and a metal.

If the collective oscillation of free electrons is confined to a finite volume as with a metal nanoparticle, the corresponding plasmon is called a localized surface plasmon (LSP). The theoretical frequency of a localized surface plasmon is $\omega_p/\sqrt{3}$ for a metal sphere placed in vacuum. Figure 2.7 shows the interaction between the electric field of incident light and the free electrons of a metal sphere whose size is smaller than the wavelength of light [33].

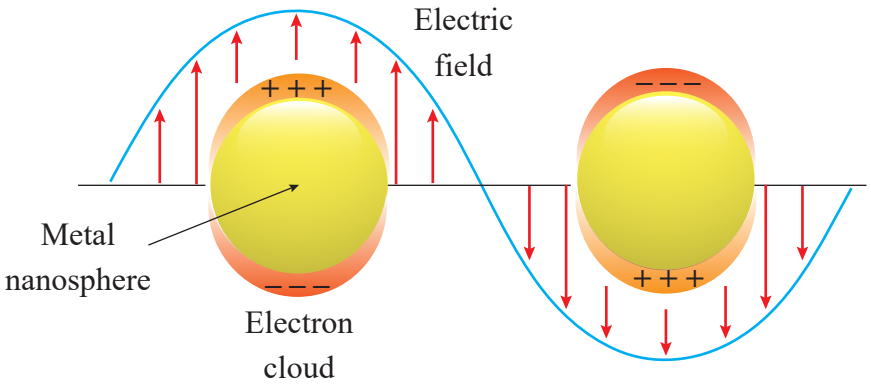

Figure 2.7: Localized surface plasmons (LSPs) of a metal nanosphere [33].

The electric field can cause free electrons to move away from the metal NP in one direction, creating a dipole that can switch direction with the change in electric field. This dipole creates an electric field inside the NP opposite to that of the light, which acts as a restoring force to the equilibrium position. When the frequency of the dipole plasmon

is approximately the same as the incident light, a resonance condition is reached, leading to constructive interference and the strongest signal for the plasmon. Such a condition is known to as surface plasmon resonance, or Localized Surface Plasmon Resonance (LSPR) for the case of a metal NP. for spherical NPs of Au and Ag with diameters less than 30 nm, mainly dipole plasmon resonances are involved; Nevertheless, for larger particles, quadruple plasmon resonance from two negatively charged poles and two positively charged poles can be observed [33].

In NPs, the electrons suffer damping during their movement due to the scattering process with the ionic cores and the NP surface, so the situation is similar to a damped oscillator, reducing the oscillation amplitude. Therefore, metallic NPs show absorption bands in the optical extinction spectra associated with the LSPR [34].

The absorption efficiency of a NP is given by its absorption cross section, σ_{abs}, which corresponds to the geometrical section of an ideal opaque NP absorbing the same number of photons as the studied NP. As figure 2.8 shows, it could replace the absorbing NP by a perfect opaque one (absorbing any photon reaching its surface) that will absorb the same number of photons as the real NP. The section of this ideal particle represents the absorption cross section of the NP. For instance, if we have an NP absorbing half of the photons reaching its surface, σ_{abs} will be half of its geometrical section [35].

In addition to absorption, light interacting with matter can be scattered, changing the propagation direction and eventually also energy and moment. For this process, it can be defined also the scattering cross section, σ_{sca}, as the geometrical section of an ideal scattering NP (that scatters any photon reaching its surface) with the same scattering efficiency as the real particle [35].

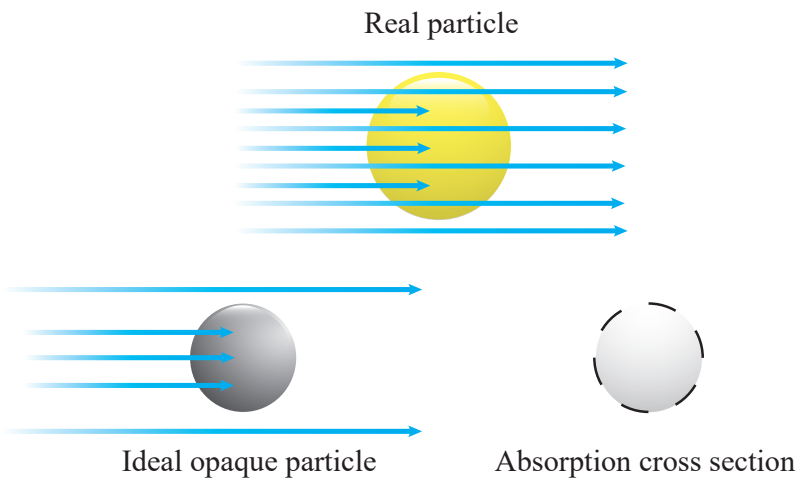

Figure 2.8: Illustration of absorption cross section concept.

The sum of σ_{abs} and σ_{sca} is defined as the extinction cross section:

$$\sigma_{ext} = \sigma_{abs} + \sigma_{sca} \tag{2.18}$$

that represents the efficiency of the NP to remove photons from an incident beam by both absorption and scattering process. Figure 2.9 shows the wavelength of SPR absorption band and the σ_{ext} for metallic NPs with 10 nm size.

The metallic NPs with higher extinction cross section coefficient are the Mg, Na, Ag and Au. However Mg and Na are easily oxidized and hence, the Ag and Au NPs are the most interesting. Nevertheless, Ag is susceptible to sulphuration by atmospheric pollution and can also be oxidized. However, as will be seen later, this work offers an alternative to avoid this issue. Au shows attractive properties such as chemical stability, high biocompatibility and easy functionalization [35]. Consequently, Au is the most frequently used element and the material utilized for this thesis.

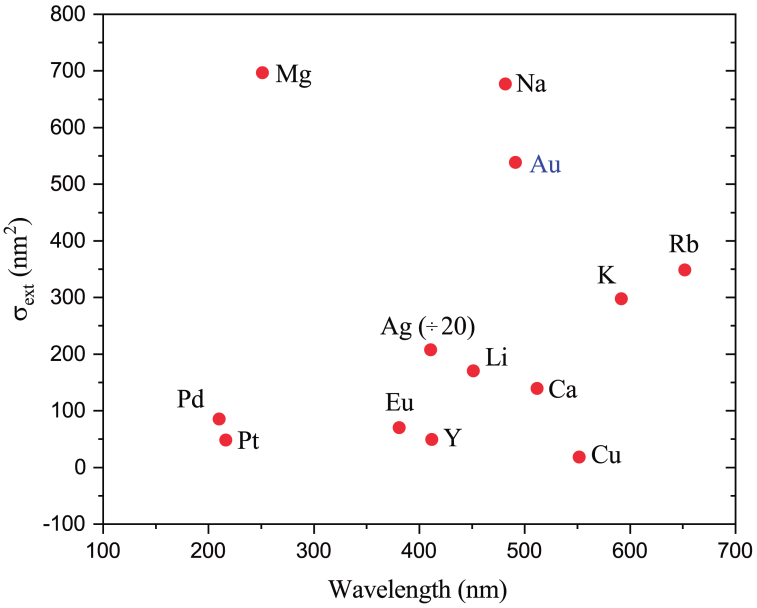

Figure 2.9: Resonant frequency and extinction cross section for some metallic NPs with 10 nm size embedded in air [35].

.

It is important to highlight that a light beam propagating through a medium with metallic NPs decay in intensity as:

$$I(x) = I_0 e^{-N\sigma_{ext}x} = I_0 e^{-N(\sigma_{abs}+\sigma_{sca})x} \tag{2.19}$$

where I_0 is the initial intensity, N the concentration of NPs per unit volume and x the distance traveled in the medium. Therefore, a moderate increase in the extinction cross section, which provides an estimation of the fraction of photons that are absorbed and scattered from the incident beam, can lead to a huge enhancement of light absorption.

From a classical point of view the analysis of the optical response NPs requires solving the Maxwell's equations of electromagnetism with the proper boundary conditions for the surrounding medium [36, 37]. For this purpose, some theories and approximations are commonly employed.

2.5. Mie theory

Gustav Mie found the exact solution to the Maxwell's equations for the optical response of spherical NPs of arbitrary size that are non-interacting, embedded in an homogeneous host and illuminated with a plane monochromatic wave. The Mie theory describes the NP as a spherical object characterized by a dielectric function, ϵ_{NP}, in an infinite dielectric medium with dielectric function ϵ_h.

In a microscopic description we consider that noble metal NPs exhibit large optical response due to the interaction of the electrons with the optical field and the relevant physical processes are: *(i)* intraband transitions and *(ii)* interband transitions.

According to Drude model [36, 37] frequency dependent dielectric function can be described by the following expression [34]:

$$\epsilon_{\text{NP}} = 1 - \frac{\omega_p}{\omega^2 - i\omega\gamma} + \epsilon_{inter} \tag{2.20}$$

where ω_p is the plasma frequency, ϵ_{inter} is an additional feature due to the interband transitions, and γ is the damping constant due to the dispersion of the electrons. The damping constant is given by:

$$\gamma = \gamma_0 + a\frac{v_{\text{F}}}{R} \tag{2.21}$$

where γ_0 represents the damping due to the scattering of the oscillating electrons with the ionic cores, a is a material dependent constant, v_{F} is the Fermi velocity and R is the NP radius. Therefore, including the damping term to the Drude model, the dielectric function can be expressed by [6, 34]:

$$\epsilon_{\text{NP}}(\omega, R) = 1 - \frac{\omega_p}{\omega^2 - i\omega\left(\gamma_0 + a\frac{v_{\text{F}}}{R}\right)} + \epsilon_{inter} \tag{2.22}$$

2.6. Discrete dipolar approximation

The discrete dipolar approximation offers simple equations to calculate light absorption of metallic NPs assuming that they are spherical, isolated and their size is smaller than the wavelength of excitation light (in addition to the hypothesis of the Mie theory). As the LSPR band falls at the visible spectrum ($\sim 360 - 720$ nm), the condition of small NPs is usually achieved for NP diameter below ~ 50 nm. In this case, the electric field inside the NP can be considered as uniform and the particle can be described by an electric dipole, In this case, the solution of Maxwell equations becomes simplified and the extinction cross section coefficient is given by [34, 35]:

$$\sigma_{ext} = \frac{24\pi^2 R^3 \epsilon_h^{3/2}}{\lambda} \frac{\epsilon_2}{(\epsilon_1 + 2\epsilon_h)^2 + \epsilon_2^2} \tag{2.23}$$

where R is the NP radius, λ is the light wavelength, ϵ_h is the dielectric constant of the host and $\epsilon_1 + i\epsilon_2$ is the complex dielectric function of the metallic NPs, which depends on the wavelength. As the size NPs increases, the approximation is no longer valid because the electric field inside the NP cannot be considered uniform.

2.7. Size effects

The NP size affects on the LSPR and consequently on the optical properties, as a general approach, for NPs of less 50 nm of diameter the radiation processes are negligible, and the particle only absorbs energy; on the other hand, for larger NPs the scattering effects dominate the response of NPs [35, 38].

For NPs smaller than ~ 50 nm, the intrinsic effects are related to the damping of the electron oscillations. When SPs are excited, the electrons are damped in their movement by the scattering with the ionic cores and the surface. Experimentally, it is observed that the

relationship between the NP size and the full-width-at-half-maximun (FWHM), Γ, of the LSPR band is given by [34]:

$$\Gamma = a + \frac{b}{R} \tag{2.24}$$

where a and b are material dependent constants and again R is the NPs radius. As the NP size increases, the fraction of electrons in the shell close to the surface represents a smaller fraction of the oscillating electrons and thus, the total effective damping is reduced. Therefore, the FWHM results inversely proportional to the NP radius.

NPs larger than $\sim$ 50 nm cannot be considered much smaller than the wavelength of incident light and the radiation effects are more important. In this case, the displacement of the electronic cloud is not homogeneous, and high multipolar charge distributions are induced [38]. As a consequence, the LSPR band splits into several peaks: two peaks for quadrupole, three peaks for an octopole, etc [35].

2.8. Shape effects

The LSPR is strongly dependent on the NP shape. The most clear example of these shape effects are the nanorods due to that the charge accumulation at the NP surface will be different for electron oscillations along the rod axis and along a perpendicular direction. For this type of nanostructures, the LSPR of transversal plasmons falls at similar position than for spherical NPs (at wavelengths slightly smaller than for spherical NPs) while the resonance of longitudinal plasmons is shifted towards larger wavelengths when the aspect ratio of nanorods increases. When the non-spherical NPs are macoscopically oriented in the same direction, it is possible to distinguish between the different resonances using polarized light. NPs with other geometries, as triangular or cube shapes, show more complicated effects obtaining the plasmon resonance towards larger wavelenth, if its compared with that of the spherical NPs [35].

CHAPTER THREE

Nonlinear Optics

Nonlinear optics is the study of phenomena that occur as a consequence of the modification of the optical properties of a material system by the presence of light. Typically, only laser light is sufficiently intense to modify the optical properties of a material system [39]. When light interacts with metal nanostructures, it can couple to free-electron excitations near the metal surface. As seen in the previous section, LSPR depend on details of the nanostructure, opening up opportunities for controlling light confinement on the nanoscale [11].

Optical nonlinearities are inherently weak, because they are governed by photon-photon interactions enabled by materials. They are linearly dependent on the electromagnetic field and can be strengthened in material environments that provide mechanisms for field enhancement. An increased effective Nonlinear Optical (NLO) response can be achieved through plasmonic effects such as SPPs for extended metal surfaces and LSPR for metal nanoparticles [11].

Plasmonic excitations can be extremely sensitive to dielectric properties of the metal and the surrounding medium as discussed above, this extraordinary sensitivity can be exploited to control light with light, using a control beam to induce a nonlinear change in the dielectric properties of one of the materials, thus modifying the plasmonic resonances and the propagation of a signal beam. In addition, plasmonic excitations can respond on the timescale of a few femtoseconds, allowing ultrafast processing of optical signals [11, 40].

3.1. Classical description

In the classical treatment of the light-matter interaction, the optical field or optical perturbation is described as a plane electromagnetic wave. The coupling between the electromagnetic wave and the medium is characterized by the electric polarization **P** of the medium, which is, to a first approximation, a collection of electric dipoles. When an electric field is applied to a dielectric medium, a separation of bound charges is induced as illustrated in Figure 3.10. This separation of charge results in a collection of induced dipole moments **p**. It is expected that the charged particles oscillate in time coupled to the oscillation of the applied electric field and, thus, behave as microscopic antennas that transmit electromagnetic radiation [41].

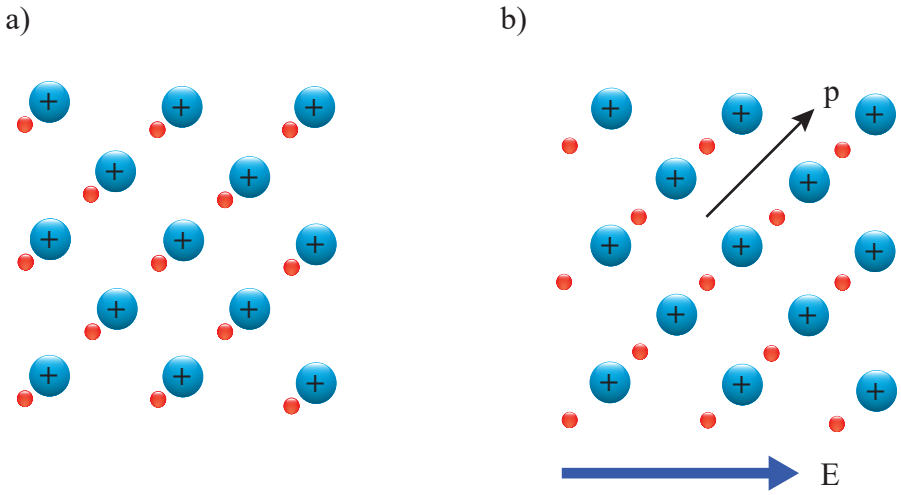

Figure 3.10: Response of a dielectric medium to an applied electric field. (a) Without field applied; (b) field applied.

The electric polarization is defined as the net average dipole moment per unit volume and is given by [42]:

$$\widetilde{\mathbf{P}} = N\langle\widetilde{\mathbf{p}}\rangle \tag{3.25}$$

where N is the number of dipole moments per unit volume, and the angular brackets indicate an ensemble average over all of the dipoles in the medium. In the case of conventional optics (i.e., in the case linear), the induced polarization depends linearly on the electric field in a manner that can be described by the following equation [39]:

$$\widetilde{\mathbf{P}} = \widetilde{\mathbf{P}}_L(t) = \epsilon_0 \chi^{(1)} \widetilde{\mathbf{E}}(t) \tag{3.26}$$

here ϵ_0 is the vacuum electric permittivity and $\chi^{(1)}$ the linear electric susceptibility. The tilde ($\sim$) denotes physical quantities that vary rapidly in time. In nonlinear optics, the NLO response is obtained by generalizing the equation 3.26 by expressing the polarization $\widetilde{\mathbf{P}}(t)$ as a power series in the electric field:

$$\begin{aligned} \widetilde{\mathbf{P}}(t) = \widetilde{\mathbf{P}}_L(t) + \widetilde{\mathbf{P}}_{NL}(t) &= \epsilon_0 [\chi^{(1)} \widetilde{\mathbf{E}}(t) + \chi^{(2)} \widetilde{\mathbf{E}}^2(t) + \chi^{(3)} \widetilde{\mathbf{E}}^3(t) + \cdots] \\ &\equiv \widetilde{\mathbf{P}}_L(t) + \widetilde{\mathbf{P}}^{(2)}(t) + \widetilde{\mathbf{P}}^{(3)}(t) + \cdots \end{aligned} \tag{3.27}$$

The quantities $\chi^{(2)}$ and $\chi^{(3)}$ are known as the second- and third-order nonlinear optical susceptibilities, respectively. They acquire their tensor nature when the vector nature of the electric field is considered [39]. In general, the physical processes that occur as a result of a presence of the second-order polarization, defined as $\widetilde{\mathbf{P}}^{(2)}(t) = \epsilon_0 \chi^{(2)} \widetilde{\mathbf{E}}^2(t)$ are different from those that occur as a result of a presence of the third-order polarization $\widetilde{\mathbf{P}}^{(3)}(t) = \epsilon_0 \chi^{(3)} \widetilde{\mathbf{E}}^3(t)$; in addition, the second-order nonlinear optical response can occur only under the absence of spatial symmetry within a crystal, that is, in noncentrosymmetric crystals. On the other hand, third-order nonlinear response can occur both for centrosymmetric and noncentrosymmetric media [39, 40].

The linear polarization $\chi^{(1)}$ is in principle larger than nonlinear terms. An estimate of orders of magnitude can be obtained for the common case in which the origin of the NLO processes steps out mainly form electron mobility in an atom. When the magnitude of the applied electric field is of the same order of the electric field within an atom [41]:

$$E_{at} = \frac{e}{4\pi\epsilon_0 a_0^2} \tag{3.28}$$

where e is electron charge and a_0 the Bohr radius for the Hydrogen atom. Under non resonance conditions it can be estimated that $\chi^{(2)}$ is of the order of $\chi^{(1)}/E_{at}$, and χ^3 of the order of $\chi^{(1)}/E_{at}^2$. For condensed matter $\chi^{(1)} \approx 1$, and therefore it is expected that $\chi^{(2)}$ will be of the order of $1/E_{at}$, that is:

$$\chi^{(2)} = 1.94 \times 10^{-12} \, \frac{m}{V}$$

Similarly, $\chi^{(3)}$ is of the order of $1/E_{at}^2$, then:

$$\chi^{(3)} = 3.78 \times 10^{-24} \, \frac{m^2}{V^2}$$

The second-order response typically gives rise to wave-mixing effects that lead to frequency conversion, the most common example being second-harmonic generation (SHG), where the incident frequency, ω, is converted to its second harmonic, 2ω; furthermore, sum- and difference-frequency generation, and an electro-optic response. Even more possibilities exist in third order, with third-harmonic generation and four-wave mixing (FWM) as specific examples; however, the third order response contains terms at the incident frequencies. This is known as the optical Kerr effect and results in nonlinear modifications on the refractive index, allowing all-optical switching and modulation of light. By combining Kerr nonlinearities with optical cavities or other systems with feedback, it is possible to obtain bistability, where one input signal allows two possible outputs [11].

Now, in the equations 3.26 and 3.27 it has been assumed that the polarization at time t only depends on the instantaneous magnitude of the electric field, which also implies the treatment of a lossless and dispersionless nonlinear medium. In the case where a dispersive material that might also present loss of energy, the intrinsic vector property of the electric field must be considered. In this way, both electric field and total polarization depend on the position and frequency of the applied optical field. Then, the equation 3.27 can be written as [41]:

$$\widetilde{\mathbf{P}}(\mathbf{r},t) = \sum_{n} \mathbf{P}(\omega_n) e^{-i\omega_n t} \tag{3.29}$$

where a Fourier transform relates the time dependence to the frequency regime. The sum goes on both the positive and negative frequency components of the applied optical field. The components of the second-order susceptibility tensor, $\chi^{(2)}_{ijk}(\omega_n + \omega_m, \omega_n, , \omega_m)$, are defined as the proportional constants that relate the nonlinear polarization amplitude with the product of the amplitudes in the other components of the electric field, that is [39]:

$$P_i(\omega_n + \omega_m) = \sum_{jk} \sum_{nm} \chi^{(2)}_{ijk}(\omega_n + \omega_m, \omega_n, , \omega_m) E_j(\omega_n) E_k(\omega_m) \tag{3.30}$$

here, the indices ijk refer to the cartesian components of the fields. The notation (nm) indicates that in doing the summation over n and m, the sum $\omega_n + \omega_m$ is to be held fixed, regardless of the interchange between ω_n and ω_m. The product $E(\omega_n)E(\omega_m)$ is associated to the time dependence $e^{-i(\omega_n+\omega_m)t}$ as a contribution to the nonlinear polarization oscillating at a frequency $\omega_n + \omega_m$. In the same fashion are defined the components of the third-order susceptibility tensor $\chi^{(3)}_{ijk}(\omega_0 + \omega_n + \omega_m, \omega_0, \omega_n, \omega_m)$ [39]:

$$P_i(\omega_0 + \omega_n + \omega_m) = \sum_{jkl} \sum_{(mno)} \chi^{(3)}_{ijkl}(\omega_0 + \omega_n + \omega_m, \omega_0, \omega_n, , , \omega_m) E_j(\omega_0) E_k(\omega_n) E_l(\omega_m) \tag{3.31}$$

The reason why the polarization plays a significant role in the classical description of the NLO phenomena is that a time-varying polarization can act as the source of new components of the electromagnetic field. This is noticed in the nonhomogeneous wave equation for nonlinear media [39]:

$$\nabla^2\widetilde{\mathbf{E}} - \frac{n^2}{c^2}\frac{\partial^2\widetilde{\mathbf{E}}}{\partial t^2} = \frac{1}{\epsilon_0 c^2}\frac{\partial^2\widetilde{\mathbf{P}}_{NL}}{\partial t^2} \tag{3.32}$$

where n is the refractive index and c is the speed of light in vacuum. This equation expresses the fact that when the term on the right side is different from zero, there are being accelerated charges, and according to Larmor's theorem from electromagnetism, accelerated charges generate electromagnetic radiation.

3.2. Quantum mechanics description

When the light is considered as a stream of photons, it can regarded the interaction between light and matter as a scattering of the photons due to the electrons present in the atoms or molecules in the material. Each photon carries a linear momentum $p = \mathrm{E}/c$ which is partially transferred to the molecule since the electron remains bound to the atoms. This process is considered an elastic scattering for the case of low intensity applied optical fields so that the energy is conserved and thus the frequency of the scattered photons equals that of the incident ones. At the instant of interaction, the photon can be regarded as absorbed and the molecule as being in a virtual excited state, intermediate in energy to the stationary states of the system; however, the duration of such interaction or lifetime of the virtual state τ is small enough not to violate the time-energy uncertainty relation [43]:

$$\tau\Delta\mathrm{E} \leq \frac{\hbar}{2} \tag{3.33}$$

where ΔE is the energy difference between the nearest electronically excited state $|1\rangle$ and the virtual state. The de-excitation of the system from the virtual state back to the ground state $|0\rangle$ is associated with the emission of the scattered photon, a process referred to as linear optics as shown in the Figure 3.11.

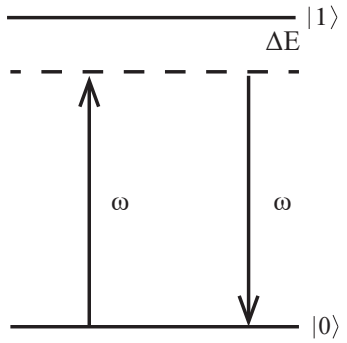

Figure 3.11: Elastic scattering of incident photons of frequency ω [43].

For high-intensity applied fields the incident radiation enhances the probability for simultaneous multi-photon interactions with a single molecule, *i.e.*, two or more photons are annihilated and absorbed by the molecule in a single quantum mechanical process. Generally, in these cases the frequency of the scattered photons is not the same as that of the absorbed photons. For example, two photons with frequency ω may be annihilated, creating a third photon with frequency 2ω as shown in the figure 3.12.a, here the system returns to its ground state $|0\rangle$ after the interactions has taken place, and the intermediate virtual state is separated from first excited state by an energy ΔE. This is an example of a nonlinear optical process known as second-harmonic generation, to the case where three photons with frequency ω are annihilated, creating a fourth photon with frequency 3ω is known as a Third-Harmonic Generation (THG) 3.12.b.

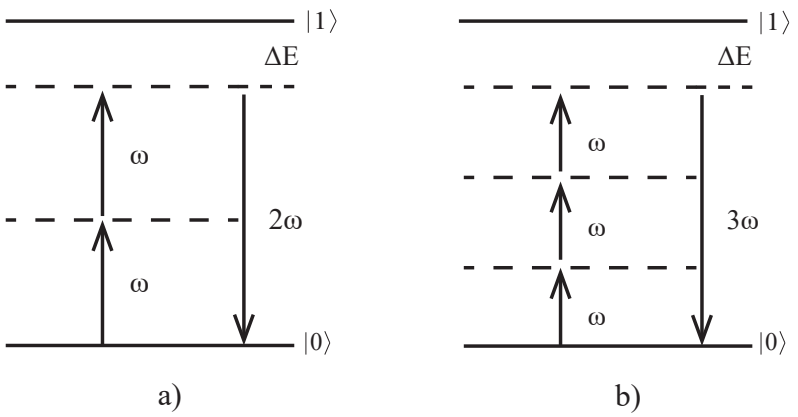

Figure 3.12: a) Second-Harmonic Generation (SHG); b) Third-Harmonic Generation (THG) [43].

The theoretical treatment in the quantum mechanics description of NLO phenomena requires the solution to the time-dependent Schrödinger equation by the density matrix formalism and the use of approximation methods such as the quantum theory of perturbations, among other considerations.

3.3. Third-Order optical response of metal NPs

This section presents a brief qualitative descriptions of a number of third-order nonlinear optical properties of metal-dielectric nanocomposite materials. These properties depend significantly on many factors regarding both the materials themselves (metal and host medium types, metal concentration, particle size, shape and spatial arrangement) and the excitation laser (wavelength, intensity, pulse width) [44].

3.3.1. Optical Kerr effect in nanocomposites media

Let's consider the third-order contribution to the nonlinear polarization $\widetilde{\mathbf{P}}^{(3)}(t) = \epsilon_0 \chi^{(3)} \widetilde{\mathbf{E}}^3(t)$, for the general case in which the optical field $\widetilde{\mathbf{E}}(t)$ is made up of several different frequency components, the expression for $\widetilde{\mathbf{P}}^{(3)}(t)$ is very complicated. Now, the simple case in which the applied optical field is monochromatic is given by [39]:

$$\widetilde{\mathbf{E}}(t) = E \cos \omega t \tag{3.34}$$

Then, taking into account that $\cos^3 \omega t = \frac{1}{4} \cos 3\omega t + \frac{3}{4} \cos \omega t$, the nonlinear polarization can be expressed as:

$$\widetilde{\mathbf{P}}^{(3)}(t) = \frac{1}{4} \epsilon_0 \chi^{(3)} \cos 3\omega t + \frac{3}{4} \epsilon_0 \chi^{(3)} \cos \omega t \tag{3.35}$$

here, the first term describes a response at frequency 3ω that is due to an applied optical field at frequency ω, this term leads to the process of THG, the second term describes a nonlinear contribution to the polarization at the frequency of the optical field; this contribution to the polarization induces a modification of the wave propagation in the material, for both its amplitud and phase, but without any frequency change [39, 44]. This phenomenon is known as the optical Kerr effect, by analogy with the electro-optic Kerr effects where the medium refractive index varies proportionally with the square of the applied electric static field.

In the case of a Kerr-type nonlinear response the dependence of the refractive index and the absorption coefficient on the intensity of light, I, can be expressed as:

$$\begin{aligned} n &= n_0 + \gamma I \\ \alpha &= \alpha_0 + \beta I \end{aligned} \tag{3.36}$$

where n_0 and α_0 are the linear refractive index and linear absorption coefficient, respectively, γ is the nonlinear refractive index, while β is the nonlinear absorption coefficient.

In a system showing a negligible absorption $\alpha_0 \approx 0$, γ and β are proportional to the real $\chi^{(3)}_{Re}$ and imaginary $\chi^{(3)}_{Im}$ parts of $\chi^{(3)}$ through the following expressions [44, 45]:

$$\begin{aligned} \chi^{(3)}_{Re} &= \frac{4}{3}\, n_0^2\, \epsilon_0 c \gamma \\ \chi^{(3)}_{Im} &= \frac{n_0^2\, \epsilon_0 c \lambda}{3\pi} \beta. \end{aligned} \tag{3.37}$$

For the case where the absorption is not negligible, the relationship between γ and β and third-order nonlinear susceptibility can be found to be given by [44, 45]:

$$\begin{aligned} \chi^{(3)}_{Re} &= \frac{2\epsilon_0 c n_0}{3} \left(2 n_0 \gamma - \frac{\alpha_0 \beta \lambda^2}{8\pi^2} \right) \\ \chi^{(3)}_{Im} &= \frac{2\epsilon_0 c n_0 \lambda}{3\pi} \left(n_0 \beta + \alpha_0 \gamma \right) \end{aligned} \tag{3.38}$$

Linear absorption in materials containing metal NP is, most of the time, absolutely not negligible, and equation 3.38 has to be used instead of equation 3.37.

In equations 3.37 and 3.38 the different quantities are expressed in SI units; however, the third-order nonlinear susceptibility is often expressed in electrostatic units (esu):

$$\chi^{(3)}(\text{esu}) = 10^{-}8\, \frac{c^2}{4\pi} \chi^{(3)}(\text{SI}) \tag{3.39}$$

In addition, the nonlinear optical coefficients γ and β are often expressed in the submultiple units cm^2W^{-1} and cmW^{-1}, respectively.

3.3.2. The case of nanocomposite materials

As for the linear optical response, several approaches have been proposed to describe the NLO properties of nanocomposite media; however, general principles can be identified. First, each component of a nanocomposite posses its own susceptibility; moreover, as the typical structure size is much smaller than wavelength, the observable result of light interaction with the nanocomposite is different from a simple combination of the individual responses of the separated constituents.

Secondly, the local electromagnetic field enhancement in the metal NP due to the LSPR is resposible for the large enhancement of the metal nonlinear optical response. Many studies have shown that the optical nonlinearities in nanocomposite materials originate from particles and not from their host matrix; however, if the metal nonlinear response is indeed much larger than the matrix one, it is further amplified by the LSPR phenomenon which depends significantly on the dielectric contrast between the particles and the host medium. In this way, metal alone cannot explain by itself the high nonlinear response of nanocomposite materials.

Thirdly, the intrinsic nonlinear optical susceptibility of a small particle might be different from the bulk metal one, due to finite size effects as mentioned in the section 2.7 for the linear response [44].

Many times, the nanocomposite materials studied in experiments contain metal inclusions, which nonlinear susceptibility is much larger than the one of the surrounding host matrix. For low metal concentrations ($< 10\%$) and assuming that the third-order nonlinear susceptibility of metal, $\chi_m^{(3)}$, is the same for all inclusions of the medium and constant in each of them, then, the effective susceptibility of the nanocomposite material is given by [46–48]:

$$\chi^{(3)} = pf^2 \mid f \mid^2 \chi_m^{(3)} \tag{3.40}$$

where p is the volume fraction of metal particles embedded, $f = \frac{E_i}{E_0}$ is the local field factor (E_i is the local field, E_0 is the macroscopic field). f can be expressed as follows when the metal particles are considered spherical:

$$f = \frac{3\epsilon_h}{\epsilon_m + 2\epsilon_h} \tag{3.41}$$

here, ϵ_m and ϵ_h are the dielectric functions of metal and host medium, respectively. The equation 3.40 is extensively used in the literature to analyze the nonlinear optical properties of nanocomposite materials determined experimentally.

3.3.3. Self - Focusing

One of the processes that can occur as a result of the optical Kerr effect is self-focusing. This process can occur when a beam of light having a nonuniform transverse intensity distribution (like a laser beam with gaussian distribution) propagates through a material in which γ is positive. Along these conditions, the material effectively acts as a positive lens, which causes that the rays curve toward each other. If the medium is short enough, this focus will occur outside of the medium as shown in the figure 3.13.a; nevertheless, if the medium is sufficiently long or even if the beam intensity is sufficiently large, the focus will occur within the nonlinear medium as shown in the figure 3.13.b [39].

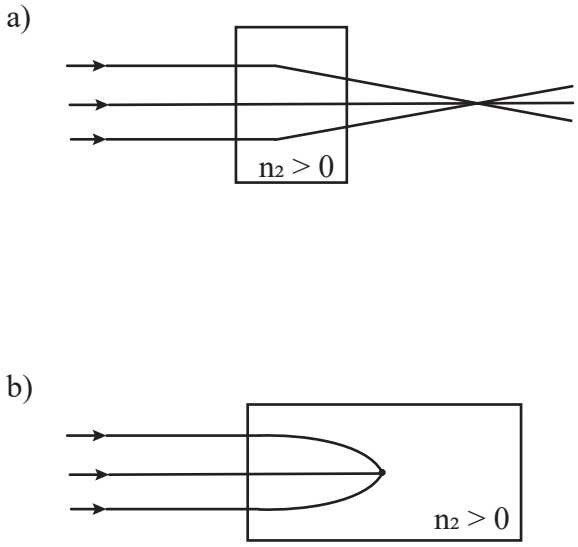

Figure 3.13: Self - focusing of light [39].

3.3.4. Saturation of absorption

Depending on the material characteristics and experimental conditions, that is, on laser wavelength and power as well as on the type of metals and their relative amount, the nonlinear absorption coefficient β can be either negative or positive. For the case when $\beta < 0$, nanocomposite materials might have the property that their absorption coefficient decreases when measured using high laser intensity, this process is called saturation of absorption (SA). Often the dependence of the measured absorption coefficient α on the incident light intensity I through:

$$\alpha(I) = \frac{\alpha_0}{1 + I/I_s} \tag{3.42}$$

where I_s is defined as the saturation intensity [39].

3.3.5. Optical bistability

Optical bistability is a nonlinear process where for the same optical input intensity in a material, there are two possible output intensities and it is a consequence of SA. The more general term optical multistability is used to describe the circumstance in which two or more stable output states are possible. Optical bistability allows the design of optical logical circuits and will play a fundamental role in the development of optical communication and optical computing. A bistable optical device can be made by placing a SA inside a Fabry-Perot resonator, as shown the figure 3.14. As the input intensity is increased, the field inside the cavity also increases, lowering the absorption that the field experiences and thus increasing the field intensity still further. Now, if the intensity of the incident field is subsequently lowered, the field inside the cavity tends to remain large due to the absorption of the material system has already been reduced [39]. The process of optical bistability can be further studied with more detail in reference: [39] (section 6.3).

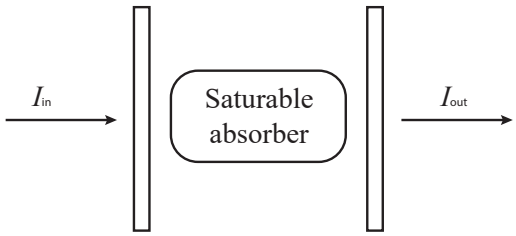

Figure 3.14: Bistable optical device [39]

CHAPTER FOUR

Experimental Techniques

This chapter describes in detail the experimental techniques used for sample preparation and characterization. A good understanding of such techniques allows a correct analysis of the samples and the results. Particularly, in this work a novel approach has been developed to obtained monodisperse spherical silica particles of large size with high shape quality and narrow size distribution, This is important because NSL requires spheres uniformly ordered of high quality for better results. This method which we will refer to as LIT-synthesis is described below.

4.1. LIT-Synthesis

Usually, the most used method for the synthesis of silica particles is the Stöber method described in the Chapter 1; nevertheless, the silica synthesis from TEOS precursor has many drawbacks because it is highly sensitive not only to the reagent concentrations, but also to environmental conditions. The so-called Stöber reactions are facilitated by the hydrolysis and condensation of TEOS in absolute ethanol (EtOH) with ammonia (NH_3) as the base catalyst [5]. This mechanism allows the formation of essentially monodisperse spherical SiO_2 particles. The spherical shape and a narrow size distribution are important issues in preparing silica particles, thus, looking for a regular morphology and a narrow size distribution, the monodispersity of the synthesized silica particles is considered as the high-quality factor. A number of modified Stöber synthesis methods have been developed to improve these

characteristics at reaction temperatures higher than 30°C [49–51]. Gao *et al.,* proposed to control the silica particle size by varying only the volume of the ethanol solvent and fixing the other reaction conditions. Besides, they presented a simple exponential equation to determine the particle size with just one parameter, the ethanol volume [51]. For this thesis, the modified Stöber method proposed is keeps the initial temperature of the reagents at low values ($6 - 14$°C) while fixing the other parameters, such as room temperature, humidity and reagent concentrations.

4.1.1. Experimental details

Reagents

The reagents necessary for LIT-synthesis are the following:

* Tetraethyl - orthosilicate ($Si[OC_2H_5]_4$, TEOS, 99.999%).

* Ethanol (C_2H_5OH, 99%).

* Ammonium hydroxide solution (NH_4OH, $28 - 30$%).

* Distilled water.

Preparation of monodispersed silica particles

The important novel aspect of the "low initial temperature synthesis (LIT-synthesis)", is to keep, previously to the synthesis reaction, the two prior prepared reagent solutions at low temperature (T_{LIT} from 6°C to 14°C), while maintaining constant the other parameters during the reaction, such as the room temperature (RT = 18°C), humidity and the reagent concentrations. The reaction mixture containing TEOS as a precursor, ethanol as solvent, distilled water as a hydrolyzing agent, and ammonium hydroxide as a catalyst for the hydrolysis and condensation of the alkoxide. First, a solution (1) containing 1.8 ml of TEOS and 20 ml of EtOH is mixed via magnetic stirring and cooled by using a homemade heat

exchanger. Then, a second solution (2) containing 5.5 ml of ammonium hydroxide in 8 ml of distilled water is cooled to the same temperature as the previous solution by means of a cold bath. Once both solutions reached the same temperature (T_{LIT} = 6, 8, 10, and 14°C), the heat exchanger for the solution (1) is set apart before the beginning of the synthesis procedure. As the synthesis reactions takes place by dripping the solution (2) into (1) at a rate of 30 drops per minute one can observe that the reaction temperature varies freely, and it can be monitored as a function of time. Finally, in order to ensure a homogeneous mixing, the reaction is maintained under constant stirring for 24 hours (Fig. 4.1).

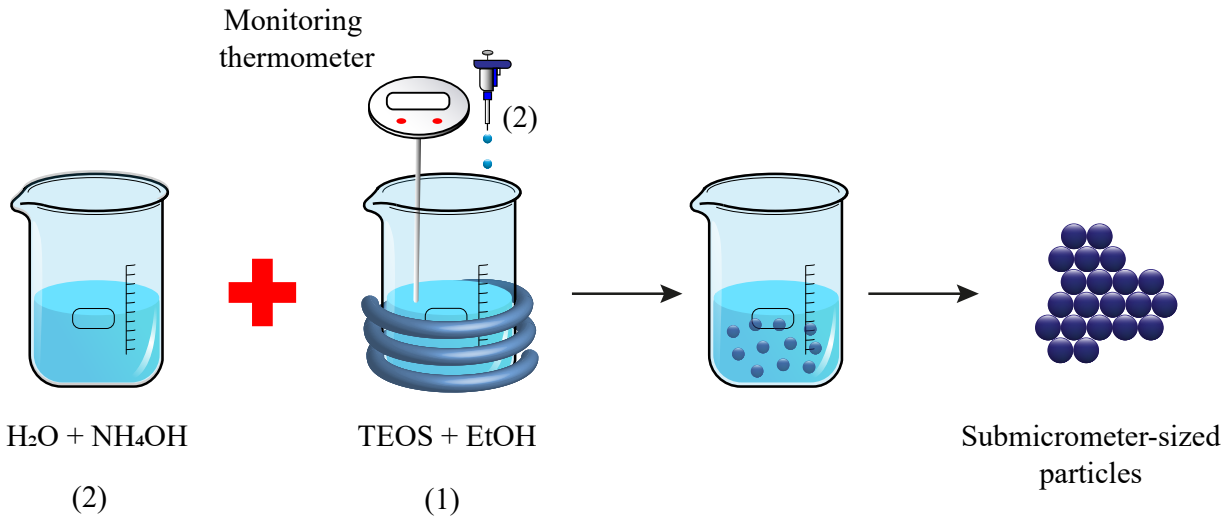

Figure 4.1: Diagram of LIT-Synthesis process.

4.2. Nanosphere Lithography

J.C Hulteen and R.P Van Duyne developed the Nanosphere Lithography (NSL) in 1994 [52]. NSL is a low-cost technique that allows to fabricate 2D ordered superficial arrays of metallic nanostructures, this approach is based on the presence of channels in one or even two close-packed layers of nano or microspheres. This process is very versatile and simple that offer nanometric resolution that compared to others lithographic techniques such as electron beam lithography [53], X-ray lithography [54], NSL is faster and at relatively low cost.

The process is divided into two steps [2] (Fig. 4.2):

1. *Mask preparation* - The flat substrate is coated with a suspension containing monodisperse spherical colloids (*e.g.*, polystyrene or silica after a chemical treatment to enhance its hydrophilic character. Upon drying, a hexagonal-close-packed (HCP) monolayer or bilayer, called a colloidal crystal mask, is formed. This mask is then used to selectively pattern the substrate thanks to the deposition of the material of interest through the interstices of the ordered spheres.

2. *The nanostructures* - The subsequent removal of the mask (lift-off) by sonication in an adequate solvent or by mechanical removal leaves an array of ordered nanoprisms for monolayers made with a single-layered colloidal mask or nanodots made with a double-layered.

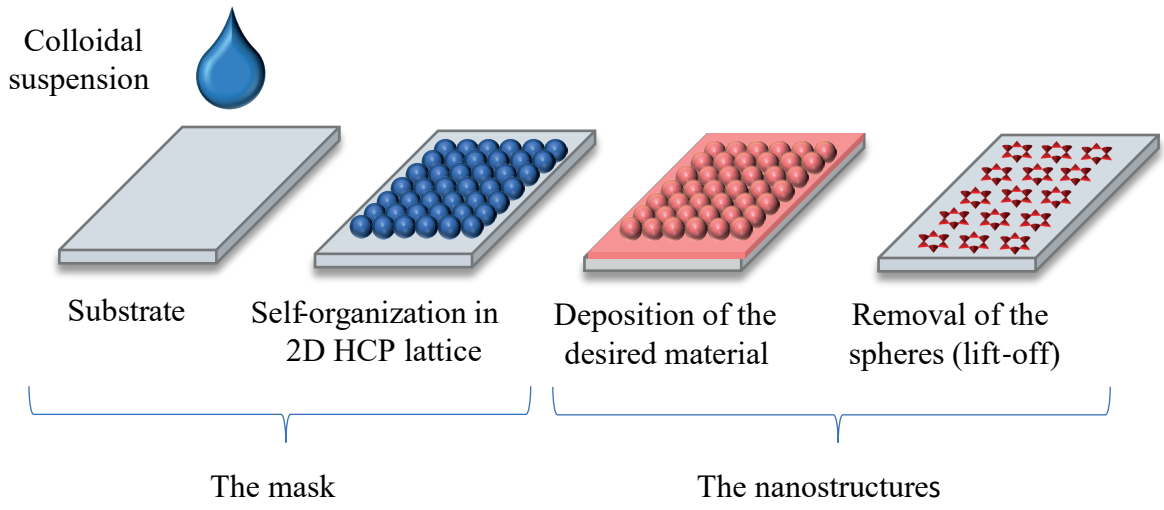

Figure 4.2: Nanosphere lithography process (NSL).

The NSL is considered as a hybrid between the bottom-up approach (due to the self-organization of the colloidal spheres in a HCP lattice) and the top-down approach (due to the obtaining of dots/structured layers such as in a conventional lithography technique).

4.2.1. Mask fabrication methods

There are different strategies to improve the quality of the mask of sub-micrometer spheres, and they will be briefly described below [2]:

Self-Assembly during Solvent Evaporation - This method is based on solvent evaporation from a droplet of dilute colloidal suspension deposited on a substrate. A pioneer work on this method was proposed by Denkov *et al.*, where regular arrays of colloidal latex polystyrene particles were obtained by evaporation of drops of suspensions on solid substrates [55]. The evaporation of the solvent induces the formation of a meniscus between the particles and therefore attractive capillary forces give rise to the self-assembly of the particles, while the ordering and quality of the obtained arrays are considerably affected by the rates of solvent evaporation. As theoretically shown by Kralchevsky and Denkov [56] interparticle capillary forces arise between spherical particles, which are partially immersed in a liquid on a horizontal solid substrate. As the liquid becomes thinner, the liquid surface deformation increases giving rise to increases capillary forces (F_c). The next step begins with the motion of more particles that are driven toward the nucleus for a hydrodynamic force (F_d) that is caused by a hydrodynamic flux (J_s), which compensates the evaporated solvent in the already ordered array (Fig. 4.3). According to Denkov *et al.*, the onset of ordering process coincides with the moment when the thickness of the liquid layer containing the particles becomes smaller than the particle diameter [55].

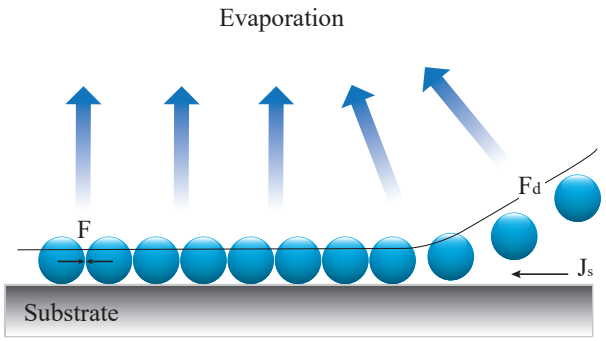

Figure 4.3: Main driving forces in evaporation process.

Dip Coating - Nagayama *et al.*, developed a dip-coating procedure for formation of 2D colloidal templates [57]. Constant monitoring of the evaporation rate as well as fine-tuning of the withdrawal speed of the substrate are key parameters to achieve large 2D ordered arrays, the mechanism is quite simple, to initiate and maintain a linear growth of thin particle arrays is to dip a clean solid plate into a suspension of particles, then, the monolayers begin to form on the plate surface from the plate-suspension-air interface, finally, the substrate is carefully removed from the suspension.

Langmuir-Blodgett - The LB methodology consists on the transfer process from the air - water interface onto a solid substrate of a monomolecular layer of amphiphilic material adsorbed at the air - water interface. The amphiphilic material is dissolved in a volatile solvent and dropped on the air - water interface. After the spreading, the solvent evaporates and the material forms a monolayer. When the monolayer reaches the thermodynamic equilibrium, it is symmetrically compressed by using two barriers. To transfer the film onto the solid, a flat substrate is immersed into the aqueous subphase and then extracted in a controlled way with the film adsorbed onto it. The transfer process can be repeated many times to obtain multilayers of different thickness and composition. During the transfer process, the surface pressure is maintained constant by barrier compression in order to compensate the loss of molecules transferred onto the solid [58]. This method has been used for to form large areas of monolayers of silica particles [59] (Fig 4.4).

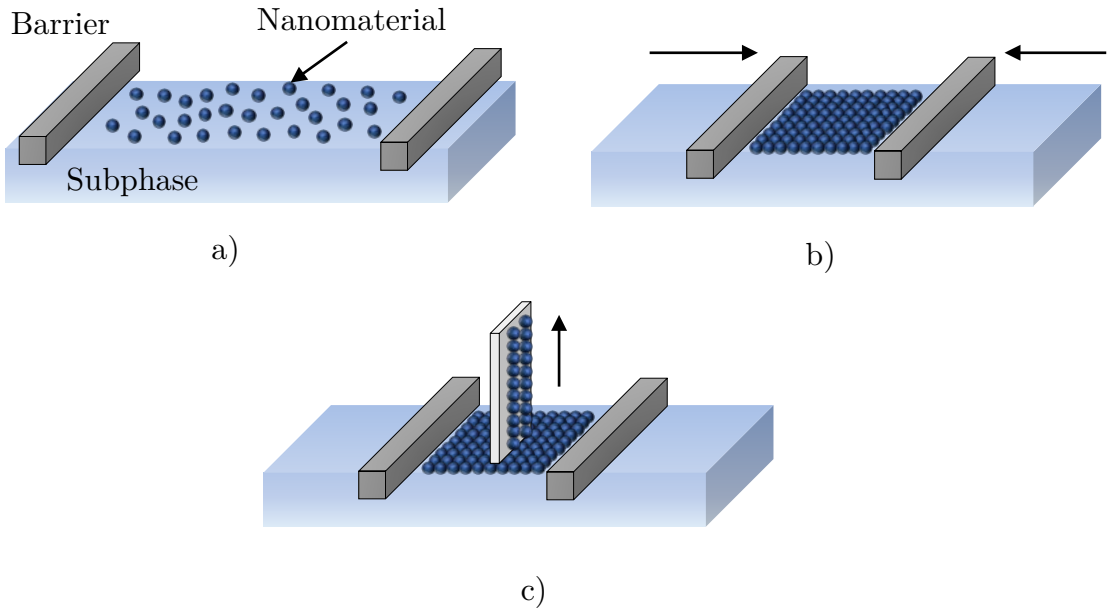

Figure 4.4: Langmuir-Blodgett technique for nanomaterials: a) monolayer spreading at the air - water interface; b) schematic illustration of compression of nanomaterials by two barriers motion at the air - water interface, and c) the monolayer transfer by vertical dipping.

Spin coating - Since the first studies done by Emslie *et al.,* [60] Spin coating technique has taken on importance in the industry and the science in general. This technique is widely used commercially to deposit polymer films for lithography, epitaxial films, it has also been used to deposit organic semiconductor films and has become the preferred deposition method for perovskite materials such as $CH_3NH_3PbI_3$ and $CsPbBr_3$ for use in solar cells, photodetectors, and light-emitting diodes (LEDs), and so on [17, 61–68]. This technique is a simple, convenient, cheap, material saving, rapid and highly reproducible method to produce homogeneous films on a rigid flat or slightly curved substrate.

Spin coating process for a colloidal suspension exhibit four distinct stages of development [69], the first two happening rapidly and the second two occurring over a much longer time period. In the first stage, a colloidal fluid is deposited as a droplet onto a fixed sub-

strate. In the second stage “spin up”, the substrate is accelerated to a prescribed rotational speed and the liquid droplet spreads out to form a film that rotates at nearly the same rate as the substrate. In the third stage “spin off”, this film spreads outward and thins, controlled primarily by centrifugal force and viscous force. In the fourth stage, the film becomes sufficiently thin that evaporation dominates, slimming down the film even more (see Fig. 4.5).

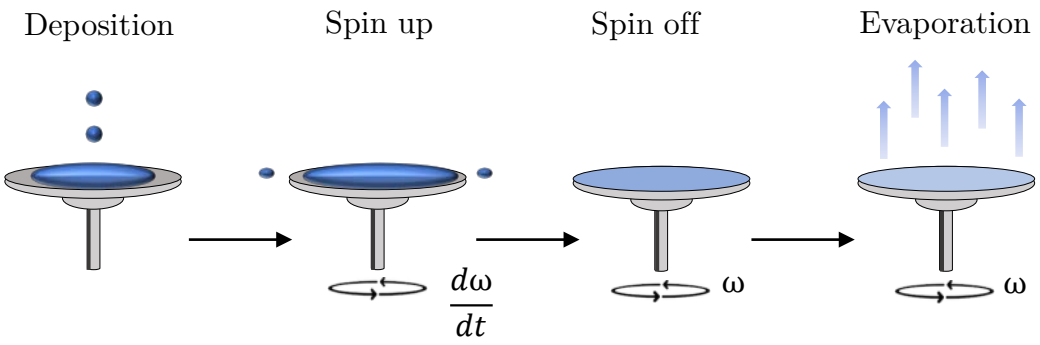

Figure 4.5: Spin-coating stages

The dominating force F for the fabrication of the self-assembled colloidal crystals can be described as follows [69]:

$$F = F_{cent} + F_{evap} + F_{cap} + F_{p-p} + F_{p-s} \tag{4.43}$$

where F_{cent} is the centrifugal force, F_{evap} is the fluid force by evaporation, F_{cap} is the capillary force, F_{p-p} is the interparticle interaction force, and F_{p-s} is the interaction force between the particle and the substrate. Spin coating has a significant potential for mass production and scaling-up due to its rapid implementation and its compatibility with wafer-scale processes.

The physical treatments the sol or gel might have undergone can lead to a substantial impact on the final gel structure [21]. Therefore, taking into consideration how the rate of evaporation during gelation can affect the quality of the silica particle monolayer, a new approach during the spin coating deposition was used in this thesis.

4.2.2. Self-assembly of silica particles onto silicon and fused silica substrates

Once obtained the colloidal SiO_2 particles, they are deposited onto crystalline silicon wafers (1 cm^2) and high-purity fused silica plates ($5 \times 5 \times 1$ mm), previously cleaned by means of a chemical treatment known as the piranha solution. This cleaning treatment consists in preparing a dissolution of sulfuric acid (H_2SO_4, $95 - 98\%$ purity) and hydrogen peroxide (H_2O_2, 30% purity) with a $3:1$ proportion. All the cleaning process is performed at 100°C on a hot plate with magnetic stirring, with the substrates immersed in the solution for 30 minutes. Finally, they are washed with ultrapure Milli-Q water and ethanol, leaving the samples in ethanol for 24 hours. Afterward, to improve the quality of the monolayer of silica particles deposited on the substrates, a novel technique is utilized. First, $5 - 10$ μl volume of the synthesis solution is deposited onto the substrates, placed inside of a plastic closed box. Immediately, the sample is put to rotate through the spin coating system (G3 Model from Specialty Coating Systems) at 500 rpm for 1 minute. Finally, without opening the box, the sample is left to dry at room temperature (Fig. 4.6).

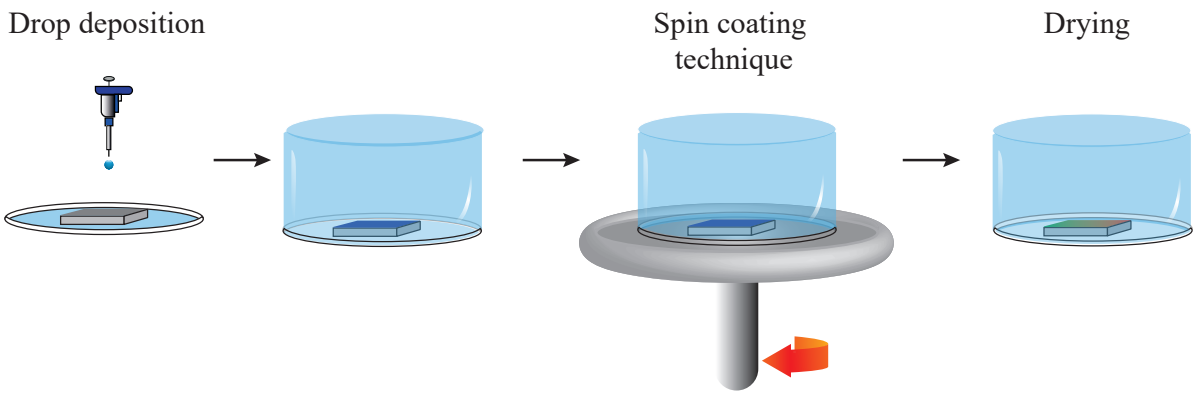

Figure 4.6: Schematic of the deposition process.

4.3. Scanning Electron Microscopy (SEM)

The Scanning Electron Microscopy (SEM), which was developed by Max Knoll and Ernst Ruska, is a type of electron microscopy that uses a focused beam of electrons to generate a variety of signals at the surface of samples. The electron-sample interactions reveal information about the sample such as: morphology, chemical composition, crystalline structure and orientation. Mainly the work done on a SEM is for obtaining topographical information, which is mainly provided by secondary electrons.

The main components of an electronic microscope are [70]:

1. *Vacuum system* - A vacuum system is required when using an electron because electrons will quickly disperse or scatter due to collisions with other molecules.

2. *Electron beam generation system* - This system provides the beam of electrons known as the primary electron beam.

3. *Electron beam manipulation system* - This system consist of electromagnetic lenses and coils that control the size, shape and position of the electron beam that reaches the sample surface.

4. *Beam sample interaction system* - This system involves the interaction of the electron beam with the sample and the types of signal that can be detected.

5. *Detection system* - This system can consist of several different detectors, each sensitive to different energy/particle emissions that occur on the sample.

6. *Signal processing and display system* - This system is an electronic system processes the signal generated by the detection system and allows additional electronic manipulation and visualization of the image.

The morphology characterization of the silica microparticles was performed by means of scanning electron microscopy (SEM, JEOL JSM-7800F) available at the Instituto de Física (Fig.4.7).

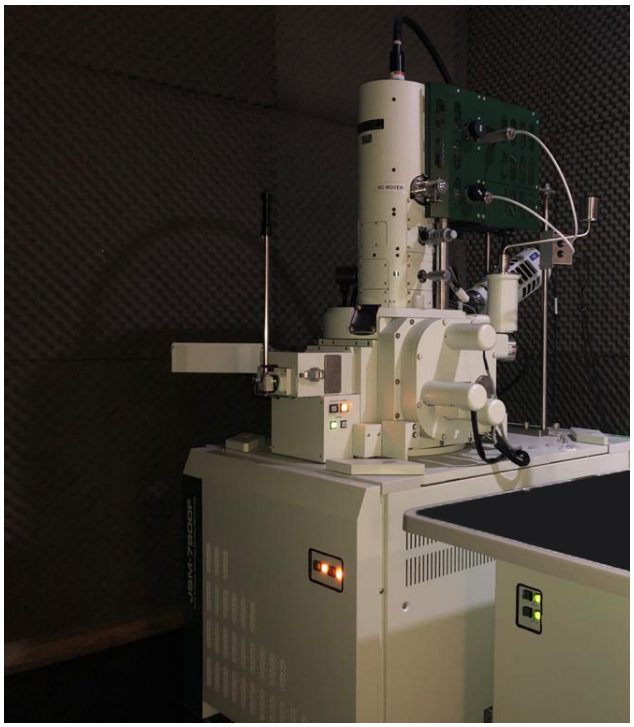

Figure 4.7: An overview image of the SEM, JEOL JSM-7800F.

4.4. Ion Implantation

Ion beam processing of materials results from the introduction of atoms into the surface layer of a solid substrate by bombardment of the solid with ions in the electron-volt (eV) to mega-electron-volt energy range (MeV). The use of energetic ions affords the possibility of introducing a wide range of atomic species, independent of thermodynamic factors, thus making it possible to obtain impurity concentrations and distributions of particular interest, as in many cases, these distributions would no otherwise be attainable [71].

Ion beam processing provides an alternative and non-equilibrium method of introducing dopant atoms into the lattice. The basic elements required in this technique are: ion source, acceleration column, mass-separator, and target chamber.

Ion implantation is performed at the Marcos Mazari Accelerator Laboratory located at the Instituto de Física of the Universidad Nacional Autónoma de México. A 3 MV Tandem accelerator (NEC 9SDH2) is used both to modify and characterize samples (Fig.4.8).

Figure 4.8: An overview image of the 3 MV Pelletron accelerator. The ion sources are located on the top left corner, followed by the main tank on the middle and on the far right the experimental research lines.

The production of a negative ion beams obtained from the Source of Negative Ions by Cesium Sputtering (SNICS). In the SNICS source a cathode is eroded by heated cesium atoms accelerated through a potential difference, successfully extracting negative ions. The extracted negative ion beam is then introduced into the main tank of the accelerator after passing through an electromagnet selector. The first acceleration stage of the ion beam is performed as it approaches the high voltage terminal. The high voltage (HV) terminal is obtained from a pellet charging system and the kinetic energy of the ion beam now has

an energy $E = qV$, where q is the particle charge. In the terminal the accelerate negative charged ion beam passes through a neutral gas. A molecular nitrogen gas (N_2) strips electrons from the ion beam, effectively changing the ion beam from negative to positive [72].

The positive ion beam now receives a second boost. The desired kinetic energy of the ion beam is now written as:

$$E = (1 + q)V \tag{4.44}$$

where q is the charge state of the positive ion beam. Based on charge and mass, an electromagnet chooses the right ion. The ion is now focused by quadrupole lenses. In order to obtain uniform beam distribution, the ion beam is collimated with a square opening, defining the implantation area [72].

When an energetic ion impinges upon the surface of the materials, it experiences a series of inelastic and elastic collisions with the atoms which lie along the path. This results in loss of kinetic energy of the ion and excitation of the solid target as well as momentum transfer between the interacting bodies.

The energy lost by the ion as it goes trough the solid is determined by the stopping power, defined as the energy transfer per unit path length of a particle along its trajectory [71]:

$$S(E) = -\frac{dE}{dx} \tag{4.45}$$

the sign of the stopping power is negative to indicate an energy loss change along the path length. There are two main processes that contribute to the energy loss mechanism. They are, the electronic stopping power denoted as $S_e(E)$ and the nuclear stopping power denoted as $S_n(E)$, also known as the inelastic and elastic energy loss mechanism, respectively. In this way the stopping power is expressed as [73]:

$$\frac{dE}{dx} = \left(\frac{dE}{dx}\right)_e + \left(\frac{dE}{dx}\right)_n \tag{4.46}$$

The relative importance between these two mechanisms as a function of the ion energy is shown in Figure 4.9, where the $S_n(E)$ is dominant at low energies and the $S_e(E)$ is at high energies.

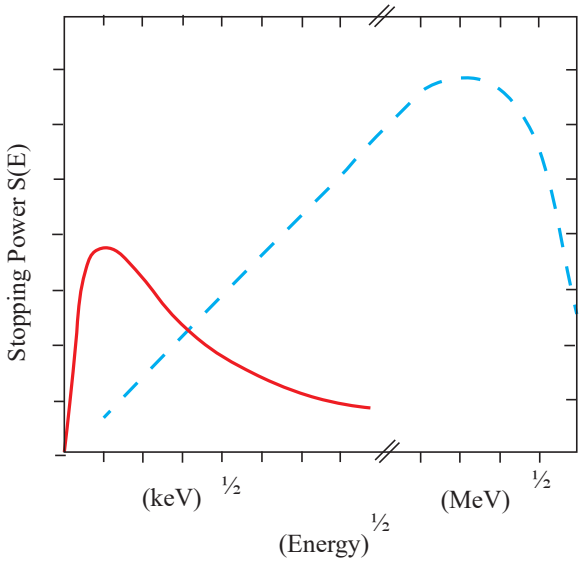

Figure 4.9: Typical dependence of the electronic and nuclear stopping of ion in matter with respect to energy.

4.4.1. Distribution range

One of the most important considerations in any description of ion-solid interactions is the depth (range) distribution of the implanted ions. As the incident ion travels into the solid matrix, it does not move to its resting place in a straight line due to multiple collisions with the substrate atoms. The implanted range $R(E)$ defines the total integrated distance the ion travels through the solid before coming to rest, it is given as [74]:

$$R(E) = \int \frac{dE}{S_n(E) + S_e(E)} \tag{4.47}$$

where $S_n(E)$ and $S_e(E)$ are the nuclear and electronic sttoping powers respectively.

As a result, ions with the same energy, incident with the same angle onto the sample surface, and into the same material, do not necessarily have the same range. However, the ion distribution obtained after implantation can be approximated by a Gaussian distribution and may therefore be characterized by a projected range, R_p, and a straggling, ΔR_p, about this mean value, as shown in Figure 4.10. The notation uses Z and M for atomic number and atomic mass, respectively, with subscript 1 denoting the incident ions (Z_1, M_1), subscript 2 denoting the ion-bombarded sample and the energy of the incident ion is denoted by E [71].

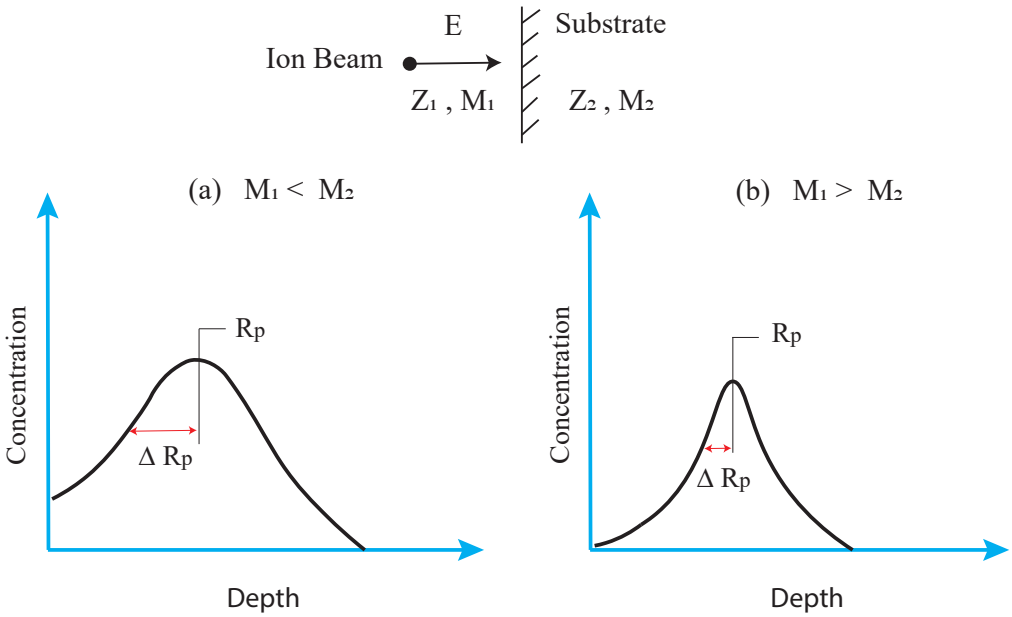

Figure 4.10: The depth distribution of implanted atoms in an amorphous target for the cases in which the ion mass is (a) less than the mass of the substrate atoms or (b) greater than the mass of the substrate atoms. To a first approximation, the mean depth, R_p, depends on ion mass, M_1, and incident energy, E, whereas the relative width, $\Delta R_p/R_p$, of the distribution depends primarily on the ratio between ion mass and the mass of the substrate ion, M_2 [71].

Figure 4.10 shows the variation $R(E)$, $R_p(E)$ and $\Delta R_p(E)$. The mean depth R_p depends on the ion mass M_1 and the incident energy E_1, whereas the relative width ΔR_p of the distribution depends on the ratio between ion mass and mass of substrate [71].

The concentration $N(x)$ is the implant density given by:

$$N(x) = \frac{\Phi}{\Delta R_p \sqrt{2\pi}} \exp\left[-\frac{(x - R_p)^2}{2(\Delta R_p)^2}\right] \tag{4.48}$$

where Φ is the ion dose that is defined as the number of ions cm^{-2} implanted into the sample. Alternatively, the term *fluence* is used instead of dose.

4.4.2. Stopping and range of ions in matter (SRIM) simulations

After understanding the theory of ion implantation, it was necessary to know the effect it produces in the material (SiO_2) used in this study. To understand the phenomena that take place during SiO_2 ion implantation with gold (Au) ions, computer simulations were carried out using the SRIM (Stopping and Range Ions in Matter) code. It is a Monte Carlo computer simulation developed by James F. Ziegler and Jochen P. Biersack around 1983 [74].

The SRIM-2013 version was used in this work to perform calculations in order to determine the depth distribution and collision details of the Au ion implanted, the simulation indicates that, for 2 MeV Au^+ ions, the projected range in silica ($\rho = 2$ g/cm^3) is about 500 nm, with SD= 9 nm as shown in Figure 4.11.

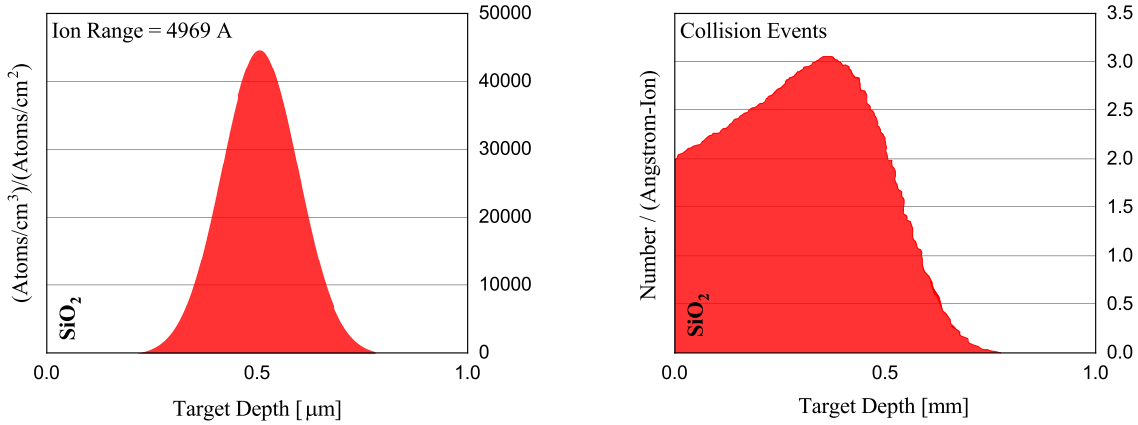

Figure 4.11: SRIM simulation at 2 MeV Au^+ ions with normal incidence in SiO_2; a) The ion range and b) Number of primary atom displacements (vacancies) per ion and unit length ($\AA$).

4.4.3. Au nanoparticle formation by ion-implanted on silica substrates

Gold nanoparticles embedded in fused silica plates are of great interest because of the nonlinear response enhancement due to the presence of plasmonic effects associated with the LSPR. In recent years, these types of structures have been prepared using different techniques such as magnetron sputtering, laser ablation, ion implantation, among others [6–11]. Ion implantation of noble metals (Au, Ag, etc.), followed by thermal annealing in different atmospheres, turns out to be an adequate technique for synthesizing metallic NPs, with spherical geometries, embedded in dielectrics.

4.5. Rutherford Backscattering Spectrometry (RBS)

Rutherford Backscattering Spectrometry (RBS) is a widely used nuclear method for the near surface layer analysis of solids. A target is bombarded with ions at an energy in the MeV-range (typically 0.5 - 4 MeV), and the energy of the backscattered projectiles is recorded with an energy sensitive detector. RBS allows the quantitative determination of

the composition of a material and depth concentration profiling of individual elements with a nanometric depth resolution [75–77].

RBS is based on the elastic collision between a high-energy beam of light ions, typically $^4He^+$, and near-surface atoms of the investigated sample. The energy of the elastically backscattered ions is measured under different angles θ with respect to the direction of the incident ion beam by a detector. The measured energy E_1 depends on the mass (M_2) of sample atoms and on the depth t where the scattering process takes place. The depth can be determined by the ion energy loss on the way to and from the point of scattering interaction with the target atom (see Fig. 4.12) [76, 77].

The element identification of a target atom requires the knowledge of the so-called kinematic factor K. This factor is defined by the ratio between energies of the primary ion after the collision E_1 and before the collision E_0:

$$K \equiv \frac{E_1}{E_0} \tag{4.49}$$

The kinematic factor can be derived assuming binary elastic collision of the projectile with the target atom, as shown in Figure 4.12. Taking into account the conservation of energy and momentum, the factor K for an ion with mass M_1 scattered at an angle θ by a target atom with mass M_2 can be expressed by the following equation [76]:

$$K(\theta, M_1, M_2) = \left(\frac{M_1}{M_1 + M_2}\right)^2 \cdot \left(\cos\theta + \sqrt{\left(\frac{M_2}{M_1}\right) - \sin^2\theta}\right)^2 \tag{4.50}$$

From the equation 4.50, for elastic scattering the factor K is independent of the incident ion energy E_0 and depends only on the mass ratio M_1/M_2 and the scattering angle θ.

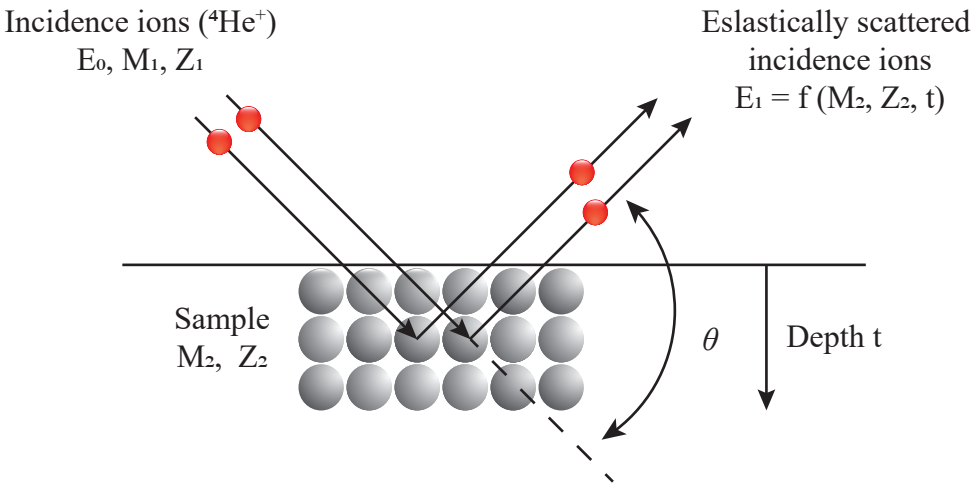

Figure 4.12: Physical principle of Rutherford backscattering [76].

In this work, RBS was used to determinate Au depth profile using our NEC 9SDH2 Pelletron facility with $^4He^+$ ions in the $3-4$ MeV energy.

4.6. Optical absorption spectroscopy

Absorption spectra are usually registered by instruments known as spectrometers. The basic function of a spectrometer is to take light, break it into its spectral components, digitize the signal as a function of wavelength, and read it out and display it through a computer. The first step in this process is to direct light from through a fiber optic into the spectrometer through a connector and a narrow aperture known as an entrance slit. The size of the aperture regulates the amount of light that enters the optical bench and controls spectral resolution. In most spectrometers, the divergent light is then collimated by a concave mirror, the collimating mirror reflects photons to a diffraction grating, which splits photons by wavelength, the diffraction grating then spreads light across by a second concave mirror, which directs the light at each wavelength onto the detector.

Once the light is imaged onto the detector the photons are then converted into electrons which are digitized and read out through a USB (or serial port) to a computer. The software then interpolates the signal based on the number of pixels in the detector and the linear dispersion of the diffraction grating to create a calibration that enables the data to be plotted as a function of wavelength over the given spectral range. Figure 4.13 shows the main components of a spectrometer.

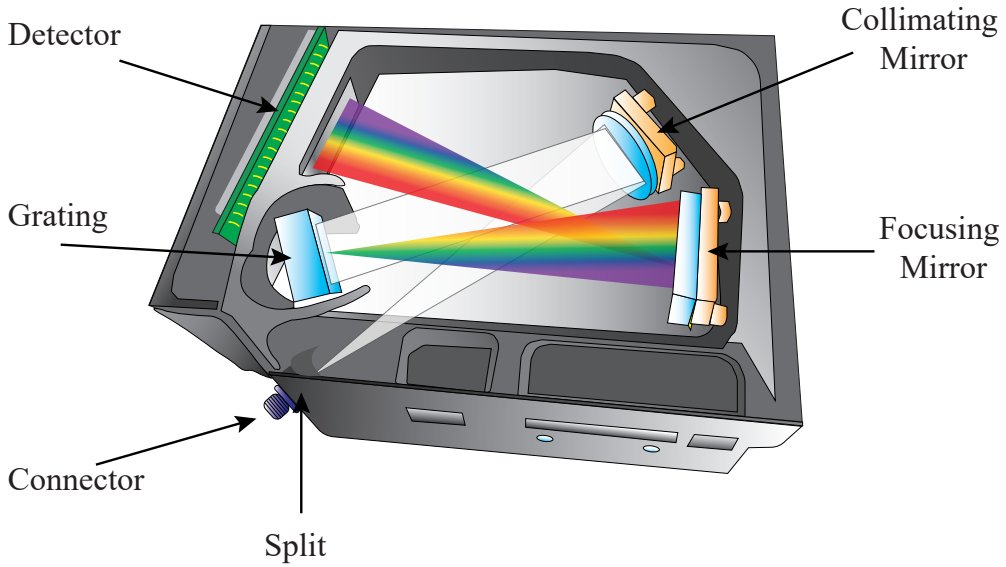

Figure 4.13: Inside the optical bench of a spectrometer.

Figure 4.14 shows a schematic diagram with the main elements of an optical absorption experiment, this experiment basically consists in the following: a light source (usually a deuterium lamp for the UV spectral range and a tungsten lamp for the VIS and IR spectral ranges) which is focused on the sample by an optical fiber. The light interacts with the sample, then another optical fiber collects and transmits the result of the interaction to the spectrometer. Afterwards the spectrometer measures the amount of light and transforms the data collected by the spectrometer into digital information, finally the spectrometer passes the sample information to PC that displays the processed spectral information.

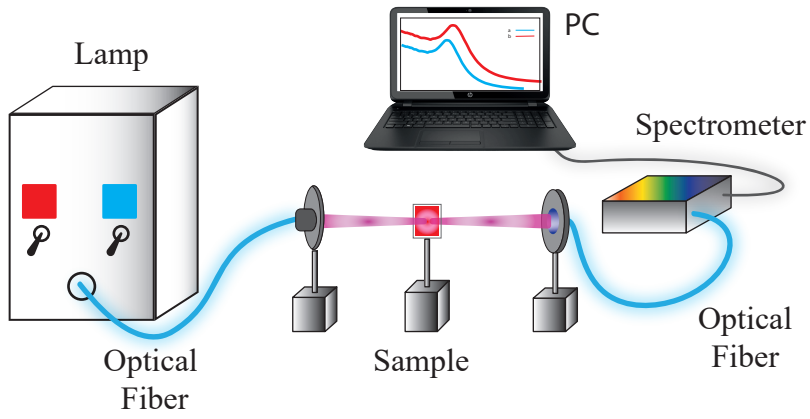

Figure 4.14: Schematic diagram of optical absorption experiment.

In the optical extinction measurements, the value that is often measured is the optical density that is defined as [31]:

$$\mathrm{OD} = \log\left(\frac{I_0}{I}\right). \tag{4.51}$$

According to equation 2.14 the absorption coefficient is determined by:

$$\alpha = \frac{\mathrm{OD}}{x \log e} = \frac{2.303(\mathrm{OD})}{x}. \tag{4.52}$$

It is important to emphasize the advantage of measuring optical density spectra over transmittance or absorbance spectra. Optical density spectra are more sensitive because they provide greater contrast than absorbance or transmittance spectra [31]; moreover, we can found a dependent function of the light frequency which is closely related with the surface plasmon that in turn is linked to the characteristics of nanocomposites. In this work the optical extinction measurements were performed with:

* Ocean Optics USB SD2000 spectrometer.

* Deuterium - halogen dual lamp in the $350 - 800$ nm wavelength range.

and according to the scheme in Figure 4.14.

4.7. Z-scan technique

In 1989 Sheik *et al.,* [78] proposed a simple experimental technique to measure intensity dependent nonlinear susceptibilities of optical materials that exhibit a large third-order optical nonlinearity. The technique has become popular due to its easy implementation, the ease with which the results obtained are interpreted and the high sensitivity it offers to changes in the ONL response.

In this method, the sample is translated in the z - direction along the axis of a focused Gaussian beam. This is because the sample experiences different intensities, dependent on the sample position (z) relative to the focus $z = 0$. In this way, measuring the transmitted power (the transmittance) through the sample as a function of z - position (-z to +z). For the measurement of the nonlinear index of refraction an aperture is placed in front of the detector measuring the transmitted light. This makes the measurement of the transmittance sensitive to beam spreading or focusing and relates to a transformation of phase distortion into amplitude distortion. The configuration with the included aperture is known as close aperture Z-scan (CA Z-scan), while without aperture is called open aperture Z-scan (OA Z-scan).

4.7.1. Nonlinear refraction

The electric field $E(r,t,z)$ associated with a Gaussian beam of beam waist radius ω_0 traveling in the $+z$ direction can be expressed as [78]:

$$E(r,t,z) = E_0(t)\frac{\omega_0}{\omega(z)} \cdot \exp\left(-\frac{r^2}{\omega^2(z)} - \frac{ikr^2}{2R(z)}\right) e^{-i\phi(z,t)} \tag{4.53}$$

here, $\omega^2(z) = \omega_0^2(1+z^2/z_0^2)$ is the beam radius, $R(z) = z(1+z_0^2/z^2)$ is the radius of curvature

of the wavefront at z, $k = 2\pi/\lambda$ is the wave vector, λ is the laser wavelength and z_0 is the Rayleigh length or diffraction length of the beam defined as:

$$z_0 = \frac{k\omega_0^2}{2} \tag{4.54}$$

$E_0(t)$ denotes the radiation electric field at the focus and contains the temporal envelope of the laser pulse. The $e^{-i\phi(z,t)}$ term contains all ther radially uniform phase variations.

The analysis in Z-scan technique requires that the sample be considered "thin", *i.e.,* the sample length is small enough that the changes in the beam diameter within the sample due to either diffraction or nonlinear refraction can be neglected. In this case the self refraction is called "external self-action". For linear diffraction. this implies that $L < z_0$, while nonlinear diffraction, $L << z_0/\Delta\phi(0)$, In most Z-scan experiments the second criterion has been found to be automatically met since $\Delta\phi$ is usually small; in addition, when negligible nonlinear absorption and only a cubic nonlinearity is considered, $\Delta\phi$ at the exit surface of the sample which simply follows the radial variation of the incident irradiance at a given position of the sample z is given by [78]:

$$\Delta\phi(z, r, t) = \Delta\phi_0(z, t) \cdot \exp\left(-\frac{2r^2}{\omega^2(z)}\right) \tag{4.55}$$

with

$$\Delta\phi_0(z, t) = \frac{\Delta\Phi_0}{1 + z^2/z_0^2} \tag{4.56}$$

here, $\Delta\Phi_0$ is the on-axis phase shift at the focus and defined as:

$$\Delta\Phi_0(t) = k\gamma I_0 L_{eff} \tag{4.57}$$

where L_{eff} is the effective length of the sample given by:

$$L_{eff} = \frac{1 - e^{\alpha_0 L}}{\alpha_0} \tag{4.58}$$

with α_0 the linear absorption coefficient and L the sample length.

The equation 4.57 is specially importance because $\Delta\Phi_0$ is a parameter that can be easily obtained from a characteristic curve of Z-scan in the configuration Z-scan CA and from it can be found the value of γ, *i.e.,* the nonlinear refractive index of the medium.

Now, the complex electric field exiting the sample E_e now contains the nonlinear phase distortion:

$$E_e(r, z, t) = E(z, r, t)e^{-\alpha L/2}e^{i\Delta\phi(z,r,t)} \tag{4.59}$$

where through a Taylor series expansion of the nonlinear phase term $e^{i\Delta\phi(z,r,t)}$ the equation 4.59 becomes [78]:

$$e^{i\Delta\phi(z,r,t)} = \sum_{m=0}^{\infty} \frac{[i\Delta\phi_0(z,t)]^m}{m!} e^{-2mr^2/\omega^2(z)} \tag{4.60}$$

In this approach each Gaussian beam is propagated individually to the aperture plane where they are resummed to reconstruct the beam. The resultant field pattern at the aperture (E_a) taking the initial beam curvature for the focused beam into account, can be expressed as [78]:

$$E_a(r, t) = E(z, r = 0, t)e^{-\alpha L/2} \sum_{m=0}^{\infty} \frac{[i\Delta\phi_0(z,t)]^m}{m!} \frac{\omega_{m0}}{\omega_m} \exp\left(-\frac{r^2}{\omega_m^2} - \frac{ikr^2}{2R_m} + i\theta_m\right) \tag{4.61}$$

defining d as the propagation distance in free espace from the sample to the aperture plane

and $g = 1 + d/R(z)$, the remaining parameters in the equation 4.61 are:

$$\begin{aligned} \omega_{m0}^2 &= \frac{\omega^2(z)}{2m+1} \\ d_m &= \frac{k\omega_{m0}^2}{2} \\ \omega_m^2 &= \omega_{m0}^2 \left(g^2 + \frac{d^2}{d_m^2} \right) \\ R_m &= d \left(1 - \frac{g}{g^2 + d^2/d_m^2} \right)^{-1} \\ \theta_m &= \tan^{-1} \left(\frac{d/dm}{g} \right) \end{aligned} \tag{4.62}$$

The transmitted power $P_T(\Delta\Phi_0)$ through the aperture is obtained by spatially integrating the equation 4.61 up to the aperture radius r_a, which yields:

$$P_T(\Delta\Phi_0) = c\epsilon_0 n_0 \pi \int_0^{r_a} \mid E_{a(r,t)} \mid^2 r dr \tag{4.63}$$

Including the temporal variation of the pulse, the normalized Z-scan transmittance can be calculated as [78]:

$$T(z) = \frac{\int_{-\infty}^{\infty} P_T(\Delta\Phi_0) dt}{S \int_{-\infty}^{\infty} P_i(t) dt} \tag{4.64}$$

where $P_i(t) = \pi\omega_0^2 I_0(t)/2$ is the instantaneous input power (within the sample), $S = 1 - e^{\frac{-2r_a}{\omega_a}}$ is the linear transmittance through the aperture and ω_a is the beam radius of the beam at the aperture.

It is important to note that for a given $\Delta\Phi_0$, the magnitude and shape of $T(z)$ does not depend on the geometry or the wavelength as the far-field condition for the aperture plane $d >> z_0$ is satisfied. An important parameter in Z-scan technique is the aperture size S, since a large aperture reduces the variations in $T(z)$. For a very large or no aperture ($S = 1$), these variations disappear altogether and $T(z) = 1$, regardless of the z-position [78].

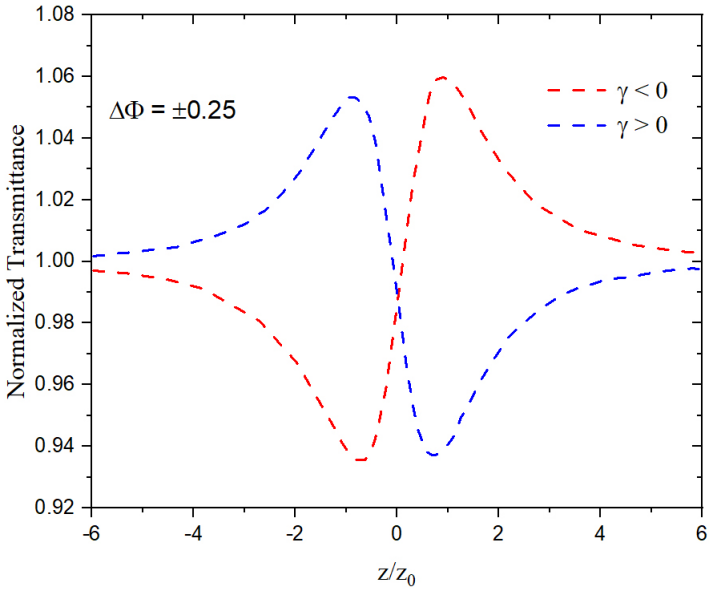

Figure 4.15: Transmittance through a sample with a positive or negative nonlinear refractive index (γ) [78].

A typical Z-scan profile for a thin sample with purely refractive, that is, without nonlinear absorption is shown in figure 4.15. The nonlinearity can be evaluated from the difference between the normalized peak and valley transmittance, ΔT_{p-v}. For a thin optical Kerr medium, ΔT_{p-v} is proportional to the nonlinear phase shift $\Delta\Phi_0$ with an accuracy of $\pm 2\%$, given by:

$$\Delta T_{p-v} = 0.406(1-S)^{0.25} \mid \Delta\Phi_0 \mid \quad \text{for} \quad \mid \Delta\Phi_0 \mid \leq \pi \tag{4.65}$$

4.7.2. Nonlinear absorption

For Z-scan measurements of nonlinear absorption, the aperture is usually removed so that the total beam power or energy can be collected and making the scan insensitive to nonlinear refraction. When there are effects of nonlinear absorption such as the saturation of absorption or absorption of two photons, the profile for a thin nonlinear medium undergoes

a change, in the case of the saturation of absorption the valley is suppressed and the peak is accentuated, while in the case of absorption of two photons it is the other way around. The effects of the nonlinear absorption can be obtained by the OA Z-scan configuration, thus, for the case of null nonlinear refraction the transmittance versus sample position graph should be symmetric around the focus since the intensity distribution of a Gaussian beam is symmetric around the focus, which presents a maximum for the case of the saturable absorption (SA) as shown in Figure 4.16.

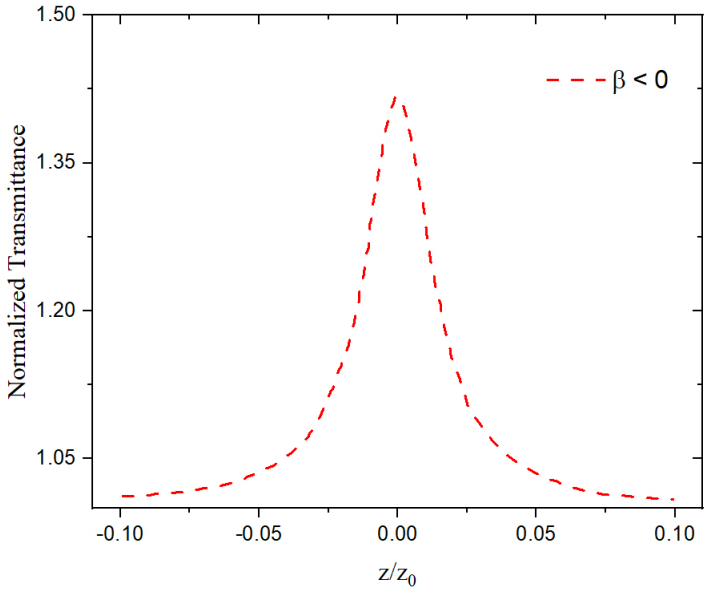

Figure 4.16: Open-aperture Z-scan curves for SA.

The nonlinear absorption coefficient, β, can be determined from a theoretical adjustment of the curves obtained from the characteristic curves of OA Z-scan configuration, this adjustment is given by [78]:

$$T(z, S = 1) = \sum_{m=0}^{\infty} \frac{[-q_0(z, 0)]^m}{(m + 1)(3/2)} \tag{4.66}$$

which can be used as long as the following condition is met:

$$\mid q_0 \mid = \mid \frac{\beta I_0 L_{eff}}{1 + (z/z_0)^2} \mid < 1 \tag{4.67}$$

where I_0, Z_0, and L_{eff} are experimental parameters and can therefore be fixed in the fitting procedure.

In the case when the samples present a strong nonlinear behavior, the CA Z-scan curves obtained directly from experiment did not feature the common valley-peak (peak-valley) pattern in transmittance since the nonlinear absorption tends to dominate over nonlinear refraction. Therefore, in order to determine NLR responses with the presence of a nonlinear absorption response, the protocol proposed by Sheik*et al.,* is followed, that is, nonlinear absorption contribution is subtracted from the CA transmittance by a simple division of curves CA/OA. In the same reference it is stated that such a procedure can be done only if the following conditions hold [78]: 1) $q_0(0,0) \leq 1$ and 2) $\beta\lambda/4\pi\gamma$.

On the other hand, if the nonlinear refraction appears in its "pure" form, then, Z-scan CA curves are well fitted by means of the equation (also given in [78]):

$$T(z, \Delta\Phi_0) = 1 - \frac{4\Phi_0(z/z_0)}{[(z/z_0)^2 + 9]\,[(z/z_0)^2 + 1]}. \tag{4.68}$$

4.7.3. Experimental setup of Z-scan technique

In this thesis Z-scan technique with variable polarization has been used to study the third-order nonlinear optical response of the samples. They were scanned along the optical axis (z direction) as shown in the figure 4.17. As light source, a 26 ps Nd:YAG pulsed-laser by EKSPLA was used at 532 nm with a 10 Hz repetition rate. First, a beam splitter was used to separate the laser beam into reference (detector 1) and signal ones. A second positive

lens was used to collimate the beam, then, the transmitted collimated beam was separated by a second beam splitter to direct the transmitted signal to a detector without aperture, in order to measure the nonlinear optical absorption (detector 2), and to a detector with a finite aperture, in order to measure the nonlinear optical refraction (detector 3). The signal beams were measured with Thorlabs DET10A fast photo-diodes. Irradiance and polarization of the incident light were controlled by using two half-wave plates and a linear polarizer.

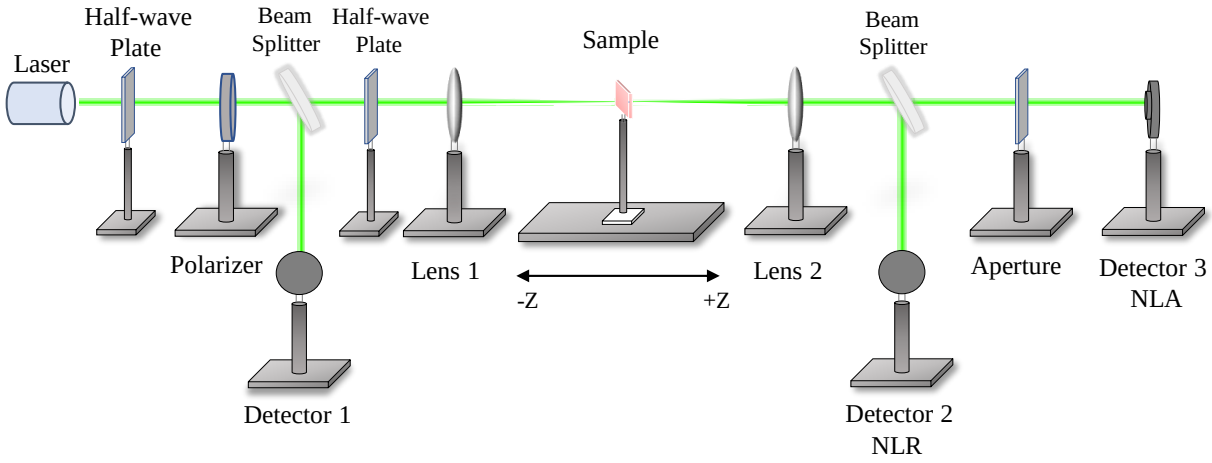

Figure 4.17: Schematic diagram of the Z-scan technique.

Carbone disulfide (CS_2) is a standard reference material in Z-scan measurements [78,79]. This material presents optical-Kerr effect since it has negligible nonlinear absorption. In this work, Z-scan setup was calibrated using 1 mm thickness of high purity CS_2 solution. The valley followed by a peak of the NLR measurement turns out to be evidence of a positive nonlinear refraction index (γ) for $\lambda = 532$ nm as shown in figure 4.18, where the continuous line correspond to the theoretical fitting by use of equation 4.68. Experimental data from NLA measurement showed no evidence of nonlinear absorption, as expected.

Thus, a $\Delta T_{p-v} = 0.186$ with a central peak incident irradiance $I_0 = 1.39$ GW/cm^2 was found, then, from equation 4.65, it follows that $\Delta\Phi_0 = 0.461$ and $\Delta n_0 = 3.93 \times 10^{-3}$. Therefore, taking into account that $\Delta n_0 = \gamma I_0$, the nonlinear refraction is $\gamma = 2.83 \pm 0.07 \times 10^{-18}$ m^2/W. This value agrees to those determined by earlier reports [39, 78, 80].

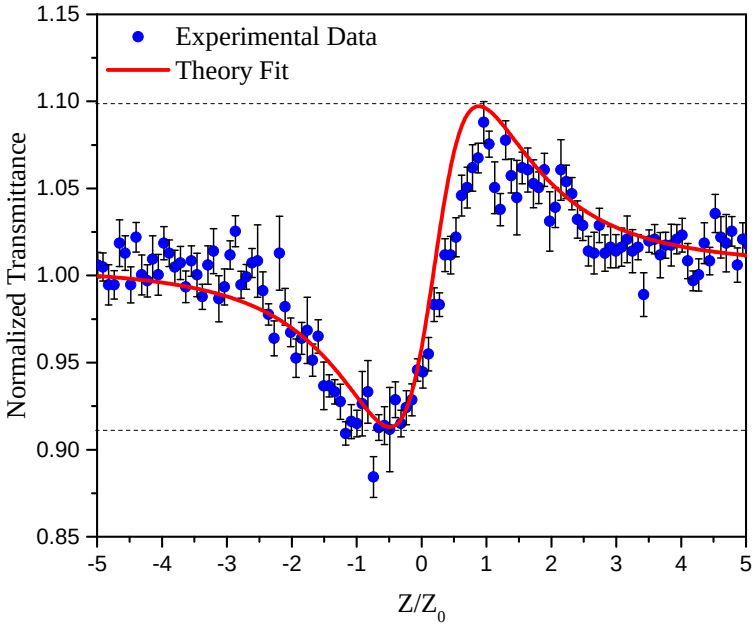

Figure 4.18: Z-scan normalized transmittance for 1 mm cell of CS_2 at 532 nm.

CHAPTER FIVE

Results and Discussion

This chapter is mainly divided into 2 sections. The first one discusses the results obtained in the production of silica particles from LIT-synthesis (see Chapter four), particles that will later serve as lithographic masks in the manufacture of gold nanocomposites embedded in SiO_2 matrix through the implantation of high-energy gold ions. In the second section, the results of the third-order non-linear optical response of these nanocomposites are studied, in particular, the non-linear absorption response as a function of the polarization angle of the incident light is investigated.

5.1. LIT-synthesis as another method to get silica particles

As mentioned earlier, NSL requires high-quality spheres to have better results when using this technique. In this way, this section presents the results of the preparation of colloidal silica particles by means of LIT-synthesis described in the Chapter 4.

Colloidal silica particles in the 600 - 1000 nm size range were prepared. The TEOS, H_2O, NH_4OH and EtOH volumes were 1.8 ml, 8 ml, 5.5 ml and 20.0 ml, respectively. The initial temperatures of the reagent solutions, as well as the laboratory room temperature conditions (with 21% humidity), are summarized in Table 1 for each type of sample.

Table 5.1: Experimental parameters used for the preparation, according to our LIT-synthesis method, of the different series of silica particles. The average particle diameter and the standard deviation (SD) determined by SEM measurements are also included.

Batch Number	Room Temperature (°C)	Initial Reagent Temperature (°C)	ΔT (°C)	Average Diameter (nm)	(SD) (nm)
a	17.0	12.0	5	590	(18)
b	18.0	6.0	12	650	(19)
c	18.0	8.0	10	660	(26)
d	18.0	10.0	8	680	(14)
e	18.0	12.0	6	600	(15)
f	18.0	14.0	4	610	(11)
g	19.0	12.3	6.7	870	(33)
h	20.5	12.0	8.7	1000	(24)

It can be clearly noticed from figure 5.1 that the silica particles are uniformly spherical and well-shaped over the entire size range. The diameter size and the standard deviation (SD) were determined from the SEM micrographs using the image processing software ImageJ [81]. From 5 or 6 images (x5000 magnification) no less than 5000 particles were measured for each sample. The SEM results are also included in Table 1, indicating that the average particle diameter is in the 600 - 700 nm range (batches b - f, fixed RT = 18°C), with a narrow standard deviation as low as 11 nm (for batch f) that represents only 1.8% of the average particle size value. It is important to highlight that under these conditions the exponential equation proposed by Gao *et al.*, to predict the particle size is valid for the experimental results obtained with LIT-synthesis [51]. Indeed, Gao *et al.*, found that in the 40 - 120 ml volume range, the smaller the ethanol volume the larger the particle size (in the

75 - 400 nm range). If we extrapolate the proposed equation to the amount of EtOH used in our LIT-synthesis reaction, $V_{EtOH} = 20$ ml, it follows that the equation leads to a particle diameter of the order of 600 nm: $D = 885.45 \exp[-0.02(V_{EtOH})] = 593.5$ nm. This value can be fairly compared with the average diameters obtained from batches a - f (see Table 5.1). On the other hand, if we increase the RT up to 20.5°C (with the initial reagent temperature around 12°C), it is possible to obtain even larger silica particles, 1 μm in diameter with a standard deviation of 24 nm (for batch h) which represent only 2.4% of the average particle size value.

For comparison purposes, Figure 5.1 show representative SEM images of batches e and h, taken at different image magnifications and using the same scale bar, together with their corresponding particle size distributions. One can observe that the monodisperse silica particles form well-defined two-dimensional hexagonal arrays with a regular interparticle distance. In general, domain boundaries and point defects are responsible for introducing disturbance in the monolayer structure. However, in the samples point defects and dislocations were hardly observed in domain areas as large as several hundreds of μm^2. Moreover, no aggregation of particles took place. Therefore, this method offers an alternative to getting essentially monodisperse spherical colloidal silica particles with diameters ranging from 600 nm to 1000 nm with a lower size distribution compared to literature [82–84], guaranteeing the formation of high-quality hexagonally-ordered monolayers.

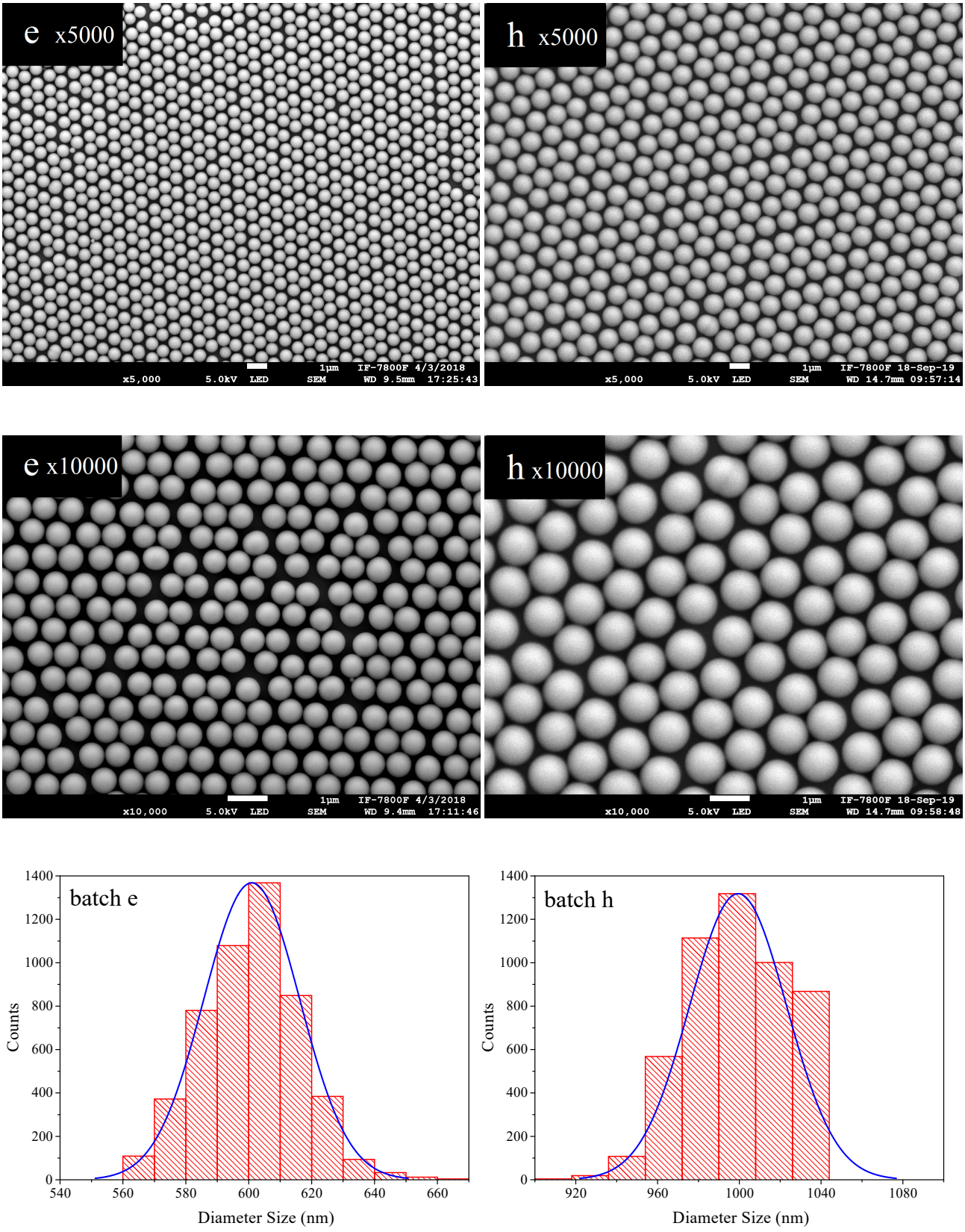

Figure 5.1: SEM images of micro-spheres prepared using LIT-synthesis at different magnifications: (x5000 and x10000) and the normal size distribution for batch e (left column) and for the batch h (right column). The scale bar correspond to 1 μm for all the cases.

5.1.1. Hydrolysis and condensation stages

Some authors suggest that even if initially a broad size distribution of primary particles could appear in the synthesis solution (hydrolysis stage), the ensuing kinetics (condensation stage) is such that it is dominated by the preferential growth of large particles at the expense of smaller ones (Ostwald ripening model), assuring a narrow size distribution of the particles at later stages [21]. Thus, the particles are spherical because they start with nucleation and they slowly grow to larger and larger. In our case we can consider that with the decrease of the reaction temperature the TEOS hydrolysis rate obviously decreases. Then it is plausible that the longer the delay before the beginning of the condensation stage, the greater the possibility of growing uniform and spherically well-shaped colloidal silica particles. Therefore, a slower reaction will result in lower polydispersity if allowed to react longer. In general, colloidal systems have interfaces and in order to minimize the interfacial energy of the system, the formation of spheres, which have the smallest surface area for a given particle size, can be promoted. However, it is also well known that the dimensionality and ultimate particle shape depend on different factors (such as reaction temperature, precursors, solvents and catalysts) that must be optimized, especially because the system and the processes are far from thermodynamic equilibrium [85]. Moreover, increasing the hydrolysis and condensation time intervals results in homogeneous and larger particle sizes. The rate of particle growth is limited by hydrolysis, but the amount of hydrolyzed TEOS available per particle is larger, leading to the formation of smooth and large spherical silica particles with a quite high monodispersity [86].

5.1.2. Relationship with temperature

During the silica synthesis the reaction temperature behavior was measured every minute after the first drop of solution (2) (ammonium hydroxide/distilled water) into solution (1) (TEOS/EtOH). From Figure 5.2 we can notice that all the synthesis reactions prepared at fixed room temperature (RT $= 18°C$), with different values for the initial temperature of the reagent mixture T_{mix} (from 6°C to 14°C), exhibit a sharp temperature increase, with a noticeable peak maximum at around 10 minutes. Part of this behavior can be easily explained as a simple heat transfer by the surrounding atmosphere (RT fixed at 18°C) to the mixture of the two solutions (with T < RT), and therefore the reaction mixture warms up and reaches a higher temperature. On the other hand, the peak maximum of the reaction temperature can be directly associated with the exothermic character of the nucleation process, generally starting within 10 min after the beginning of the mixture procedure. The initial phase of the condensation mechanism is clearly noticeable by an increasing opalescence of the mixture after 5 - 7 min, leading to a final turbid white suspension within a few more minutes. Moreover, for our series of samples, the peak maximum depends on the initial temperature of the reagent mixture T_{mix}. After the peak maximum, the monitored temperature decreases to a value of approximately 15°C at around 40 min for all the samples (Fig. 5.2). In all the cases, it is important to notice that the final temperature reached by the synthesis mixture stabilizes at a value T = 15°C < RT = 18°C, at least in the 40 - 120 min time interval. In this case, this constant temperature seems to be imposed by the surrounding ambient at fixed RT. Once again, we can notice that the negative slope associated with the temperature decrease in the 10 - 30 min range also depends on the initial T_{mix} value. Therefore, the higher the initial T_{mix} value for the reagents the higher the reaction temperature peak, and the absorbed energy contributes to the overall internal energy of the solution mixture.

A similar temperature behavior as a function of the reaction time was observed in the case of the samples prepared at four different room temperatures (fixed RT ranging from

17°C to 20.5°C) for an initial reagent temperature of T_{mix} = 12°C. Again, a noticeable peak maximum can be observed after 10 min (see Fig. 5.3), and it seems to slightly depend on the surrounding RT. After the peak maximum, the monitored temperature decreases and it almost stabilizes into the 15 - 16°C range, with no clear dependence on the ambient RT. In all the cases, the final temperature reached by the synthesis mixture always stabilizes at a temperature T lower than the fixed RT, at least in the 40 - 120 min time interval.

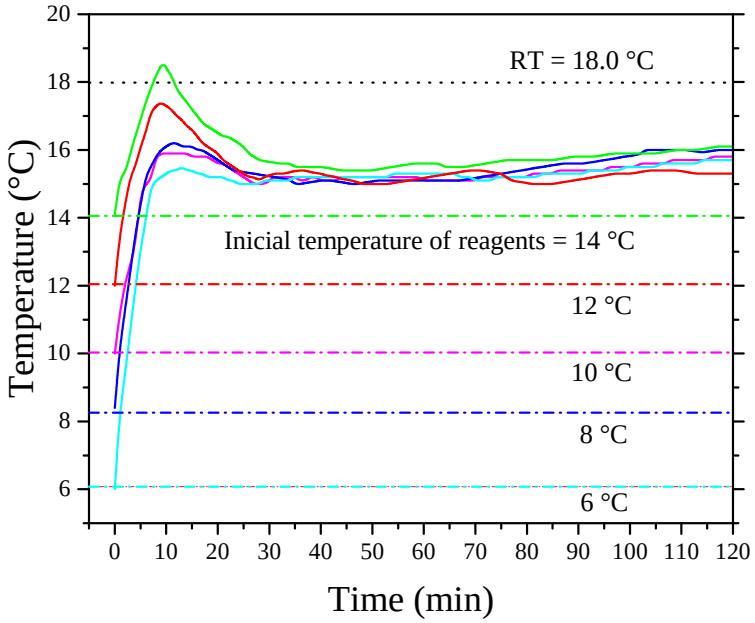

Figure 5.2: Reaction temperature behavior as a function of time during the silica particle synthesis: Fixing room temperature at 18°C and varying the initial T_{mix} temperature of the reagents from 6°C to 14°C.

The next experiment allows us to assess the effect of the exothermic character of the nucleation process on the reaction temperature during the LIT-synthesis method as compared with the heat transfer process by the surroundings to the solution. Then, in Figure 5.4, the red curve shows the temperature behavior of the solution (1) (TEOS/EtOH) after the heat exchanger was set apart, but without the addition of solution (2), for an initial reagent temperature of T_{mix} = 12°C. One can notice that within 30 min the temperature of solution (1) increases steadily up to the ambient room temperature fixed at 18°C. In this case we

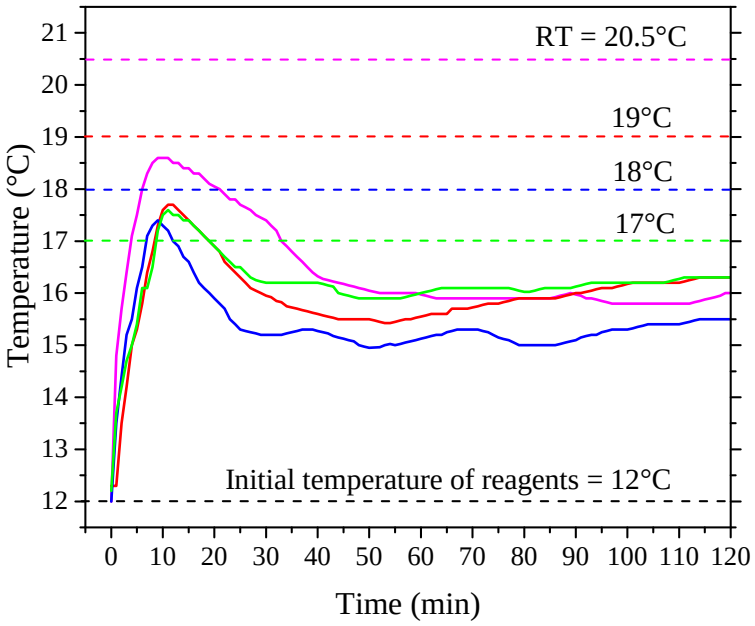

Figure 5.3: Fixing initial reagent temperature at 12° and varying the room temperature from 17°C to 20.5°C.

can consider indeed that this temperature behavior corresponds to the energy transferred by the surroundings to the solution (1). On the other hand, for comparison purposes, the blue curve shows the reaction temperature behavior of the sample prepared following the LIT-synthesis method (batch e: T_{mix} = 12°C and RT = 18°C), previously included in figure 5.2. This comparison confirms that the temperature behavior during the LIT-synthesis can be associated with the exothermic character of the nucleation-condensation phase of the silica particle formation. In this case, a sharp temperature increase takes place for the reaction mixture, with a noticeable peak maximum at around 10 minutes. As discussed above, it is generally observed that the condensation reaction starts within 7 min and it is linked to the increasing opalescence of the mixture suspension [5]. After the peak maximum the reaction temperature decreases at about 15° within 30 min, and this behavior can be related to the fact that during the growth process the production of hydrolyzed TEOS monomers is rate-limiting [86, 87]. Thus, as the TEOS concentration slowly decreases a steady-state concentration of hydrolyzed species follows until at the end of the growth.

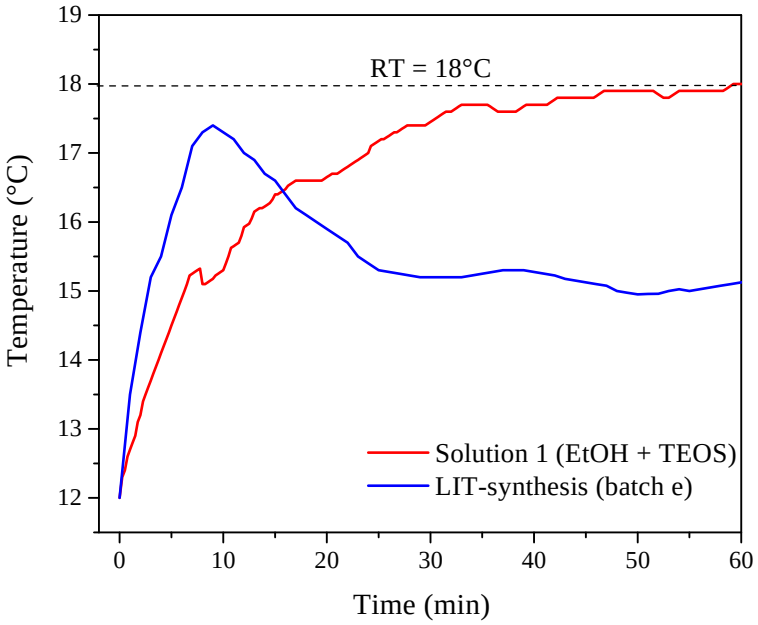

Figure 5.4: Comparative of the temperature behavior as a function of time (at RT = 18°C) of solution (1) at an initial reagent temperature of T_{mix} = 12°C, after the heat exchanger was set apart, but without adding solution (2) (red curve), and the sample prepared following the LIT-synthesis method (batch e: T_{mix} = 12°C and RT = 18°C) (blue curve).

Also, from table 5.1 we can notice that the growth in diameter size for particles prepared by LIT-synthesis with an initial reagent temperature of T_{mix} = 12°C (batches: a, e, g and h) at different room temperatures depends directly on the fixed laboratory RT, as shown in figure 5.5. Indeed, as a function of RT the particle diameter increases from small sizes (589 nm) at 17°C, and subsequently there is an accelerated growth up to a maximum value of D = 1μm for RT = 20.5°C. A sigmoid exponential function can be used to fit our experimental data, leading to the following expression:

$$D = 589 + \frac{411}{1 + 10^{(18.72-RT)1.43}} \tag{5.69}$$

where D is the silica particle diameter in nm, RT is the room temperature in °C, and the parameter p = 1.43 is the mean slope (Hill slope, unitless) used in this case for the data

fitting. The Hill slope describes the steepness of the curve and if it is positive, the curve increases as the laboratory RT is increased. Clearly, this behavior opens the possibility of tuning the size particle as a function of the laboratory temperature for a given initial reagent temperature T_{mix}.

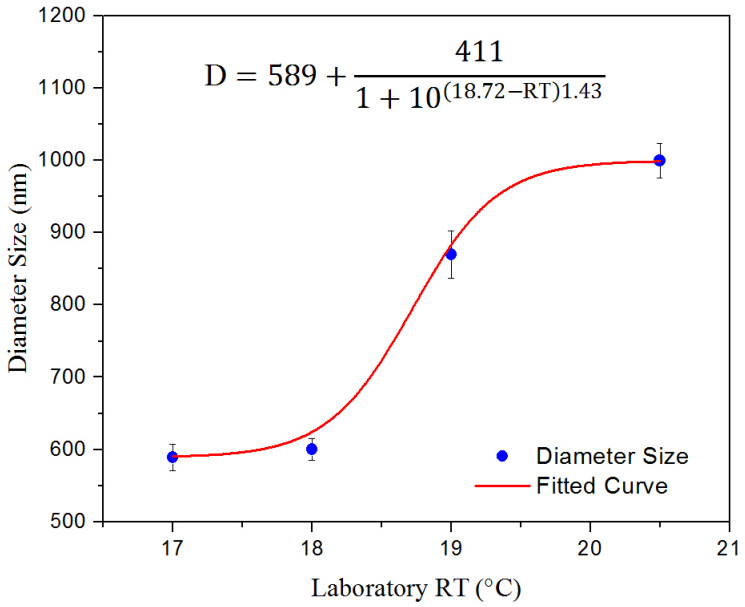

Figure 5.5: Particle size as a function of the fixed laboratory RT for the colloidal silica particles prepared by LIT-synthesis with an initial reagent temperature of T_{mix} = 12°C (batches: a, e, g, h), together with the sigmoid exponential fitting curve.

5.1.3. Monolayer formation with Spin-coating deposition

With the new proposed deposition technique, *i.e.*, the standard spin coating method but adding the sample-closed box (see Chapter 4), it is possible to greatly improve the monolayer quality of our samples. Indeed, it is clear from the SEM images that the silica monolayers possess orientational order over macroscopic distances larger than hundreds of μm (see Fig. 5.6). These ordered arrays of silica particles onto Si and silica substrates can be extended over larger areas due to the high monodispersity of the silica particles prepared using our LIT-synthesis method, and also because during the spin coating process most of the smaller particles are ejected from the substrate. In addition, since the sample is isolated from the external environment, the evaporation process takes place gradually inside the box, generating its own atmosphere, which favors the self-assembly of hexagonally-ordered close-packed particles into monolayers ideal for NSL and further applications. On the other hand, it is clear that the gradual control of the evaporation rate during the spin coating deposition inside the sample closed box improves the silica monolayer quality.

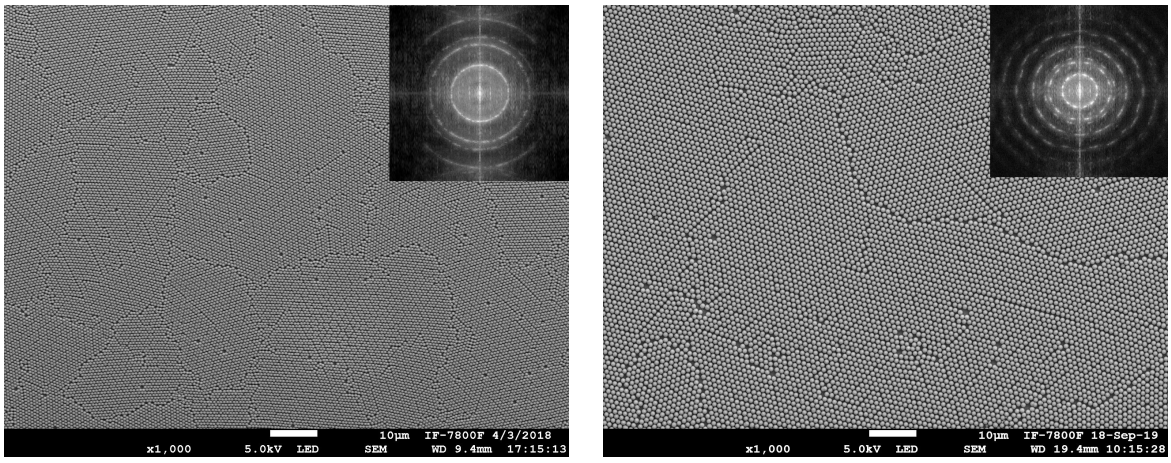

Figure 5.6: SEM images of extended ordered silica particle arrays onto Si substrates, with a magnification as low as 1000x, and their corresponding Fast Fourier Transform (FFT) for silica particle diameters of: a) 600 nm and b) 1000 nm.

In order to characterize the long-range order of the silica monolayers the corresponding SEM images were analyzed by means of a Fast Fourier Transform (FFT) study. The FFT images were obtained from an area of about 100 μm^2. Two representative SEM images were studied, revealing substantial differences in the FFT patterns for samples with different silica particle sizes. For the particles with a 600 nm diameter, the FFT images show well-defined intensity rings (inset Fig. 5.6.a). In this case, a uniform distribution of intensity along the rings could correspond to a complete disorientation of separate regions or domains contributing to the FFT pattern. In contrast, in the case of particles with a 1000 nm diameter, wide maxima instead of rings are clearly observed for the FFT image (inset Fig. 5.6.b). This indicates that during the spin coating deposition orientational order is built over distances larger than the image size. Therefore, the FFT studies confirm the long-range order of our monolayered samples, formed by monodisperse colloidal silica particles with large diameters, over macroscopic distances of the order of millimeters. The self-assembly of a surface into regular hexagonal structures can be currently observed not only in physical systems, but also in other sciences such as biology, chemistry or geology. It can be described as a universal phenomenon in which the involved interface forces tend to minimize the potential energy of a free surface.

5.2. Au NP arrays embedded in a SiO_2 plates

The silica particle masks were also deposited on high-purity fused silica plates ($5 \times 5 \times 1$ mm). Experimentally, masks formed by 590 nm and 650 nm silica particles onto fused silica substrates were then implanted at room temperature with 2 MeV Au ions, fluences of 1×10^{16} and 5×10^{16} ion/cm^2, perpendicularly to the sample surface. Thus, resulting in four different samples, which individual parameters are given in Table 5.2.

Table 5.2: Experimental parameters associated with the 2 MeV Au^+ ion implantation into two different masks prepared by NSL. The average particle diameter and the standard deviation (SD) determined by SEM measurements are included. The Au projected range in silica calculated by the SRIM-2013 code and the Au ion range determined experimentally by Rutherford Backscattering Spectrometry (RBS) are also included.

AuNps:SiO_2	Mask sizes (SD) (nm)	Fluence (ion/cm^2)	SRIM 2013 (nm)	RBS (SD) (nm)
1a	590 (18)	1×10^{16}	500 (9)	518 (28)
1b	590 (18)	5×10^{16}	500 (9)	521 (20)
2a	650 (19)	1×10^{16}	500 (9)	519 (17)
2b	650 (19)	5×10^{16}	500 (9)	520 (22)

According to the SRIM-2013 simulation, the projected range of 2 MeV Au ions in SiO_2 is about 500 nm [74]. These values indicate that most of the impinging Au ions are completely stopped into the silica particles, while the ions passing through the interstitial regions of the mask are deep implanted into the silica substrate. Moreover, after the ion implantation, the spherical silica particles turned into ellipsoidal particles, as a result of an increase of the particle dimensions perpendicular to the ion beam and a decrease in the direction parallel to the ion beam. This ion hammering effect induced the modification of the shape of the original spherical colloids into ellipsoidal oblates [88].

In figure 5.7 shows representative SEM images of the 590 nm silica particle array after the Au ion implantation at two different fluences: 1×10^{16} and 5×10^{16} ion/cm^2. It can be observed that this ion-induced particle shape modification leads to an increase of the major axis of the ellipsoidal particle as a function of the irradiation fluence. It is important to notice that the low fluence (1×10^{16} ion/cm^2) seems to be enough to practically close

the interstices between the silica particles. With the 5×10^{16} ion/cm^2 fluence, the silica deformation is even higher, but always maintaining the hexagonal ordered array. By this way, the mask openings of the silica particle monolayer can be modified as a function of the irradiation parameters [89], while allowing the implanted ions to pass through the interstitial regions of the mask and reach depths corresponding to the nominal Au ion projected range into the silica substrate.

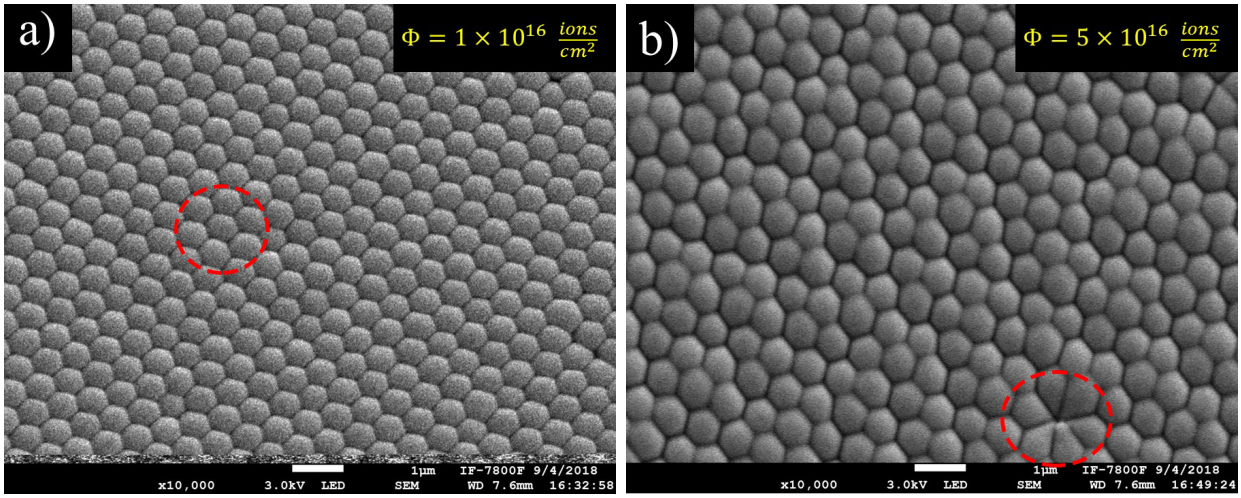

Figure 5.7: Representative SEM images of 590 nm colloidal silica particles deposited onto fused silica substrates and implanted with 2 MeV Au ions at two different fluences: a) 1×10^{16} ion/cm^2; b) 5×10^{16} ion/cm^2. Notice the ion-induced shape deformation of the silica particles.

After the ion implantation, the lithographic mask must be removed without affecting the surface of the substrate. For this case, the usual methods such as ultrasonic agitation [90] and mechanical removal [14] were unsuccessful because, after the high-energy implantation, the masks were strongly anchored to the substrate. Instead, the samples were subjected to a polishing method to eliminate the silica particles with a 1 µm polishing paper, the figure 5.8 shows a before and after polishing.

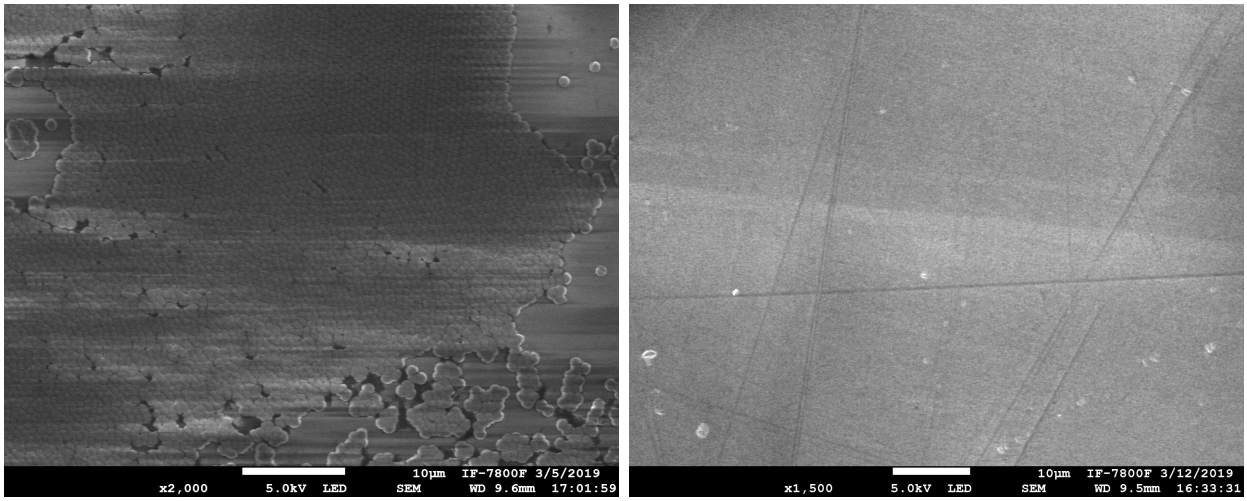

Figure 5.8: Representative SEM images of the samples (x2000 magnification): before being polished (with only ultrasonic agitation, left) and after polished (right).

Finally, in order to promote the nucleation of Au nanoparticles into the substrate, the samples were annealed at 1100°C in an oxidizing atmosphere (air) for 1 hour, the Au particle size depend directly of the implantation fluences and annealing temperature according to previous studies [19,91,92]. After annealing, all samples exhibit the characteristic red color associated with the presence of embedded gold nanoparticles, with a quite pale red tone in the case of implanted samples with the lower fluence (samples 1a and 2a, Table 5.2). Figure 5.9 shows a schematic diagram of the fabrication procedure of the Au NPs ordered arrays.

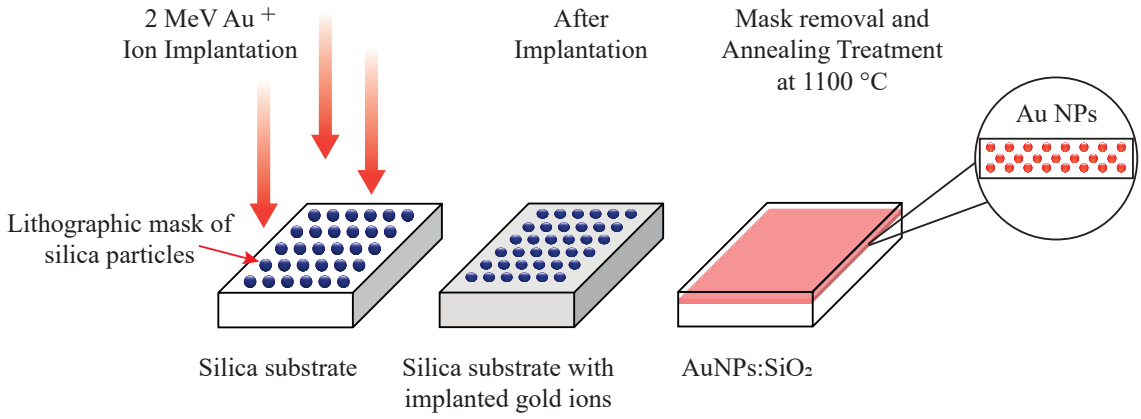

Figure 5.9: Diagram of AuNPs:SiO_2 manufacturing process.

5.2.1. Rutherford backscattering Spectrometry (RBS)

In order to determine both the Au content and the concentration depth profile of the implanted ions, ^{4}He RBS measurements were simulated using the RUMP code [93]. Figure 5.10 shows the Au concentration depth profile determined by RBS for the 650 nm silica particle masks implanted at two different fluences (1×10^{16} and 5×10^{16} ion/cm^2), together with the RUMP simulation curves calculated by assuming a Gaussian distribution. Furthermore, one can observe that the two simulated curves are fairly centered at the same position, a depth value actually corresponding to the 2 MeV Au projected range (500 nm) determined by the SRIM-2013 code. The corresponding full width at half maximum (FWHM) is $\sim$ 520 nm for the 5×10^{16} ion/cm^2 fluence and $\sim$ 660 nm for the 1×10^{16} ion/cm^2 one, and it gives a measure of the actual depth distribution of the Au nanoparticles in the implanted layer. Finally, although it is clear that the maximum concentration depends on the nominal implantation fluence, the mask size also directly affects the Au nanoparticle formation, because the mask itself limits the number of implanted ions reaching the substrate (see Fig. 5.10.b). Thus, the larger the silica particles size, the lower the amount of Au ions passing into the substrate.

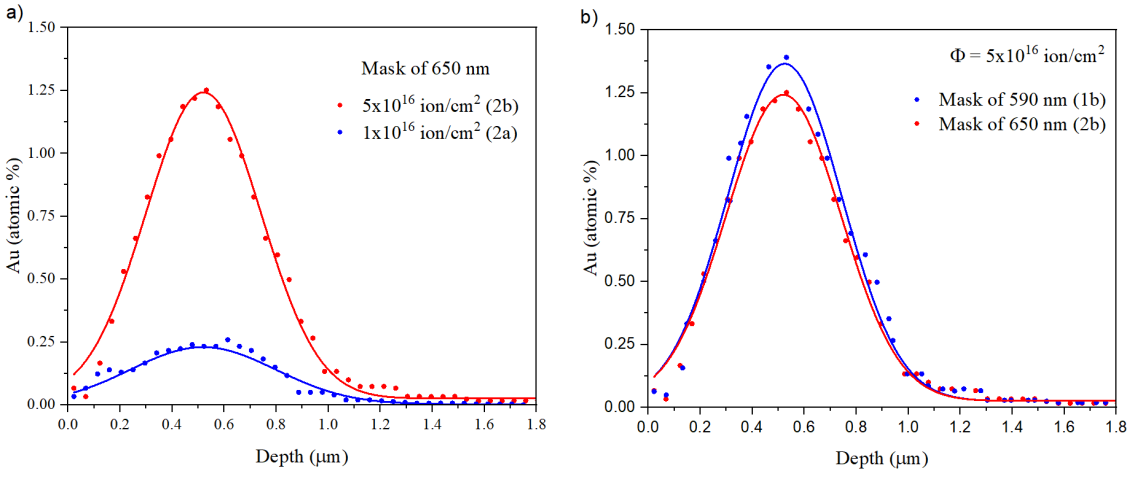

Figure 5.10: Au concentration depth profile determined by RBS. a) For the 650 nm silica particle masks implanted at two different fluences (1×10^{16} and 5×10^{16} ion/cm^2); b) For the two different NSL mask sizes (590 nm and 650 nm) implanted at the same fluence (5×10^{16} ion/cm^2). The continuous curves correspond to the best RUMP fitting to experimental data assuming Gaussian functions.

5.2.2. Optical absorption characterization

It is well known that the near-field enhancement effect based on LSPR absorption is the typical optical response of metallic NPs. Their optical extinction spectra (OES) may provide information on the kind of metallic NPs, as well as on their size and shape. After the thermal annealing, the samples implanted with the highest fluence exhibit an intense band centered at 520 nm in the extinction spectra, which can be clearly associated with the formation of spherical Au NPs embedded in the fused silica plates after thermal treatment (see Fig. 5.11). As no noticeable additional bands are observed, no other multipolar contributions to the extinction spectra are present. For the samples implanted at low fluence, the LSPR absorption band is hardly noticeable because much of the amount of gold was embedded in the mask and not in the substrate. One can also observe that the intensity of the SPR increases with the nominal implantation fluence, but it also depends on the NSL mask size, which directly affects the amount of formed Au NPs.

Through a careful analysis of the spectra and by using Mie theory, it is possible to estimate the average particle size (assuming a spherical shape). In this thesis, the NPs radius distributions were determined by fitting the experimental OES spectra using the MieLab code developed by our group [94]. The best fits were obtained assuming a normal distribution for the particle sizes, as shown in Figure 5.11 and reported in Table 5.3. The two masks implanted at 5×10^{16} ion/cm^2 are compared in Figure 5.12.a, it is clear that the shape of the optical extinction spectra depends on the mask size because there is a larger space between the particles and thus a greater amount of ions are implanted into the substrate. For completeness, the linear optical responses were also characterized as a function of the incident polarization angle. Fig. 5.12.b shows the OES as a function of the linear polarization angle for the sample 2b (650 nm mask, 5×10^{16} ion/cm^2). The electric field is rotated in 10° steps from 0° to 90° with respect to the plane of incidence. The linear optical response of the sample was found to be insensitive to the orientation of the incident electric field

and no major differences were observed in the spectra. Such a behavior is expected for samples exhibiting a high degree of symmetry such as honeycomb or hexagonal plasmonic lattices [95].

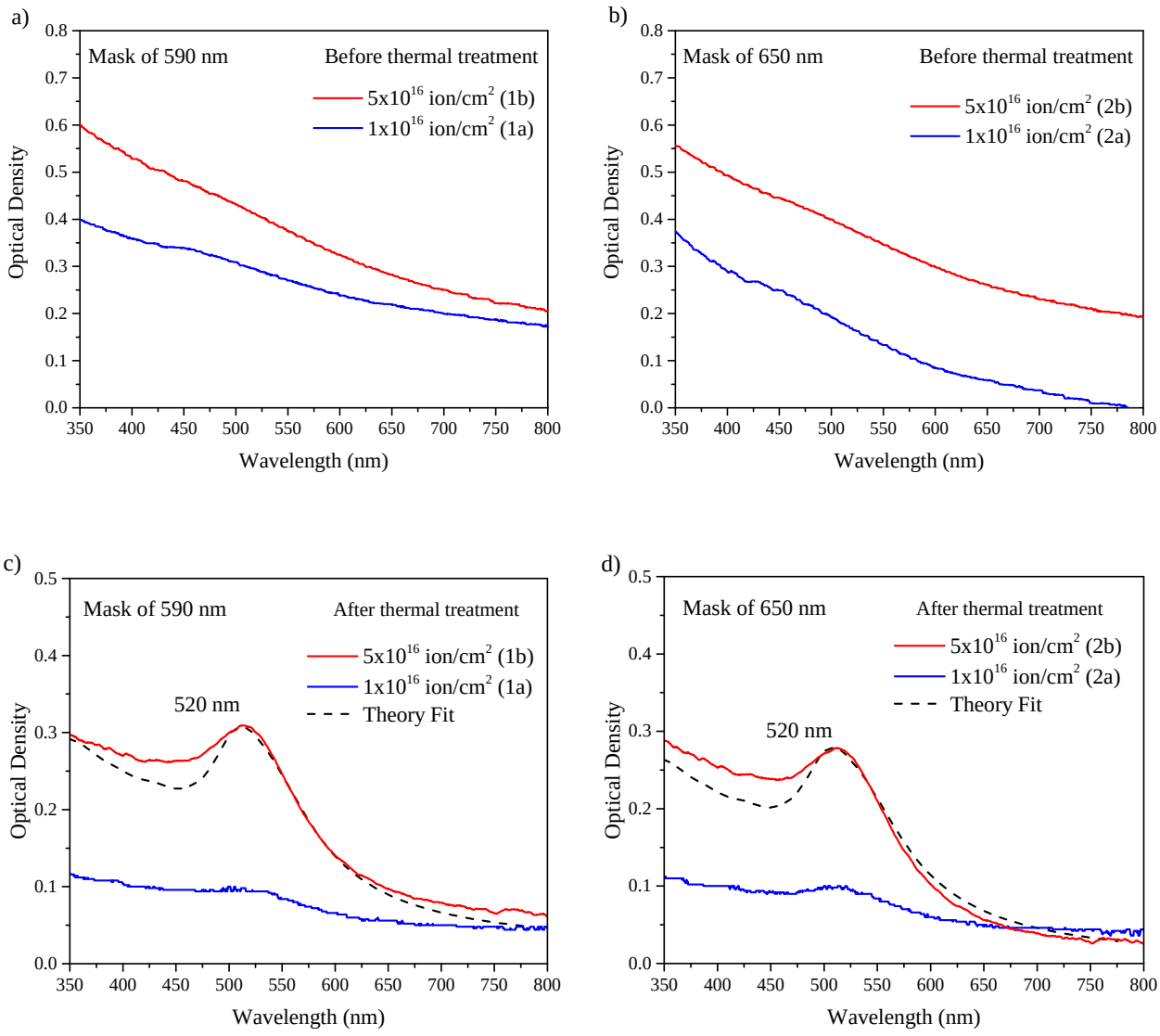

Figure 5.11: Optical extinction spectra of the ordered array of spherical Au NPs embedded in fused silica substrates prepared by ion implantation at 1×10^{16} and 5×10^{16} ion/cm^2 fluences into two different NSL mask sizes: a) 590 nm mask and b) 650 nm mask before thermal treatment, c) 590 nm mask and d) 650 nm mask after thermal treatment. The dashed lines correspond to the best fit obtained with the MieLab code [94]

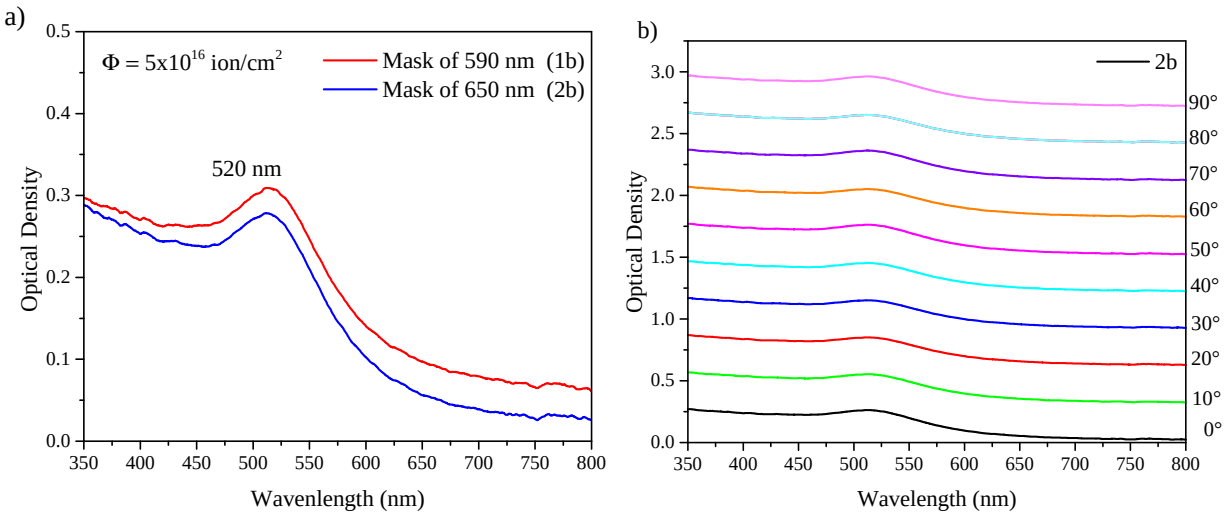

Figure 5.12: a) The two masks implanted at 5×10^{16} ion/cm^2 and b) OES as a function of the linear polarization angle for the sample 2b (650 nm, 5×10^{16} ion/cm^2). The spectra are shifted vertically by a constant amount for better readability.

Table 5.3: Average radius determined by MieLab code.

AuNPs:SiO_2	Mask size (SD) (nm)	Fluence (ion/cm^2)	Average Radius (SD) (nm)
1a	590 (18)	1×10^{16}	< 1.0
1b	590 (18)	5×10^{16}	1.1 (0.7)
2a	650 (20)	1×10^{16}	< 1.0
2b	650 (20)	5×10^{16}	1.0 (0.2)

5.2.3. Non-linear optical measurements

The nonlinear absorption (NLA) properties of the ordered arrays of Au NPs embedded in SiO_2 substrates were studied in the open-aperture (OA) configuration, where 25 transmission experimental data were taken and averaged for each step of 0.75 mm on z-axis. Since the samples implanted at low fluence (1a and 2a) showed a lower amount of Au NPs (see

Fig. 5.11), they were omitted for the z scan studies. Nevertheless, a lower limit for the implantation fluence (1×10^{16} ion/cm^2) could be established for these NSL mask sizes.

As mentioned earlier, Saturable Absorption (SA) is identified by a negative nonlinear absorption coefficient ($\beta < 0$), showing a peak in the OA transmittance scans at the lens focal point ($z = 0$). The OA Z-scan curves for the AuNPs:SiO_2 samples were measured at different peak irradiances. In particular, the figure 5.13 shows the Z-scan curves for the sample 2b (650 nm mask, 5×10^{16} ion/cm^2), with the incident polarization oriented at 0° with respect to the plane of incidence. In all cases, the continuous line corresponds to the best fit to the experimental data by using equation 4.66. The figure 5.13 shows that the NLA coefficient β increases as a function of the peak irradiance, reaching saturation values for irradiances higher than 5.5 GW/cm^2 for both samples (see Table 5.4).

Table 5.4: NLO results for AuNPs:SiO_2.

AuNps:SiO_2	1b (590 nm mask)	2b (650 nm mask)
Average Radius (nm)	1.1 ± 0.7	1.0 ± 0.2
α_0 (cm^{-1})	11999	13269
I_0 (GWcm^{-2})	$\beta \times 10^{-6}$ (cm/W)	$\beta \times 10^{-6}$ (cm/W)
1.65	-3.32	-3.43
2.64	-2.02	-2.15
4.15	-2.16	-1.81
5.48	-1.43	-1.28
6.62	-1.08	-1.21
7.95	-0.84	-1.20

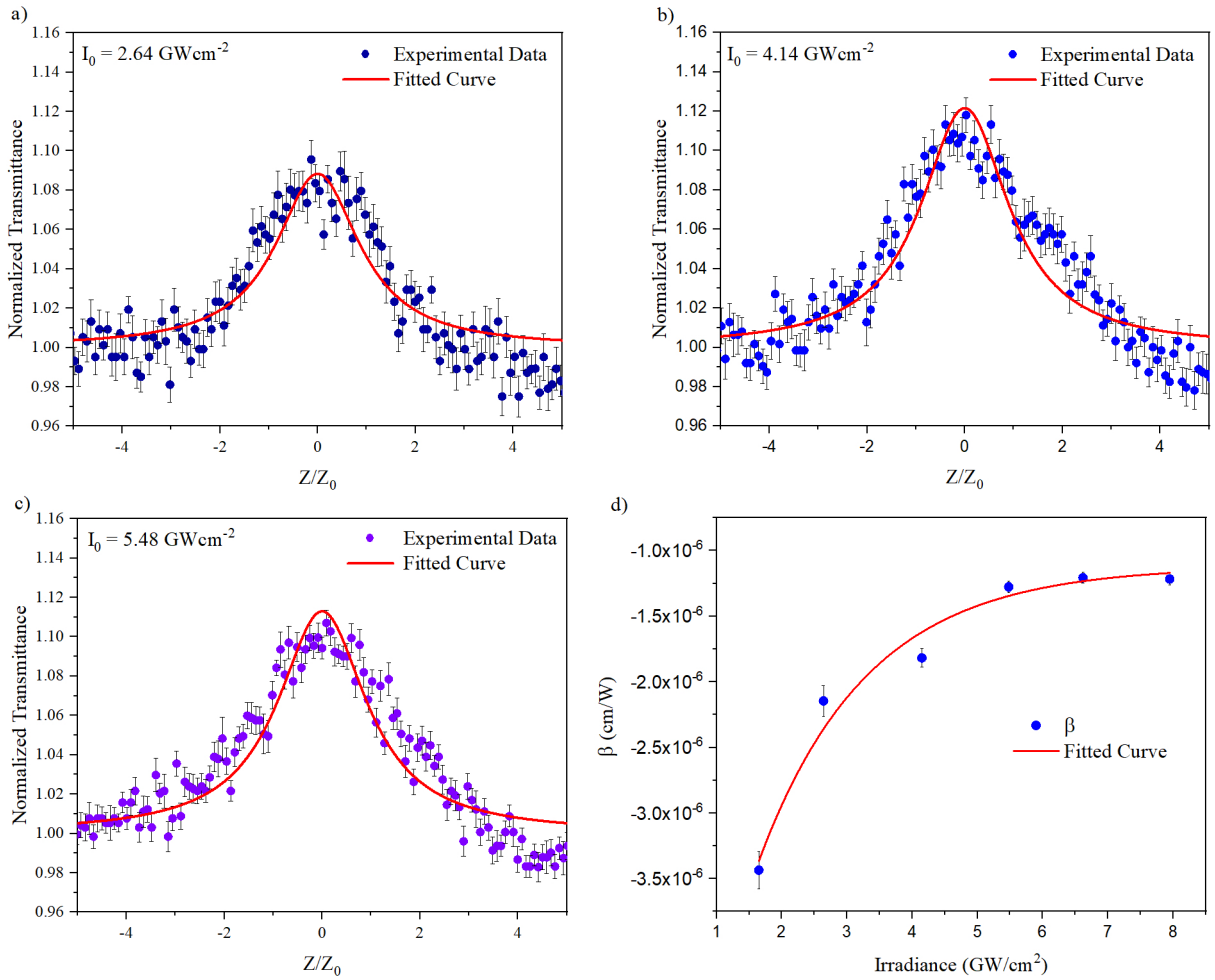

Figure 5.13: NLO response of the ordered array of spherical Au NPs embedded in SiO_2 substrates (sample 2b) for different peak irradiances: a) 2.64 GW/cm^2; b) 4.14 GW/cm^2; c) 5.48 GW/cm^2. d) Variation of the nonlinear absorption coefficient β for the sample 2b as a function of the irradiance.

In order to perform OA Z-scan measurements with different linear polarization angles, the incident electric field must be rotated by means of a half-wave plate in 10° increments with respect to the horizontal direction (0°), maintaining the sample in the same position. Figure 5.14 shows the results for samples 1b and 2b with peak irradiances of 1.65 ± 0.04 GW/cm^2 and 4.14 ± 0.05 GW/cm^2, respectively. A sinusoidal modulation of the nonlinear absorption coefficient β was observed for both samples, and this modulation can be fitted by means of the equation:

$$\beta(\theta) = \tilde{\beta} + \Delta\beta \sin\left(\frac{2\pi(\theta - \theta_c)}{\mathrm{T}}\right) \tag{5.70}$$

where $\tilde{\beta}$ is the average value of the nonlinear absorption coefficient ($\tilde{\beta} = \beta(\tilde{\theta})$), $\Delta\beta$ is the amplitude of the modulation and T is its period. Table 5.5 shows the parameters obtained from equation 5.70 for both samples. According to these results, the sinusoidal modulation of the nonlinear absorption coefficient exhibits a variation of about $\Delta\beta/\tilde{\beta} \approx 20\%$ for the sample 2b and only 7% for the sample 1b, and this is due to the fact that the peak irradiance used for 1b is very low for the saturation of the sample. However, it can be observed that the modulation period T, mainly related to the ordered array, is fairly the same for both samples, $29.7° \pm 0.34°$ and $29.88° \pm 0.20°$. These results agree with a 30° period corresponding to a honeycomb lattice, formed by the arrays of quasi-spherical Au NPs embedded in fused silica, and preferentially located in the interstitial positions determined by the hexagonally ordered NSL silica mask (see Fig. 5.15). It is important to notice that this honeycomb lattice symmetry exhibits a long-range order and holds for any coordinate system whose origin is situated at any spherical Au nanoparticle.

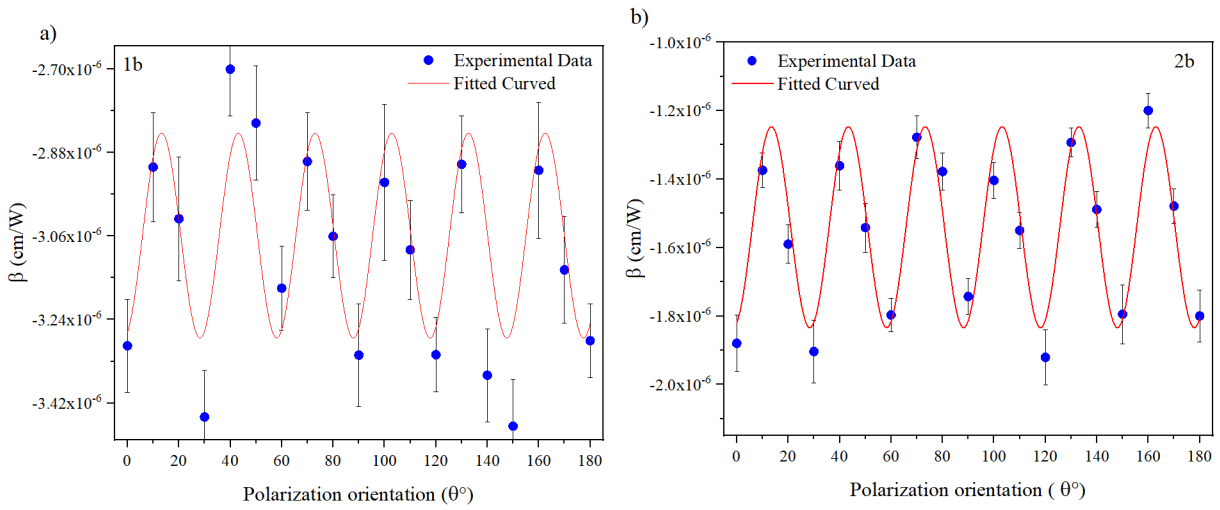

Figure 5.14: Nonlinear absorption coefficient β as a function of the linear polarization angle obtained by fitting the corresponding OA Z-scans with equation 4.66. All the measurements were performed at $\lambda = 532$ nm, with peak irradiances of: a) 1.65 GW/cm^2 for sample 1b, and b) 4.15 GW/cm^2 for sample 2b. The 30° modulation period corresponding to the honeycomb lattice can be clearly observed.

Table 5.5: Parameters determined from the sinusoidal modulation simulation for the Au NPs embedded in SiO_2 (samples 1b and 2b, 5×10^{16} ion/cm^2 fluence).

AuNps:SiO_2	1b (590 nm mask)	2b (650 nm mask)
I_0 (GWcm^{-2})	1.65 ± 0.04	4.15 ± 0.05
$\tilde{\beta} \times 10^{-16}$ (cm/W)	-3.03 ± 0.02	-1.54 ± 0.02
$\Delta\beta \times 10^{-16}$ (cm/W)	0.20 ± 0.03	0.30 ± 0.03
T(°)	29.74 ± 0.034	29.88 ± 0.20

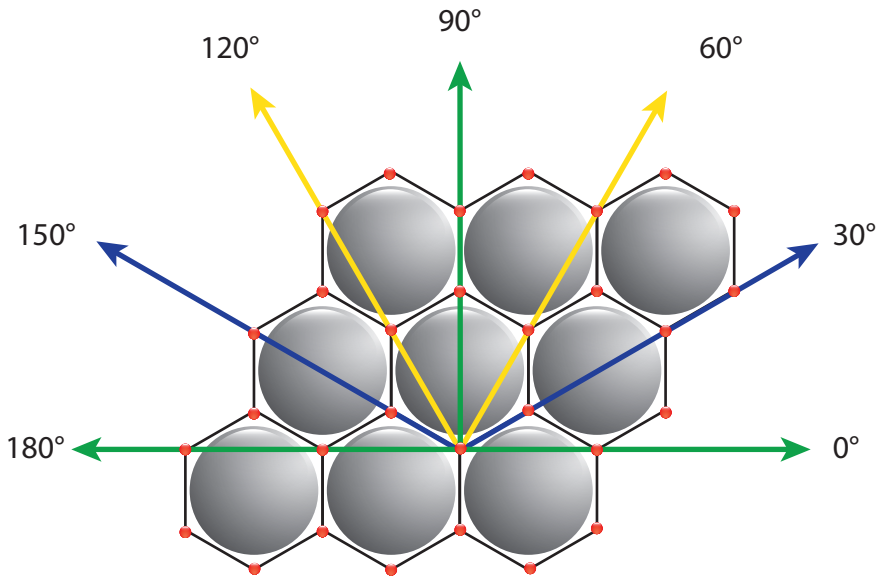

Figure 5.15: Honeycomb lattice formed by the array of Au NPs (red dots) embedded in the silica substrate and located in the interstitial positions determined by the 2-D NSL silica mask formed by a hexagonally-ordered array with a regular silica interparticle distance. The 30° modulation period corresponding to the honeycomb lattice can be clearly noticed.

This latter result demonstrates the potential of combining NSL and Ion Implantation, as it offers a solution to a recurring problem in the manufacture of such samples through other techniques. The challenge is to prevent either oxidation or sulphuration suffered by metal nanostructures when in contact with the atmosphere. That is, metal nanostructures are usually manufactured on the surface of the desired substrate, then are covered with a protective layer, but in the meantime they are exposed to the environment. In our case, as the nucleation of the NPs is generated deeply into the substrate, these arrangements are protected from any environmental factor; therefore, following this process, we are able to generate arrangements of any desired metal.

On the other hand, the properties highlighted in the present thesis make such that embedded arrays of plasmonic metallic NPs a very interesting platform for the development of all-optical nanophotonic devices with fast, strong, and tunable nonlinear optical response. As fast saturable absorbers, they could be used, for example, to develop solid-state mode-locking systems in ultra-fast laser devices. Moreover, with the dichroic effect that presents our samples, the capability to modify the nonlinear response of nanomaterials in a reversible way by switching the polarization of the light would be of great interest for NLO applications.

CHAPTER SIX

Conclusions

The presented LIT-synthesis method allows us to obtain submicrometer silica particles in the range from 600 to 1000 nm with high quality shapes and narrow size distribution just by setting the initial temperature of the reagent solutions at low values (6°C - 14°C range) and fixing the other parameters such as room temperature and concentration. Under these conditions batches of particles with diameters ranging from 600 nm to 680 nm have been produced with quite narrow particle size distribution compared to literature [82–84]. To achieve this, laboratory isothermal conditions (RT = 18°C) and a homogeneous particle suspension, maintained during the reaction by gentle agitation, proved to be effective. Additional series of samples were produced by varying the laboratory RT in the 17°C - 20.5°C range, leading to the formation of larger silica particles with increasing sizes as a function of RT. This particle growth behavior could be correctly described by using a sigmoid exponential function to fit the data, allowing the possibility of tuning the size particle as a function of the laboratory temperature.

A simple setup modification during the spin coating deposition, incorporating a sample closed box, demonstrated to improve the quality of the silica particle monolayers over silicon and silica substrates. This method favors the self-assembly of hexagonally ordered close-packed monolayers of silica particles, ideal for Nanosphere Lithography (NSL) and other applications.

The fabrication of ordered arrays of Au NPs embedded in silica substrates by a combination of NSL with high-energy MeV Au^+ ion implantation is reported for the first time to our knowledge. These spherical Au NPs exhibit a long-range order honeycomb lattice despite the transversal deformation of the lithographic silica mask.

Open aperture Z-scan measurements were performed for different linear polarization angles in order to study the dichroic properties of the thus-formed honeycomb lattice. The samples showed a strong saturable absorption with a sinusoidal modulation of the nonlinear absorption coefficient β up to about 20%, with a modulation period of 30°, clearly associated to the Au NPs honeycomb lattice symmetry.

This research confirms that the combination of lithographic silica masks and deep ion implantation can be a very useful technique to fabricate ordered arrays of embedded NPs in dielectric substrates. Therefore, the formation of ordered arrays of plasmonic metallic NPs opens the path to develop nanophotonic devices with fast, strong and tunable nonlinear optical responses.

Bibliography

[1] Y. Xia, B. Gates, Y. Yin, Y. Lu, (2000). *Monodispersed colloidal spheres: old materials with new applications*, Adv. Mater. 12, 693–713. https://doi.org/10.1002/(SICI)1521-4095(200005)12:10<693::AID-ADMA693>3.0.CO;2-J

[2] P. Colson, C. Henrist, R. Cloots, (2013). *Nanosphere lithography: a powerful method for the controlled manufacturing of nanomaterials*, J. Nanomaterials, 2013. https://doi.org/10.1155/2013/948510

[3] Pisco, M., Galeotti, F., Quero, G., Grisci, G., Micco, A., Mercaldo, L. V., ... & Cusano, A. (2017). *Nanosphere lithography for optical fiber tip nanoprobes*. Light: Science & Applications, 6(5), e16229-e16229. https://doi.org/10.1038/lsa.2016.229

[4] E. Flores-Romero, E. Rodríguez-Sevilla, J.C Cheang-Wong, (2018). *Silver films over silica micro-spheres (AgFOSM) as SERS substrates*, Photonics and Nanostructures - Fundamentals and Applications 28, 81-87. https://doi.org/10.1016/j.photonics.2017.12.001

[5] W. Stöber, A. Fink, E. Bohn, (1968). *Controlled growth of monodisperse silica spheres in the micron size range*, J. Colloid. Interface Sci. 26, 62–69. https://doi.org/10.1016/0021-9797(68)90272-5

[6] Albert S. Reyna and Cid B. De Araújo, (2017). *High-order optical nonlinearities in plasmonic nanocomposites-a review*, Advances in Optics and Photonics Vol. 9, Issue 4, 720-774. https://doi.org/10.1364/AOP.9.000720

[7] Jeffrey N. Anker, W. Paige Hall, Olga Lyandres, Nilam C. Shah, Jing Zhao & Richard P. Van Duyne, (2008). *Biosensing with plasmonic nanosensors.* Nature Materials 7, 442–453. https://doi.org/10.1038/nmat2162

[8] Tiziana Cesca, Niccolò Michieli, Boris Kalinic, Ionut Gabriel Balasa, Raúl Rangel-Rojo, Jorge Alejandro Reyes-Esqueda, Giovanni Mattei, (2019). *Bidimensional ordered plasmonic nanoarrays for nonlinear optics, nanophotonics and biosensing applications*, Materials Science in Semiconductor Processing, Volume 92, 2-9. https://doi.org/10.1016/j.mssp.2018.03.025

[9] Weissleder, R., Nahrendorf, M., & Pittet, M. J. (2014).*Imaging macrophages with nanoparticles*. Nature materials, 13(2), 125-138. https://doi.org/10.1038/nmat3780

[10] Pang, C., Li, R., Li, Z., Dong, N., Cheng, C., Nie, W., ... & Chen, F. (2018). *Lithium Niobate Crystal with Embedded Au Nanoparticles: A New Saturable Absorber for Efficient Mode-Locking of Ultrafast Laser Pulses at 1 μm. Advanced Optical Materials*, 6(16), 1800357. https://doi.org/10.1002/adom.201800357

[11] M. Kauranen, A. V. Zayats, (2012) *Nonlinear plasmonics*, Nature Photon 6, 737-748. https://doi.org/10.1038/nphoton.2012.244

[12] Y.X. Zhang, Y.H. Wang, (2017) *Nonlinear optical properties of metal nanoparticles: a review*, RSC Adv. 7 45129–45144, https://doi.org/10.1039/C7RA07551K

[13] Kun Liu, Xin Xu, Wen Shan, Di Sun, Chengbao Yao, Wenjun Sun, (2020), *Study on third-order nonlinear optical properties of the composite films with Ag nanoparticles and CdSe quantum dots*, Optical Materials, Volume 99, 109569. https://doi.org/10.1016/j.optmat.2019.109569

[14] Cesca, T., García-Ramírez, E. V., Sánchez-Esquivel, H., Michieli, N., Kalinic, B., Gómez-Cervantes, J. M., ... & Mattei, G. (2017).*Dichroic nonlinear absorption response*

of silver nanoprism arrays. RSC advances, 7(29), 17741-17747. https://doi.org/10.1039/C7RA01722G

[15] Dana Miu, Ionut Nicolae, (2020). *Third order nonlinear optical properties of gold/alumina multilayer nanocomposites with different nanoparticle arrangements*, Thin Solid Films, Volume 697, 137829. https://doi.org/10.1016/j.tsf.2020.137829

[16] Sánchez-Dena, O., Mota-Santiago, P., Tamayo-Rivera, L., García-Ramírez, E. V., Crespo-Sosa, A., Oliver, A., & Reyes-Esqueda, J. A. (2014).*Size-and shape-dependent nonlinear optical response of Au nanoparticles embedded in sapphire*. Optical Materials Express, 4(1), 92-100. https://doi.org/10.1364/OME.4.000092

[17] Nie, W., Tsai, H., Asadpour, R., Blancon, J. C., Neukirch, A. J., Gupta, G., ... & Wang, H. L. (2015). *High-efficiency solution-processed perovskite solar cells with millimeter-scale grains*. Science, 347(6221), 522-525. https://doi.org/10.1126/science.aaa0472

[18] J. Bornacelli, C. Torres-Torres, H.G. Silva-Pereyra, G.J. Labrada-Delgado, A. Crespo-Sosa, J.C. Cheang-Wong, A. Oliver. (2019)*Superlinear photoluminescence by ultrafast laser pulses in dielectric matrices with metal nanoclusters*, Sci. Rep. 9, 1–12. https://doi.org/10.1038/s41598-019-42174-1.

[19] A. Oliver, J.C. Cheang-Wong, J. Roiz, L. Rodríguez-Fernández, J.M. Hernández, A. Crespo-Sosa, E. Muñoz, (2002). *Metallic nanoparticle formation in ion-implanted silica after thermal annealing in reducing or oxidizing atmospheres*, Nuclear Instruments and Methods in Physics Research B 191, 333-336. https://doi.org/10.1016/S0168-583X(02)00528-1

[20] N.C. Panoiu, W.E.I. Sha, D.Y. Lei, G. C Li. (2018) *Nonlinear optics in plasmonic* nanostructures, J. Optic. 20, 083001, https://doi.org/10.1088/2040-8986/aac8ed

[21] C.J. Brinker, G.W. Scherer, (1990). *Sol-Gel Science: The Physics and Chemistry of Sol-Gel Processing*, Academic Press, San Diego. https://doi.org/10.1016/C2009-0-22386-5

[22] Innocenzi, P. (2020). *Understanding sol–gel transition through a picture. A short tutorial*. J Sol-Gel Sci Technol 94, 544–550. https://doi.org/10.1007/s10971-020-05243-w

[23] IUPAC. Compendium of Chemical Terminology, 2nd ed. (the "Gold Book"). Compiled by A. D. McNaught and A. Wilkinson. Blackwell Scientific Publications, Oxford (1997). Online version (2019-) created by S. J. Chalk. ISBN 0-9678550-9-8. https://doi.org/10.1351/goldbook

[24] Innocenzi P. (2019). *A Sol and a Gel, What Are They?. In: The Sol-to-Gel Transition*. SpringerBriefs in Materials. Springer, Cham. https://doi.org/10.1007/978-3-030-20030-5_1

[25] Rahman, I. A., & Padavettan, V. (2012). Synthesis of silica nanoparticles by sol-gel: size-dependent properties, surface modification, and applications in silica-polymer nanocomposites—a review. Journal of Nanomaterials, 2012. https://doi.org/10.1155/2012/132424

[26] Hyde, E. D., Seyfaee, A., Neville, F., & Moreno-Atanasio, (2016). *R. Colloidal silica particle synthesis and future industrial manufacturing pathways: a review*. Industrial & Engineering Chemistry Research, 55(33), 8891-8913. https://doi.org/10.1021/acs.iecr.6b01839

[27] LaMer, V. K., & Dinegar, R. H. (1950). *Theory, production and mechanism of formation of monodispersed hydrosols*. Journal of the American Chemical Society, 72(11), 4847-4854. https://doi.org/10.1021/ja01167a001

[28] Klimov, V. (2014). *Nanoplasmonics*. CRC press.

[29] Zhang, J. X., & Hoshino, K. (2018). Molecular Sensors and Nanodevices: Principles, Designs and Applications in Biomedical Engineering. Academic Press.

[30] Dresselhaus, M., Dresselhaus, G., Cronin, S. B., & Souza Filho, A. G. (2018). *Solid State Properties*. https://doi.org/10.1007/978-3-662-55922-2

[31] Solé, J., Bausa, L., & Jaque, D. (2005). *An introduction to the optical spectroscopy of inorganic solids*. John Wiley & Sons.

[32] Barbillon. G (2017) *Nanoplasmonics-Fundamentals and Applications* InTech. https://doi.org/10.5772/65150

[33] Lu, X., Rycenga, M., Skrabalak, S. E., Wiley, B., & Xia, Y. (2009). *Chemical synthesis of novel plasmonic nanoparticles.* Annual review of physical chemistry, 60, 167-192. https://doi.org/10.1146/annurev.physchem.040808.090434

[34] Serrano A. (2014) *Modifed Au-based nanomaterials studied by surface plasmon resonance spectroscopy* Tesis Doctoral, Universidad Complutense de Madrid. Madrid, España.

[35] M. A. Garcia (2011) *Surface plasmons in metallic nanoparticles: fundamentals and applications* Journal of Physics D: Applied Physics, vol. 44, 28, 283001. https://doi.org/10.1088/0022-3727/44/28/283001

[36] Bohren, C. F., & Huffman, D. R. (2008).*Absorption and scattering of light by small particles*. John Wiley & Sons.

[37] Mie, G. (1908). *Beiträge zur Optik trüber Medien, speziell kolloidaler Metallösungen.* Annalen der physik, 330(3), 377-445. https://doi.org/10.1002/andp.19083300302

[38] Noguez, C. (2007). *Surface plasmons on metal nanoparticles: the influence of shape and physical environment*. The Journal of Physical Chemistry C, 111(10), 3806-3819. https://doi.org/10.1021/jp066539m

[39] R. W. Boyd. (2008) *Nonlinear Optics*, Academic Press. 3rd edn.

[40] Stockman, M. I. (2011). *Nanoplasmonics: past, present, and glimpse into future*. Optics express, 19(22), 22029-22106.

[41] O. Sánchez (2019) *Lithium Niobate powders: its Chemical Composition and a stuyd of its Second Harmonic Generation response*, Tesis Doctoral, UNAM, Ciudad de México, México.

[42] Sutherland, R. L. (2003). Handbook of nonlinear optics. CRC press.

[43] Norman. P, Ruud K. (2006) *Theory of Nonlinear Optics. In Non-Linear Optical Properties of Matter* Springer. https://doi.org/10.1007/1-4020-4850-5_1

[44] Palpant, B. (2006). *Third-order nonlinear optical response of metal nanoparticles. In Non-linear optical properties of matter* (pp. 461-508). Springer, Dordrecht. https://doi.org/10.1021/jp502294u

[45] Del Coso, R., & Solis, J. (2004). *Relation between nonlinear refractive index and third-order susceptibility in absorbing media*. JOSA B, 21(3), 640-644. https://doi.org/10.1364/JOSAB.21.000640

[46] Tanahashi, I., Manabe, Y., Tohda, T., Sasaki, S., & Nakamura, A. (1996). *Optical nonlinearities of Au/SiO2 composite thin films prepared by a sputtering method*. Journal of Applied Physics, 79(3), 1244-1249. https://doi.org/10.1063/1.361018

[47] Hamanaka, Y., Fukuta, K., Nakamura, A., Liz-Marzán, L. M., & Mulvaney, P. (2004). *Enhancement of third-order nonlinear optical susceptibilities in silica-capped Au nanoparticle films with very high concentrations*. Applied Physics Letters, 84(24), 4938-4940. https://doi.org/10.1063/1.1760229

[48] Ning, T., Chen, C., Zhou, Y., Lu, H., Shen, H., Zhang, D., ... & Yang, G. (2009). *Third-order optical nonlinearity of gold nanoparticle arrays embedded in a BaTiO 3 matrix*. Applied optics, 48(2), 375-379. https://doi.org/10.1364/AO.48.000375

[49] Z. Lu, H. Owens, (2018). *A method to improve the quality of silica nanoparticles (SNPs) over increasing storage durations*, J. Nanopart. Res. 20, 213. https://doi.org/10.1007/s11051-016-3691-8

[50] C. Hubner, C. Fettkenhauer, K. Voges, D.C. Lupascu, (2018). *Agglomeration-free preparation of modified silica nanoparticles for emulsion polymerization - A well scalable process*, Langmuir 34, 376-383. https://doi.org/10.1021/acs.langmuir.7b03753

[51] W. Gao, M. Rigout, H. Owens, (2016). *Facile control of silica nanoparticles using a novel solvent varying method for the fabrication of artificial opal photonic crystals*, J. Nanopart. Res. 18, 387. https://doi.org/10.1007/s11051-016-3691-8

[52] Hulteen, J. C., & Van Duyne, R. P. (1995). *Nanosphere lithography: A materials general fabrication process for periodic particle array surfaces*. Journal of Vacuum Science & Technology A: Vacuum, Surfaces, and Films, 13(3), 1553-1558. https://doi.org/10.1116/1.579726

[53] Manfrinato, V. R., Camino, F. E., Stein, A., Zhang, L., Lu, M., Stach, E. A., & Black, C. T. (2019). *Patterning Si at the 1 nm Length Scale with Aberration-Corrected Electron-Beam Lithography: Tuning of Plasmonic Properties by Design*. Advanced Functional Materials, 29(52), 1903429. https://doi.org/10.1002/adfm.201903429

[54] Takeuchi, M., Yamaguchi, A., & Utsumi, Y. (2019). *Deep X-ray lithography system with a uniform and high-accuracy fabrication area established in beamline BL11 at NewSUBARU*. Journal of synchrotron radiation, 26(2), 528-534. https://doi.org/10.1107/S1600577518017939

[55] Denkov, N., Velev, O., Kralchevski, P., Ivanov, I., Yoshimura, H., & Nagayama, K. (1992). *Mechanism of formation of two-dimensional crystals from latex particles on substrates*. Langmuir, 8(12), 3183-3190. https://doi.org/10.1021/la00048a054

[56] Kralchevsky, P. A., & Denkov, N. D. (2001). *Capillary forces and structuring in layers of colloid particles*. Current opinion in colloid & interface science, 6(4), 383-401. https://doi.org/10.1016/S1359-0294(01)00105-4

[57] Nagayama, K. (1996). *Two-dimensional self-assembly of colloids in thin liquid films*. Colloids and Surfaces A: Physicochemical and Engineering Aspects, 109, 363-374. https://doi.org/10.1016/0927-7757(95)03467-6

[58] Velázquez, M. M., Alejo, T., López-Díaz, D., Martín-García, B., & Merchán, M. D. (2016). *Langmuir-Blodgett Methodology: A Versatile Technique to Build 2D Material Films*. TWO-DIMENSIONAL MATERIALS, 21. https:/doi.org/10.5772/63495

[59] Hsu, C. M., Connor, S. T., Tang, M. X., & Cui, Y. (2008). *Wafer-scale silicon nanopillars and nanocones by Langmuir–Blodgett assembly and etching*. Applied Physics Letters, 93(13), 133109. https://doi.org/10.1063/1.2988893

[60] Emslie, A. G., Bonner, F. T., & Peck, L. G. (1958). *Flow of a viscous liquid on a rotating disk*. Journal of Applied Physics, 29(5), 858-862. https://doi.org/10.1063/1.1723300

[61] Zhang, F., Di, C. A., Berdunov, N., Hu, Y., Hu, Y., Gao, X., ... & Zhu, D. (2013). *Ultra thin film organic transistors: precise control of semiconductor thickness via spin-coating*. Advanced Materials, 25(10), 1401-1407. https://doi.org/10.1002/adma.201204075

[62] Yuan, Y., Giri, G., Ayzner, A. L., Zoombelt, A. P., Mannsfeld, S. C., Chen, J., ... & Bao, Z. (2014). *Ultra-high mobility transparent organic thin film transistors grown by an off-centre spin-coating method*. Nature communications, 5(1), 1-9. https://doi.org/10.1038/ncomms4005

[63] Liu, C., Li, W., Zhang, C., Ma, Y., Fan, J., & Mai, Y. (2018). *All-inorganic CsPbI2Br perovskite solar cells with high efficiency exceeding 13%*. Journal of the American chemical society, 140(11), 3825-3828. https://doi.org/10.1021/jacs.7b13229

[64] Li, J., Shan, X., Bade, S. G. R., Geske, T., Jiang, Q., Yang, X., & Yu, Z. (2016) . *Single-layer halide perovskite light-emitting diodes with sub-band gap turn-on voltage and high brightness*. The journal of physical chemistry letters, 7(20), 4059-4066. https://doi.org/10.1021/acs.jpclett.6b01942

[65] Jeon, N. J., Noh, J. H., Kim, Y. C., Yang, W. S., Ryu, S., & Seok, S. I. (2014). *Solvent engineering for high-performance inorganic–organic hybrid perovskite solar cells*. Nature materials, 13(9), 897-903. https://doi.org/10.1038/nmat4014

[66] Burschka, J., Pellet, N., Moon, S. J., Humphry-Baker, R., Gao, P., Nazeeruddin, M. K., & Grätzel, M. (2013). *Sequential deposition as a route to high-performance perovskite-sensitized solar cells*. Nature, 499(7458), 316-319. https://doi.org/10.1038/nature12340

[67] Ji, L., Hsu, H. Y., Lee, J. C., Bard, A. J., & Yu, E. T. (2018). *High-performance photodetectors based on solution-processed epitaxial grown hybrid halide perovskites*. Nano letters, 18(2), 994-1000. https://doi.org/10.1021/acs.nanolett.7b04445

[68] Kelso, M. V., Mahenderkar, N. K., Chen, Q., Tubbesing, J. Z., & Switzer, J. A. (2019). *Spin coating epitaxial films*. Science, 364(6436), 166-169. https://doi.org/10.1126/science.aaw6184

[69] Ko, Y. G., Shin, D. H., Lee, G. S., & Choi, U. S. (2011). Fabrication of colloidal crystals on hydrophilic/hydrophobic surface by spin-coating. Colloids and Surfaces A: Physicochemical and Engineering Aspects, 385(1-3), 188-194. https://doi.org/10.1016/j.colsurfa.2011.06.011

[70] Dunlap, M., & Adaskaveg, J. E. (1997). *Introduction to the scanning electron microscope*. Theory, practice, & procedures. Facility for Advance Instrumentation. UC Davis, 52.

[71] Nastasi, M. A., & Mayer, J. W. (2006). *Ion implantation and synthesis of materials* (Vol. 5). Berlin: Springer. https://doi.org/10.1007/978-3-540-45298-0

[72] M. A. García Cruz (2017) *Surface morphology of ti and ti-6al-4v bombarded with 1.0-MeV au ions*, Tesis Doctoral, UNAM, Ciudad de México, México.

[73] Nastasi, M., Michael, N., Mayer, J., Hirvonen, J. K., & James, M. (1996). *Ion-solid interactions: fundamentals and applications*. Cambridge University Press. https://doi.org/10.1017/CBO9780511565007

[74] J.F. Ziegler, J.P. Biersack, U. Littmark. (2985). *The Stopping and Range of Ions in Solids*, Pergamon, New York. https://doi.org/10.1007/978-3-642-68779-2_5

[75] J.R Tesmer, M. Nastari (1995)*Handbook of Modern Ion Beam Materials Analysis* Materials Research Society, Pittsburgh, Pennsylvania.

[76] Schmidt, B., & Wetzig, K. (2012). *Ion beams in materials processing and analysis*.

[77] Y. Wang, M. Nastasi, (2009). *Handbook of Modern Ion-Beam Materials Analysis*, Materials Research Society, Pittsburgh.

[78] M. Sheik-Bahae, A. A. Said, T. H. Wei, D. J. Hagan, and E. W. Van Stryland. (1990). *Sensitive measurement of optical nonlinearities using a single beam*, IEEE J. Quantum Electron. 26(4), 760–769. https://doi.org/10.1109/3.53394

[79] Georges Boudebs and Kamil Fedus. (2009). *Absolute measurement of the nonlinear refractive indices of reference materials*, Journal of applied physics 105, 103106. https://doi.org/10.1063/1.3129680

[80] Reichert, M., Hu, H., Ferdinandus, M. R., Seidel, M., Zhao, P., Ensley, T. R., ... & Hagan, D. J. (2014). *Temporal, spectral, and polarization dependence of the nonlinear optical response of carbon disulfide*. Optica, 1(6), 436-445. https://doi.org/10.1364/OPTICA.1.000436

[81] Schneider, C., Rasband, W. & Eliceiri, K. (2012) *NIH Image to ImageJ: 25 years of image analysis*. Nat Methods 9, 671–675. https://doi.org/10.1038/nmeth.2089

[82] Yano, K., & Fukushima, Y. (2003). *Particle size control of mono-dispersed super-microporous silica spheres*. Journal of Materials Chemistry, 13(10), 2577-2581. https://doi.org/10.1039/B304867P

[83] Liang, X., Lian, L., Liu, Y., Kong, Q., & Wang, L. (2016). *Controlled synthesis of monodisperse silica particles*. Micro & Nano Letters, 11(9), 532-534. https://doi.org/10.1049/mnl.2016.0189

[84] Wang, X. D., Shen, Z. X., Sang, T., Cheng, X. B., Li, M. F., Chen, L. Y., & Wang, Z. S. (2010). *Preparation of spherical silica particles by Stöber process with high concentration of tetra-ethyl-orthosilicate*. Journal of colloid and interface science, 341(1), 23-29. https://doi.org/10.1016/j.jcis.2009.09.018

[85] G.H. Bogush, C.F. Zukoski. (1991). *Uniform silica particle precipitation: An aggregative growth model*, J. Colloid Interf. Sci. 142, 19. https://doi.org/10.1016/0021-9797(91)90030-C

[86] A. van Blaaderen, J. van Geest, A. Vrij. (1992). *Monodisperse colloidal silica spheres from tetraalkoxysilanes: Particle formation and growth mechanism*, J. Colloid Interface Sci, 154(2), 481-501. https://doi.org/10.1016/0021-9797(92)90163-G

[87] T. Matsoukas, E. Gulari. (1988). *Dynamics of growth of silica particles from ammonia-catalyzed hydrolysis of tetra-ethylorthosilicate*, J. Colloid Interf. Sci 124. 252–261. https://doi.org/10.1016/0021-9797(88)90346-3

[88] J.C. Cheang-Wong, U. Morales, A. Oliver, L. Rodríguez-Fernández, J. Rickards. (2006) *MeV ion beam deformation of colloidal silica particles*, Nuclear Instruments and Methods B 242, 452-254. https://doi.org/10.1016/j.nimb.2005.08.078

[89] E. Reséndiz, U. Morales, C. Salinas, O. Graniel, L.M. López, J.C. Cheang-Wong. (2014) *Ion-beam modification of colloidal silica particle masks to tailor the size of ordered arrays of Ag produced by nanosphere lithography*, Mater. Res. Soc. Symp. Proc. 1712. http://dx.doi.org/10.1557/opl.2014.871

[90] T. Ning, C. Chen, H. Lu, H. Shen, D. Zhang, P. Wang, H. Ming, G. Yang. (2009) *Third-order optical nonlinearity of gold nanoparticle arrays embedded in BaTiO3 matrix.* Applied Optics 68, 375-379. https://doi.org/10.1364/AO.48.000375

[91] Silva-Pereyra, H. G., Arenas-Alatorre, J., Rodriguez-Fernández, L., Crespo-Sosa, A., Cheang-Wong, J. C., Reyes-Esqueda, J. A., & Oliver, A. (2010). *High stability of the crystalline configuration of Au nanoparticles embedded in silica under ion and electron irradiation.* Journal of Nanoparticle Research 12(5), 1787-1795. https://doi.org/10.1007/s11051-009-9735-6

[92] Fukumi, K., Chayahara, A., Kadono, K., Sakaguchi, T., Horino, Y., Miya, M., ... & Satou. (1994). *Gold nanoparticles ion implanted in glass with enhanced nonlinear optical properties.* Journal of applied physics 75(6), 3075-3080. https://doi.org/10.1063/1.356156

[93] Doolittle, L. R. (1985). *Algorithms for the rapid simulation of Rutherford backscattering spectra.* Nuclear Instruments and Methods in Physics Research Section B: Beam Interactions with Materials and Atoms, 9(3), 344-351. https://doi.org/10.1016/0168-583X(85)90762-1

[94] Ovidio Peña-Rodríguez, Pedro Pablo González Pérez, and Umapada Pal. (2011). *MieLab: A Software Tool to Perform Calculations on the Scattering of Electromagnetic*

Waves by multilayered Spheres, International Journal of Spectroscopy Volume 2011, Article ID 583743. https://doi.org/10.1155/2011/583743

[95] Alastair D. Humphrey and William L. Barnes, (2014) *Plasmonic surface lattice resonances on arrays of different lattice symmetry*, Physical Review B 90, 075404. https://doi.org/10.1103/PhysRevB.90.075404